An inverse source problem in planetary sciences. Dipole localization in Moon rocks from sparse magnetic data

Konstantinos Mavreas

UNIVERSITÉ CÔTE D'AZUR

ÉCOLE DOCTORALE
SCIENCES ET TECHNOLOGIES DE L'INFORMATION ET DE LA COMMUNICATION

THÈSE DE DOCTORAT

Un problème inverse de source en sciences planétaires: localisation d'un dipole magnétique dans des roches lunaires à partir de données magnétiques clairsemées

Konstantinos MAVREAS
INRIA

Présentée en vue de l'obtention du grade de docteur en
Automatique, Traitement du Signal et des Images
d'Université Côte d'Azur
Dirigée par: Juliette LEBLOND
Soutenue le: janvier 31, 2020

Devant le jury, composé de:
Juliette LEBLOND, Directrice de recherche, Inria
Sylvain CHEVILLARD, Chargé de recherche, Inria
Yannick PRIVAT, Professeur, IRMA - Université de Strasbourg
Ioannis STRATIS, Professeur, National and Kapodistrian University of Athens
Laure BLANC FERAUD, Directrice de recherche, I3S, CNRS
Yoann QUESNEL, Maître de conférence, CEREGE, Aix-Marseille Université

Inria

Un problème inverse de source en sciences planétaires : localisation d'un dipole magnétique dans des roches lunaires à partir de données magnétiques clairsemées

Jury :

Directrice de thèse :		
Juliette Leblond	Directrice de recherche	INRIA, Sophia Antipolis, France
Co-directeur de thèse :		
Sylvain Chevillard	Chargé de recherche	INRIA, Sophia Antipolis, France
Rapporteurs :		
Yannick Privat	Professeur	IRMA, Université de Strasbourg, France
Ioannis Stratis	Professeur	National and Kapodistrian University of Athens, Grèce
Examinateurs :		
Laure Blanc Feraud	Directrice de recherche	I3S, CNRS, Sophia Antipolis, France
Yoann Quesnel	Maître de conférence	CEREGE, Aix-Marseille Université, France

Titre : Un problème inverse de source en sciences planétaires : localisation d'un dipole magnétique dans des roches lunaires à partir de données magnétiques clairsemées

---

Résumé :

Les anomalies magnétiques à la surface de la Lune, indiquent que celle-ci a eu un champ magnétique propre. Les géologues étudient la magnétisation rémanente des roches de la Lune, afin de comprendre l' origine et l' évolution de cet ancien champ lunaire. Les informations disponibles, collectées à partir de techniques non invasives telles que l' utilisation d' un magnétomètre tournant, correspondent à certaines composantes du champ magnétique de l' échantillon. Ceci fournit un problème inverse qui consiste à récupérer les caractéristiques de la magnétisation à partir du champ qu' elle génère.
Nous faisons l' hypothèse de que la source magnétique est ponctuelle et unique. En se fondant sur une telle hypothèse, une approche existante consiste à postuler la position de la source magnétique au centre de masse de l' échantillon, puis à résoudre un problème linéaire pour retrouver la magnétisation. Dans cette thèse, nous proposons d' utiliser d' abord les données disponibles pour estimer l' emplacement de la source, ce qui est un problème non linéaire. La magnétisation est ensuite retrouvée, comme avec l' autre approche, en résolvant un problème linéaire.
Dans notre étude, nous observons l' existence d' une relation entre les pôles d' une fonction rationnelle et l' emplacement de la source magnétique. Nous utilisons des schémas d' approximation rationnelle pour récupérer le pôle de la fonction rationnelle à partir de ses valeurs sur un cercle. Nous proposons ensuite différentes méthodes pour utiliser le lien entre le pôle récupéré et l' emplacement de la source, afin de l' estimer. Nous avons mené des expériences numériques pour analyser le comportement de ces méthodes et comparer leurs qualités.

Mots clés : roches de la Lune, source magnétique, estimer l' emplacement de la source, approximation rationnelle, problème inverse.

Title : An inverse source problem in planetary sciences : dipole localization in Moon rocks from sparse magnetic data.

Abstract :

Magnetic anomalies on the Moon's surface indicate that the Moon used to have a global magnetic field for millions of years that no longer exist. Geoscientists need to study the remanent magnetization (strength and direction) of Moon rocks, in order to understand the origin and the evolution of this ancient lunar field. This remanent magnetization is preserved from ferromagnetic materials. From non-invasive techniques such as with the use of a spinner magnetometer, the available information is some measurements of the sample's magnetic field. This leads to an inverse problem which is to recover the magnetization characteristics from the field it generates. We use the hypothesis of a single pointwise magnetic source (dipolar model). With such an assumption, an existing approach is to set the magnetic source position at the sample's mass center and then solve a linear problem to recover the magnetization. In this thesis we propose to use the available data to first estimate the location of the dipolar source, which is a nonlinear problem. The magnetization is then recovered as with the other approach, by solving a linear problem.
In our study, we observe that there is a relation between the poles of a rational function and the magnetic source location. We use rational approximation schemes to recover the pole of the rational function from its values on a circle. Then we propose several methods to use the link between the recovered pole and the source location, in order to estimate it. Methods like these take advantage of the geometrical features derived from our physical model equations. We conducted numerical experiments to analyze the behavior of these methods and compare their qualities.

Keywords : Moon rocks, magnetic dipole, source estimation, rational approximation, inverse problems.

Acknowledgments

Looking back at the last four years of my life, I realize that I wouldn't have reached my destination without the help, the guidance and the support of many people. In this section I would like to express my gratitude and my appreciation to all of them.

First of all I would like to equally thank my supervisors, Sylvain Chevillard and Juliette Leblond for their continuous support, patience and guidance over all these years. I am grateful for their trust and their efficient and creative ways in teaching me mathematics, physics and computer science.

Sylvain, thank you very much for your dedication and your efforts to expand my knowledge in mathematics and computer science, without your challenges and your guidance I wouldn't have the ability to express my ideas properly. Your valuable courses on various mathematical topics has improved my confidence and helped me to deeply understand my subject in order to fulfill my thesis.

Juliette, thank you for your attention and care for my research progress. Thank you for all of the hours you have spent with me discussing, explaining and analyzing mathematics and physics. You are a true inspiration to me for both your scientific work and your kindness. You reveal to me the connection between different areas of mathematics, which changes the way I approach mathematics. Thank you for helping me to overcome scientific and personal difficulties during all those years. I was extremely lucky to have you and Sylvain as my supervisors.

I would also like to thank the reviewers of my thesis: Ioannis Stratis and Yannick Privat. Thank you for your time and efforts in reviewing my thesis as well as for your valuable comments and remarks.

Also a big thanks to Laure Blanc Feraud and Yoann Quesnel who were members of the jury (together with my supervisors and my reviewers) during my PhD defense day. It was a pleasure to collaborate with you. Thank you for your remarks and your questions, they were important and have underlined the challenges behind my research.

Next I would like to give my thanks to Laurent Baratchart. He trusted me and invited me (together with my supervisors) to join the IMPINGE team, which is a collaborative project with the Paleomagnetic Lab of Earth, Atmospheric and Planetary Sciences Department in MIT.

During my time in Boston, I had the chance to meet and work with Eduardo Andrade Lima. I appreciate him for his warm welcome and his patience in explaining to me the Spherical harmonics theory. For me the visit to MIT was a dream that came true, working there was a boost of motivation and inspiration, which I truly appreciate and will never forget.
I would also like to thank Martine Olivi and Jean-Paul Marmorat, both of you help me to understand how RARL2 software works, you were never tired of my countless questions and you were always happy to enlighten me with your answers and provide me bibliographic materials.
I would not forget to thank Fabien Seyfert who helped me unconditionally with my thesis extension, as well as our assistants Stephanie Sorres and Marie-Line Meirinho who resolved plenty of administrative issues all those years.

A huge thanks to my porcos Dmitry, Matthias, Christos, Stefanos and Adam for the support and the good memories we shared together. Christos, thank you, because without you, the decision to come and study in France would have been much more difficult. Thank you also for your consistent back up! Adam and Mathias, the two most amazing Belgian guys I have ever met! Thanks to both of you for the time we spent together and your cheerful spirit! My Italian porcellino Stefano, thank you for the risotto cooking nights and your warm hospitality in Pavia. Dmitry my brilliant Russian friend, Thank you for all the precious moments we shared together and your legendary stories.

I cannot miss the opportunity to give a huge thanks to all the Apics team members for their support all this time. A special thanks goes to my office mates David, Gibin and Yacine. You are all great company and wonderful friends. An extra thanks to Gibin for his hospitality during the last month of my PhD.
My very special thanks also goes to my friends: Francesco, Brahim, Marco, Dimitra, Elena, Dora, Ines, Valeria, Paul, Masimba. Guys, it is always great to be around you.
A huge thanks to my friends from Greece: Giorgo, Theotoki, Roza, Zissi and Antoni. Despite the distance that separates us, every time we meet each other is like nothing has changed in our friendship.

An enormous thanks to my family. My parents Giorgo and Teta, they are the best parents who have been providing the best things they could since the first day of my life. Thank you for being there for me and supporting me unconditionally. My brother Oresti is a true inspiration for me and the best brother one can have. A big thanks to my grandfather Oresti who spoiled me as a kid and sparked my interest in knowledge. A special thanks to my uncle Kosta, who introduced me to the world of mathematics when I was a kid and initiated my admire for it.

Last but not least, I would like to thank my dear wife, Yu. Thank you for your support, your caring and your love, especially during the last months of my thesis. You have helped me the most to form a better personality. Your strength has encouraged me to surpass all the difficulties I faced. I am extremely lucky to have you in my life.

Table of Contents

Abstract

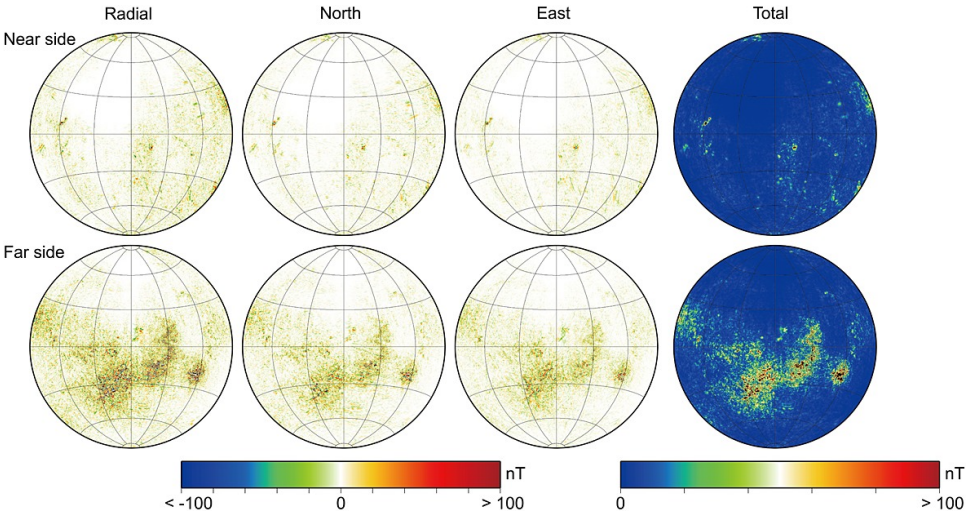

Figure 1: Global maps of three components and total intensity of the lunar magnetic anomalies at 30 km altitude (SVM30) [1].

Magnetic anomalies on the Moon's surface (see Figure 1) indicate that the Moon used to have a global magnetic field [2]. Geoscientists need to study the remanent magnetization (strength and direction) of Moon rocks, in order to understand the origin and the evolution of this ancient lunar magnetic field. From non-invasive techniques such as with the use of a spinner magnetometer, we are able to measure the sample's magnetic field. This leads to an inverse problem which is to recover the magnetization characteristics from the field it generates.
We use the hypothesis of a single pointwise magnetic source (dipolar model). With such an assumption, an existing approach is to set the magnetic source position at the sample's mass center and then solve a linear problem to recover the magnetization. In this thesis we propose to use the available data to first estimate the location of the dipolar source, which is a nonlinear problem. Practically with the proper data treatment we translate our source localization problem to a rational approximation problem. The magnetization is then recovered as with the other approach, by solving a linear

problem.
In our study, we observe that there is a relation between the poles of a rational function and the magnetic source location. We use rational approximation schemes to recover the pole of the rational function from its values on a circle. Then we propose several methods to use the link between the recovered pole and the source location, in order to estimate it. We conducted numerical experiments to analyze the behavior of these methods and compare their qualities.

Introduction and thesis outline

During the last sixty years, our understanding of the Moon has changed drastically. In 1959 Luna 2 mission carried a three-component fluxgate magnetometer and it didn't detect a global magnetic field on the Moon, this was in agreement with the theory that the Moon is too small to produce a dynamo field similar to that of the Earth's. The same year Luna 3 mission took the first photograph of the far side of the Moon revealing a landscape covered mostly with impact craters in contrast to the near side of the Moon (the side that is always visible from Earth) which is 30% covered with basaltic plains of ancient volcanic activity known as "mare". However, the giant leap came with the Apollo missions in 1969 and the discovery of ancient Lunar magnetism! Apollo 11 (July 1969) and Apollo 12 (November 1969) missions revealed a significant surface magnetic field which comes from crustal remanent magnetization anomalies see Figure 1. Even early studies of the Apollo samples [3] reveal that the Moon had a strong magnetic field, with a value up to 100 μT, between 3.9-3.6 Ga (billion years) ago, see Figure 2.
The Earth's magnetic field is generated by a geodynamo and it ranges from 25-65 μT. The Moon is a planetary object with mass about 1.2% of the Earth's mass however we have evidences that it used to have an ancient magnetic field with strength up to 100 μT. This is a puzzling situation because when scientists calculated the theoretical maximum field strength at the surface of the Moon from a geodynamo mechanism [4,5], they found that it should range between 12-16 μT. So how it is possible a small planetary object like the Moon can generate such a strong magnetic field? One idea to answer this question is that the mechanism that produces the Moons global magnetic field was different from that of the Earth's. In [4] they also study the idea of a field generated by a precession core crystallization, and/or thermal convection dynamo, in that case an intensity of 71-77 μT is possible. Another idea is that the strong remanent magnetization of the Moon rocks is the effect of impact events [6] and their magnetic field of the impact-generated plasma.

So what is the remanent magnetization and how paleomagnetic studies try to recover it? The origin of the magnetization comes from

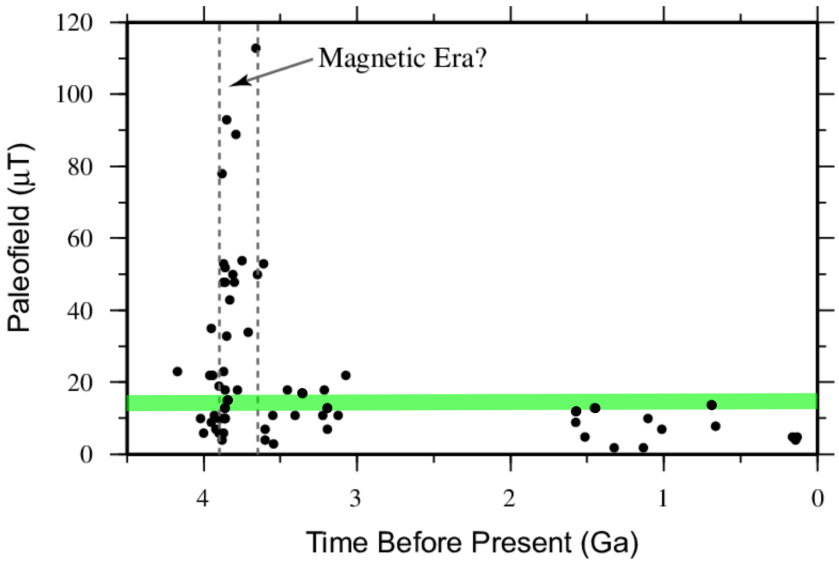

Figure 2: Absolute and IRMs normalization paleointensities of the Lunar samples as a function of time. Each point represents a single Lunar rock. The green area corresponds to the theoretical maximum field strength at the surface of the Moon generated by a dynamo mechanism. Data taken from [3].

quantum mechanics phenomena [7] that are not in the scope of this thesis. Nonetheless it is interesting to discuss how these phenomena affects the behavior of the chemical elements of the periodic table under the influence of an external magnetic field. Based on the interaction of an element with an external magnetic field, we can categorize the chemical elements (with respect to their magnetic properties) into four groups known as antiferromagnetic, paramagnetic, diamagnetic and ferromagnetic/ferrimagnetic. More precisely elements with no response to an external magnetic field are called antiferromagnetic. Elements that have weak interactions with the applied magnetic field are called paramagnetic if they are attracted by the field, and diamagnetic if they are repelled from the magnetic field. Finally elements with strong interactions with the applied magnetic field are called ferromagnetic/ferrimagnetic. Ferromagnetic materials are able to retain their magnetic properties after the external field has been removed [8]. Iron is one of the most important ferromagnetic elements, for this reason minerals (mixes of elements with metals) that contain iron such as magnetite, hematite and pyrrhotite are crucial for paleomagnetic studies [8]. Since iron is so important for our study, it will be useful to know the iron concentration on the Moon's surface. More precisely the iron abundance in Lunar surface varies from 0.1 wt% (weight percent) in mare basalts to 1-2 wt% in the largest crater basis with an average abundance of 0.11-0.45 wt% [9]. That

means that some Apollo samples are not good candidates for paleomagnetic studies due to low iron content and some of the good samples with high iron content must have been enriched with iron from asteroidal projectiles [6].

Paleomagnetic studies focused on remanent magnetization preserved by ferromagnetic materials. This magnetization is the result of a cooling process under the influence of a magnetic field. In paleomagnetic studies they can use noninvasive or invasive techniques to estimate the magnetization of a sample. For instance a noninvasive technique is to measure the magnetic field around a sample and try to estimate the magnetization from this information [10,11]. On the other hand a common invasive demagnetization technique in paleomagnetic studies is the Thellier-Thellier method [12]. With the Thellier-Thellier method, a sample is exposed to various stages of heating, at each stage the natural remanent magnetization (NRM) of the sample is replaced with thermal remanent magnetization (TRM). At the end of this process the NRM is totally replaced with TRM and an estimation of NRM is recovered through the known TRM data. Unfortunately both noninvasive and invasive techniques have a degree of uncertainty for the NRM estimation. That happens because for noninvasive techniques we are dealing with inverse problems that depend on the model, for instance the use of a dipolar or a multipolar source affects the estimation of the magnetization, because it explains the magnetic field data under different assumptions. On the other hand for invasive techniques like Thellier-Thellier method not only do we damage the sample, but at the same time in order to have a good estimation of the magnetization, we need to satisfy specific conditions such as the single-domain magnetic grains [13]. Though human processed objects like bricks and pottery satisfy the single-domain magnetic grains condition it is not common to find natural objects such as rocks that they do. That means the paleointensity data illustrated in Figure 2 have uncertainty for both their intensity and their age. For this reason the need to study the Apollo samples with modern magnetometers and new theories is essential. One of the goals of our study is to develop tools that can increase the confidence on the noninvasive techniques.

Some open questions: we saw before, that the records of the ancient Lunar magnetic field, are preserved in Moon rocks, for billions of years, in the form of remanent magnetization (NRM). Those rocks reveal pieces of the ancient Moon's magnetic history. The goal of the geoscientists is to combine this information and understand the mechanism and the evolution of this ancient magnetic field. What are the origins and the mechanisms of this field? What was its intensity and its evolution? Why did it disappear? How does a small planetary object have the ability to generate a long lasting magnetic field? All of these questions are still open for the geoscientists.

Why a planetary magnetic field is important? To answer this question we need to know how Earth's magnetic field is useful. The main reason why Earth's magnetic field is important is because it protects us against the solar wind [14, ch. 15]. Solar wind is a phenomenon where charged particles from the Sun "bombard" a planet. Without a global planetary magnetic field the upper layers of the atmosphere are exposed to those charged particles. That results in the slow and gradual loss of the atmosphere. For Earth specifically, the ozone layer, which protects us from the cosmic radiation and part of the Sun's ultraviolet radiation, is located at the upper level of our atmosphere and it is more vulnerable to solar wind. Consequently it is not an exaggeration to say that life on the Earth as we know it, exists because of the magnetic field of our planet. Another reason is due to the fact that humans depend more and more on assets that are in orbit around our planet. The satellites and other space devices face a potential threat from the charged particles of the solar wind [15]. However a magnetic field is not stable. It has a periodic cycle of geomagnetic polarity reversals [16], during the reversals the field strength drops to low levels and as a result the danger for satellite damage increases. For those reasons it is important to understand how a planetary object generates a global magnetic field, what is the minimum size required to sustain it? And what conditions affect its intensity?

Challenges

From the 2200 returned samples of Apollo missions that are stored in NASA facilities[1] only 90 had been studied for paleomagnetism upto 2010. A more exhaustive study which measuresd 123 new samples, took place in 2016 by scientists from Cerege [11]. The difference between the previous studies and the latest one was that previous studies focused on small fragments usually with a weight less than 1 g (with exception [17] which studied samples with weight between 0.24-8.05 g) and many of those used invasive demagnetization methods. The motivation of our research is to study large samples from the Apollo missions weighing between 50 g & 4 kg. For a study like this, an invasive technique is not an option. The large Apollo samples must be protected and only after significant evidence of paleomagnetic importance, can a small fragment of the sample be extracted for further invasive studies. For this reason it is important to decide which rocks have interesting magnetic properties. The current approach used by geoscientists is to assume that the generated magnetic field can be explained by a single dipole, which is located at the center of the mass of the sample.

[1] Lunar Sample Laboratory: `https://curator.jsc.nasa.gov/lunar/`

Thesis Contribution

Our contribution is to expand the model used by geoscientists. Though we also assume that the magnetic field can be explained by a single dipole, the location of the dipole could be anywhere inside the sample. A model like that has the advantage, for instance, to indicate the area from where a fragment should be extracted. In addition, for large samples, a better localization of the dipole, leads to better estimation for the strength of the magnetization. Both of these are necessary for the geoscientists to take the correct decision in the samples selection.
These new paleomagnetic studies are the consequence of the growing interest around the Moon and its history. The French National Research Agency (ANR) participated in this research expedition by funding the MagLune project[2]. The innovation of this project is the collaboration between French research centers CEREGE, IPGP, ISTerre, INRIA and American organizations and institutes MIT, NASA which put in action the study of the same problem from many different scientific fields.
Though our research focuses on Lunar rock samples, its results can be used to study remanent magnetization from rock samples of other planets and planetary objects in our solar system. With our research we can even study the magnetic properties of meteorites.

Thesis outline

The issue of the magnetization recovery can be broken into two subproblems. The first problem is to find the location of the magnetic dipole (chapters 2, 3, 4) and the second problem is to recover the strength and the direction of the magnetic dipole (chapter 5). The content of this thesis is structured as follows:

Chapter 1: in this chapter we describe the data acquisition process and the physical model of our study. We explain the problem we face and we derive the equations that describe it. We also describe the simulations framework for our synthetic data experiments. The setup of these experiments will be used to test and compare the various methods of our study in the rest of the thesis.

Chapter 2: in this chapter we describe the data treatment, based on this process we are able to start our analysis. Part of the solution of the localization problem depends on the estimation of a pole of a rational function inside the unit disk. That happens because the pole is linked with information regarding the dipole location. The goal of this chapter is to provide an

[2] `http://maglune.cerege.fr/`

initial estimation of the pole by using either PHC or grid method and then a final estimation of the pole with the use of RARL2 software. A comparison for perfect and noisy synthetic data of the two initialization methods (PHC and grid) is provided at the end of this chapter.

Chapter 3: having the information of the estimated pole position we use different methods to recover the dipole location. In this chapter we describe a linear system method as well as methods with geometrical features namely the planes method, parabola method and circles method. The goal of this chapter is to understand the features of the described methods. We also conduct simulations with synthetic data in order to get a first idea for the performance of each method.

Chapter 4: this chapter is dedicated to resolve some issues regarding the circles method of chapter 3. Due to approximation and numerical errors the mathematical solution of a common intersection point of the circles method cannot be computed. For this reason we need to compute a pseudo-intersection point. To do that we use three different approaches namely the radical center, the minimization of the sum of the distances to three circles and the minimization of the sum of the squares of powers of a point with respect to given circles. At the end of the chapter we provide simulations with synthetic data and we discuss how we can combine the information from different measurement positions in order to compute a unique estimation for the dipole location.

Chapter 5: having an estimation for the dipole location we can focus now on the second problem which is the estimation of the strength and the direction of the magnetic dipole. We describe how we can approach this problem as a least min square problem. We also provide simulations with synthetic data. In this chapter we also conduct a comparison of the methods we decide to use in order to solve the problem.

Chapter 6: the last chapter of our thesis is dedicated to the conclusions, and the description of further work.

Notations

$\mathbf{B}_{[\mathbf{X_d},\mathbf{M_d}]}(\mathbf{X})$	macroscopic magnetic field
B_r, $B_\perp$, B_τ	magnetic field data which measured by the radial, vertical and tangential component of the magnetic field respectively
μ_0	magnetic permeability of free space
$\mathbf{M}_d = (M_1, M_2, M_3)$	magnetic source moment / dipole moment
$\mathbf{X}_d = (x_d, y_d, z_d)$	magnetic source location / dipole location
$\mathbf{X} = (x, y, z)$	point under study *e.g.* location of the pointwise magnetic field measurement
ξ_-	pole of our rational function / theoretical pole

In our study we adopt the following conventions for our notations.

- Symbols in **bold** represent vectors or matrices, unless otherwise indicated.
- Estimated quantities appear with a hat on top of the symbol *e.g.* $\hat{\mathbf{X}}_d$ denotes the estimation of the magnetic source location / dipole location.
- Notations with prime ($'$) referred to the scaled geometry of the unit circle $\mathbb{T}$, disc $\mathbb{D}$ or ball $\mathbb{B}$ depending the content of our analysis. For instance ξ'_- denotes the theoretical pole in the unit disc $\mathbb{D}$.

CHAPTER 1

Data acquisition process and physical models

1.1 Data acquisition process

In this section we describe the data acquisition process and the geometry that is correlated with it. Let's start with the nature of our measurements. Moon rocks have the ability to preserve magnetic information [9] in the form of remanent magnetization. This remanent magnetization generates a magnetic field around the rock. Geoscientists from Cerege conducted a survey by measuring the magnetic fields of 123 Moon rock samples [11] with the aim of recovering information on their magnetization. An additional difficulty in their work was the fact that the Moon rock samples from Apollo missions are located in NASA storage facilities and they cannot leave these facilities. This situation introduces some additional constraints such as the portability of the equipment used by geoscientists. For this reason they built a spinner magnetometer device which they call lunometer [10] see Figure 1.1. As a result the lunometer is a portable device and without many mechanical parts, this design resolves the transportation issues and at the same time protects the samples from chemical contamination. Lunometer performs measurements of the magnetic field in short time and without damaging the sample. It also has the ability to measure a variety of sample sizes and it can isolate the sample from the external environment with a mu-metal shield. Finally lunometer is sensitive enough to allow measurements of samples with weak magnetic field. As a side remark for the lunometer, geoscientists use a commercial three-axis fluxgate magnetic field sensor (Mag-03MS100[3] Bartington Instruments, Ltd.) which measures the components of the magnetic field B_r, $B_\perp$, B_τ namely the radical, vertical and tangential component

[3] http://www.bartingtondefenceandspace.com/presentation/mag-03-three-axis-magnetic-field-sensor

respectively at heights $[0, 0.015, 0.03]$. These specifications dictate the default setup of our experiments for which we usually use 3 sensors at heights $[0, 0.015, 0.03]$.

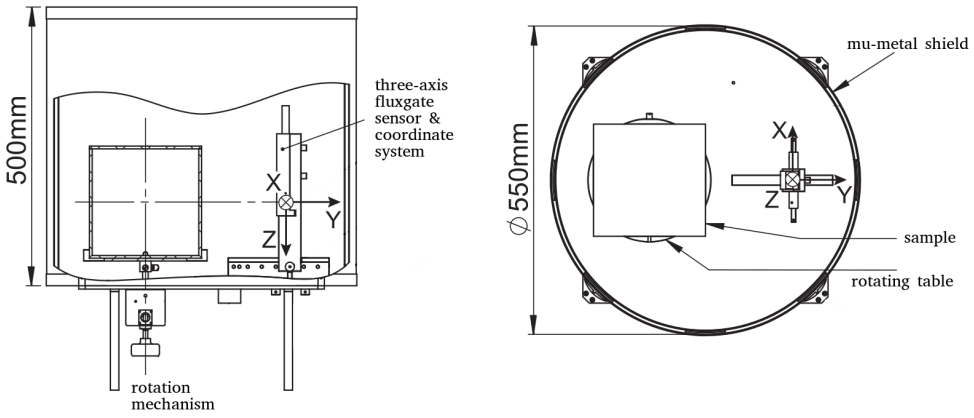

Figure 1.1: Schematic illustration of the magnetometer [10]. The picture on the left shows the side view of the magnetometer, while the picture on the right shows its top view. In both pictures one can see the rotation mechanism on top of which there is the rotation table and the acrylic cubic box which encloses the sample as well as the commercial three-axis fluxgate magnetic field sensor. This sensor measures each component of the magnetic field at different heights. The sample is isolated from the external environment with a two-layered mu-metal shield.

The measurement procedure is as follows:

- The sample is enclosed inside an acrylic cubic box. The size of the box can vary from five to twenty centimeters. The acrylic box is placed on top of a rotating table (deposition plate).
- A two-layered mu-metal shield is used to cancel the ambient field.
- A rotating mechanism, rotates the deposition plate. At every $0.7°$ the three components of the magnetic field are measured stepwise by the "three-axis" fluxgate sensor, note that the distance of the sensor from the cubic box center (which approximates the sample's mass center) is free to move from between five to thirty centimeters.
- After one or several full turns (for the sake of stacking) these operations are repeated two more times (3 measurement positions in total) with the sample placed in orthogonal positions on the rotating table.

Finally from those sparse measurements for one measurement position, we will have data on three circle sections on a cylindrical geometry see Figure 1.2. From those measurements we try to recover the dipole's position, direction and magnitude. The features of this cylindrical geometry will be explained in detail during our study.

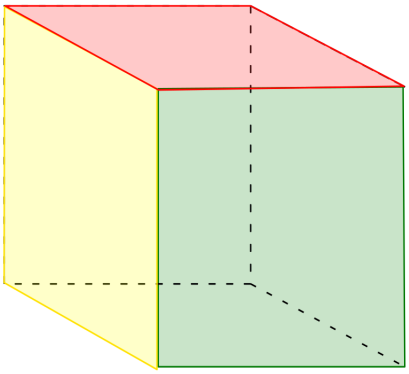

(a) This picture illustrates the surfaces of the cubic box (where the sample is enclosed) which are placed on the disposition plate.

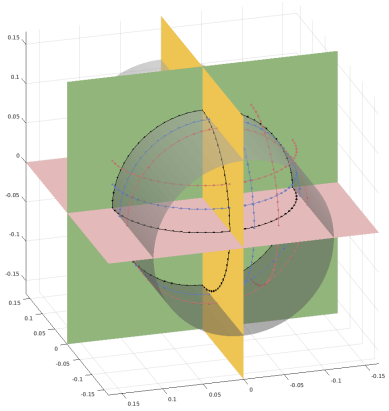

(b) This picture shows the data geometry of our measurements. The measurements are performed on three orthogonal cylinders; for each cylinder, data are indeed available at discrete points of three circles.

Figure 1.2: In both pictures we use the same color code to illustrate the measurement position. Position 1, is illustrated with red and the orthogonal positions 2 and 3, are illustrated with yellow and green respectively.

1.2 Physical framework

In our study we use the differential form of Maxwell's equations for the magnetic field, under the magnetostatic and macroscopic framework, see [18, ch. 5.8]:

$$\nabla \cdot \mathbf{B} = 0, \tag{1.1}$$

$$\nabla \times \mathbf{H} = \mathbf{J}, \tag{1.2}$$

where $\nabla\cdot$ is the divergence operator, $\nabla\times$ is the curl operator, $\mathbf{B}$ is the average of all magnetic flux regions of our volume (magnetic flux density), $\mathbf{H}$ is the averaged magnetic field and $\mathbf{J}$ is the total current density. Note that $\mathbf{B}$, $\mathbf{H}$, $\mathbf{J}$ are $\mathbb{R}^3$ valued quantities depending on space variables.

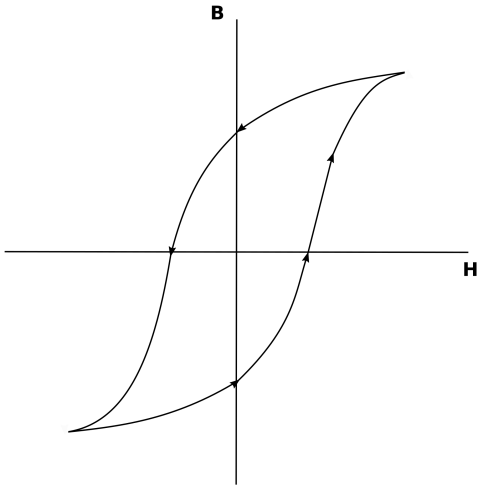

Figure 1.3: Illustration of hysteresis loop for a ferromagnetic material.

The link between the averaged magnetic field $\mathbf{H}$ and the averaged magnetic flux density $\mathbf{B}$ is given by the relation

$$\mathbf{H} = \frac{1}{\mu_0}\mathbf{B} - \mathbf{M}, \tag{1.3}$$

where $\mathbf{M}$ is the average macroscopic magnetization which is also called magnetic moment density, or magnetization. In ferromagnetic materials, $\mathbf{H}$ and $\mathbf{B}$ have a non linear relation which could be illustrated with the hysteresis loop, see Figure 1.3.
For hard ferromagnetic materials (such as iron) with a given magnetization $\mathbf{M}$ and $\mathbf{J} = 0$ we see in [18, ch. 5.9] that Equation (1.2) becomes

$$\nabla \times \mathbf{H} = 0. \tag{1.4}$$

Equation (1.4) implies that we can introduce a magnetic scalar potential Φ_M in [18, ch. 5.9 B] and [19, sec. 2.1]. Then the macroscopic magnetic field can be computed as

$$\mathbf{H} = -\nabla\Phi_M. \tag{1.5}$$

The idea of the scalar potential Φ_M computation is to use Equations (1.1) and (1.3). This leads us to the relation

$$\Delta\Phi_M = \nabla \cdot \mathbf{M}$$

which is a Poisson equation (with Δ we denote the Laplace operator $\nabla \cdot \nabla$). By using the Coulomb potential $\dfrac{1}{4\pi|\mathbf{X} - \mathbf{X}'|}$ as a fundamental solution of

$-\Delta$, the expression of the scalar magnetic potential Φ_M can be written as:

$$\Phi_M(\mathbf{X}) = -\frac{1}{4\pi}\int \frac{\nabla\cdot\mathbf{M}(\mathbf{X}')}{|\mathbf{X}-\mathbf{X}'|}d^3\mathbf{X}',$$

at points $\mathbf{X}\in\mathbb{R}^3$ that do not belong to the support of $\mathbf{M}$. Now having in mind that our magnetization is assumed to be pointwise we can use the Dirac impulsion δ for which we get that

$$\langle \mathbf{M}, 1\rangle = \langle \mathbf{M}_d\delta_{\mathbf{X}_d}, 1\rangle = \mathbf{M}_d\langle\delta_{\mathbf{X}_d}, 1\rangle = \mathbf{M}_d,$$

where $\mathbf{M}_d$ is the moment of the dipole. Following the computations in [19], we compute the gradient

$$\nabla\left(\frac{1}{|\mathbf{X}-\mathbf{X}'|}\right) = -\frac{\mathbf{X}-\mathbf{X}'}{|\mathbf{X}-\mathbf{X}'|^3}.$$

With these computations we can write the scalar potential as:

$$\Phi_M(\mathbf{X}) = -\frac{1}{4\pi}\int \frac{\nabla\cdot\mathbf{M}(\mathbf{X}')}{|\mathbf{X}-\mathbf{X}'|}d^3\mathbf{X}' = -\frac{1}{4\pi}\int \mathbf{M}(\mathbf{X}')\cdot\nabla\left(\frac{1}{|\mathbf{X}-\mathbf{X}'|}\right)d^3\mathbf{X}',$$

from which we get:

$$\Phi_M(\mathbf{X}) = \frac{1}{4\pi}\int \frac{\mathbf{M}(\mathbf{X}')\cdot(\mathbf{X}-\mathbf{X}')}{|\mathbf{X}-\mathbf{X}'|^3}d^3\mathbf{X}' = \frac{1}{4\pi}\frac{\mathbf{M}_d\cdot(\mathbf{X}-\mathbf{X}_d)}{|\mathbf{X}-\mathbf{X}_d|^3}. \tag{1.6}$$

Note that the right part of Equation (1.6) derives from our single dipole assumption.

Notation of our study: for a point $\mathbf{X}$ outside from the sample, Equation (1.3) is zero. In that case the magnetic flux density $\mathbf{B}$ and the magnetic field $\mathbf{H}$ are proportional to each other. In our study, by abuse of language, we call $\mathbf{B}$ sometimes as magnetic field. We use the notation $\mathbf{B}_{[\mathbf{X}_d,\mathbf{M}_d]}$ to recall that the magnetic source is a single dipole with location $\mathbf{X}_d$ and moment $\mathbf{M}_d$. Consequently the basic equation of our study which is based on a single dipole, quasi-static (time independent), magnetostatic, macroscopic approximation for ferromagnetic materials can be computed from the Expressions (1.5) and (1.6) from which we get:

$$\mathbf{B}_{[\mathbf{X}_d,\mathbf{M}_d]}(\mathbf{X}) = \mu_0\mathbf{H} = -\mu_0\nabla\Phi_M(\mathbf{X}) = -\mu_0\nabla\left(\frac{1}{4\pi}\frac{\mathbf{M}_d\cdot(\mathbf{X}-\mathbf{X}_d)}{|\mathbf{X}-\mathbf{X}_d|^3}\right). \tag{1.7}$$

Now what we have to do is to compute the gradient of Φ_M. We do the computations for the first element of the gradient vector which corresponds to the partial derivative of

$$-\frac{1}{4\pi}\frac{\mathbf{M}_d \cdot (\mathbf{X}-\mathbf{X}_d)}{|\mathbf{X}-\mathbf{X}_d|^3}$$

with respect to the first variable x_1 of $\mathbf{X} = (x_1, x_2, x_3)$; we can work with a similar way for the other two partial derivatives.

$$-\frac{1}{4\pi}\frac{\partial}{\partial x_1}\frac{\mathbf{M}_d \cdot (\mathbf{X}-\mathbf{X}_d)}{|\mathbf{X}-\mathbf{X}_d|^3} = -\frac{1}{4\pi}\frac{\partial}{\partial x_1}\frac{\begin{pmatrix} M_1 \\ M_2 \\ M_3 \end{pmatrix} \cdot \begin{pmatrix} x_1 - x_{d1} \\ x_2 - x_{d2} \\ x_3 - x_{d3} \end{pmatrix}}{((x_1-x_{d1})^2 + (x_2-x_{d2})^2 + (x_3-x_{d3})^2)^{\frac{3}{2}}}.$$

By computing the dot product and using the property of the derivative for division of functions $\left(\frac{f}{g}\right)' = \frac{f'g - fg'}{g^2}$ we get:

$$\begin{aligned}
&-\frac{1}{4\pi}\frac{\partial}{\partial x_1}\frac{M_1(x_1-x_{d1}) + M_2(x_2-x_{d2}) + M_3(x_3-x_{d3})}{((x_1-x_{d1})^2 + (x_2-x_{d2})^2 + (x_3-x_{d3})^2)^{\frac{3}{2}}} = \\
&= -\frac{1}{4\pi}\left(\frac{|\mathbf{X}-\mathbf{X}_d|^3 \frac{\partial}{\partial x_1}\left(M_1(x_1-x_{d1}) + M_2(x_2-x_{d2}) + M_3(x_3-x_{d3})\right)}{|\mathbf{X}-\mathbf{X}_d|^6} - \right. \\
&\left. \frac{[\mathbf{M}_d \cdot (\mathbf{X}-\mathbf{X}_d)]\frac{\partial}{\partial x_1}\left(\left((x_1-x_{d1})^2 + (x_2-x_{d2})^2 + (x_3-x_{d3})^2\right)^{\frac{3}{2}}\right)}{|\mathbf{X}-\mathbf{X}_d|^6}\right) = \\
&= -\frac{1}{4\pi}\frac{|\mathbf{X}-\mathbf{X}_d|^3 M_1 - [\mathbf{M}_d\cdot(\mathbf{X}-\mathbf{X}_d)]\frac{3}{2}|\mathbf{X}-\mathbf{X}_d|\frac{\partial}{\partial x_1}\left((x_1-x_{d1})^2+(x_2-x_{d2})^2+(x_3-x_{d3})^2\right)}{|\mathbf{X}-\mathbf{X}_d|^6} = \\
&= -\frac{1}{4\pi}\frac{|\mathbf{X}-\mathbf{X}_d|^3 M_1 - 3|\mathbf{X}-\mathbf{X}_d|[\mathbf{M}_d \cdot (\mathbf{X}-\mathbf{X}_d)](x_1-x_{d1})}{|\mathbf{X}-\mathbf{X}_d|^6} = \\
&= -\frac{1}{4\pi}\frac{|\mathbf{X}-\mathbf{X}_d|^2 M_1 - 3[\mathbf{M}_d \cdot (\mathbf{X}-\mathbf{X}_d)](x_1-x_{d1})}{|\mathbf{X}-\mathbf{X}_d|^5}.
\end{aligned}$$

Combining this result (together with the other two partial derivatives) and Equation (1.3) we get the expression of our main equation of our study which is:

$$\mathbf{B}_{[\mathbf{X}_d,\mathbf{M}_d]}(\mathbf{X}) = -\frac{\mu_0}{4\pi}\frac{|\mathbf{X}-\mathbf{X}_d|^2\mathbf{M}_d - 3[\mathbf{M}_d \cdot (\mathbf{X}-\mathbf{X}_d)](\mathbf{X}-\mathbf{X}_d)}{|\mathbf{X}-\mathbf{X}_d|^5}. \quad (1.8)$$

1.3 Magnetic source models

There are two main categories of magnetic source models, namely dipolar [20, 21] and multipolar [22]. In literature the assumption of point like

magnetic sources is common for both of these categories. For each category we can have models which concern a single source [20] or many sources [21]. Depending on the model, the magnetic source could be located at the origin of the coordinate system or elsewhere. For instance geoscientists in Cerege study a dipolar model with a single dipole assumption which is located at the origin of their coordinate system [10]. Similarly in our study we also use a dipolar model with a single dipole assumption but our source could be located at any place in our coordinate system, limited only by the sample's physical size. It is worth mentioning that there exist also hybrid models like in [23] which assume first dipolar dominant sources and then use multipolar expansion.
Note that the data from the magnetic field measurements are independent of the model we use. In our case we use the assumption that the field can be explained by only one magnetic dipole in the sample. This assumption has meaning if the sample is uniformly magnetized or if the sample is globally not magnetic, except for a small grain somewhere. In these cases the hypothesis of a single magnetic dipole could be a good approximation of the rock's generated field. Of course it is possible that the data cannot be explained by only one dipole. In that case the role of our algorithm is to tell us that our hypothesis of a single dipole is not valid.

1.4 Framework for simulations with synthetic data

In the following chapters we conduct simulations with synthetic data in order to test the methods we develop. For this reason it is useful to describe here the frameworks of those simulations. We design the experiments in such a way that, in the ideal case, the data acquisition process corresponds to data without noise generated from exactly one magnetic dipole with moment $\mathbf{M}_d$ at location $\mathbf{X}_d$ (perfect data, based on our assumption). To do that, we generate arbitrary dipole locations $\mathbf{X}_d$ and moments $\mathbf{M}_d$. There are two main frameworks based on which we can categorize our experiments.

Framework for arbitrary dipoles uniformly spread in a restricted volume: for this framework of experiments we define the shape of a volume, such as a cylinder or a ball. The generated dipoles of those experiments are uniformly spread inside the volume. For instance in Figure 1.4 one can see the dipole locations of 2000 experiments uniformly spread inside a ball of radius $r = 0.14$.

Framework for arbitrary dipoles uniformly spread on cylinders: for this framework we define specific cylinders with radii evenly spaced between 0 and R where R denotes the distance of the sensors from the revolution axis. In these experiments the dipoles are uniformly spread on the

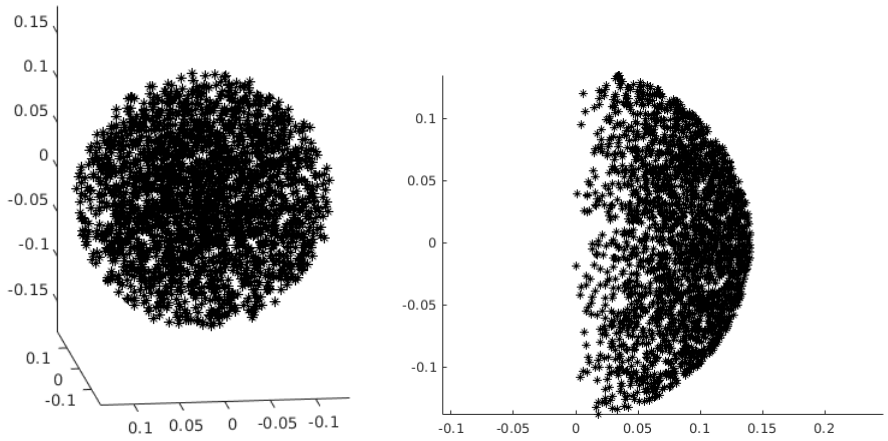

(a) (b)

Figure 1.4: The picture on the left illustrates a general 3D view of 2000 dipole locations uniformly generated in a ball of radius $r = 0.14$. The picture on the right is the 2D side view of the same 2000 dipole locations containing the information $(|x_d + \mathrm{i}y_d|, z_d)$. In both pictures the dipole locations are illustrated as black stars.

surface of each cylinder and are vertically ranging from $-R$ to R. For instance Figure 1.5 illustrates the case with $R = 0.111$ for 10 different cylinders with 100 generated dipoles on each surface hence 1000 dipole locations in total. Note that every cylindrical surface has the same number of generated dipoles.

For each framework we generate arbitrary moments $\mathbf{M}_d$ for the dipoles (by default we generate one moment). For the moments we specify their strength, namely their modulus. The moments directions are randomly chosen (uniformly) on a sphere. For instance, if we generate 30 moments $\mathbf{M}_d$ with modulus one, for a dipole location, we will end up with 30 different dipoles which are all located at the same $\mathbf{X}_d$ location. Figure 1.6 shows the directions of the moments for a case like that.

Extra parameters of our experiments

Noise: note also that we have the ability to introduce noise into our measurements. There are two kinds of noise we can use, the angular noise which adds inaccuracy to the sensors's locations and signal noise which is additive noise on the magnetic field measurements.

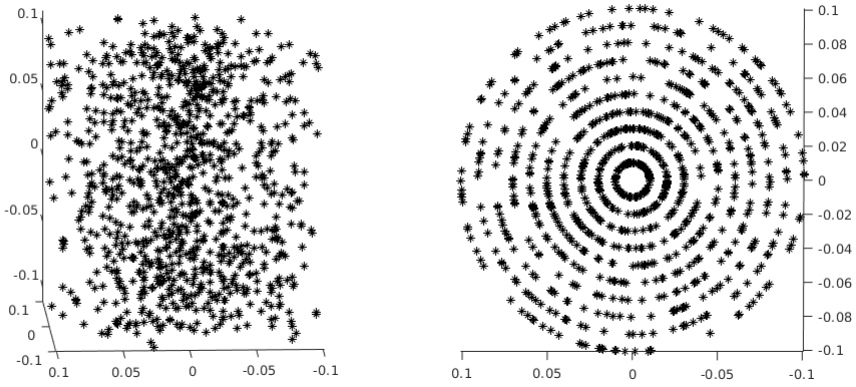

(a) (b)

Figure 1.5: The picture on the left illustrates a general 3D view of 1000 dipole locations generated on the surface of 10 concentric cylinders. The picture on the right is a top view of the same 1000 dipoles locations, here the radius of the cylinders are more visible. In both pictures the dipole locations are illustrated as black stars.

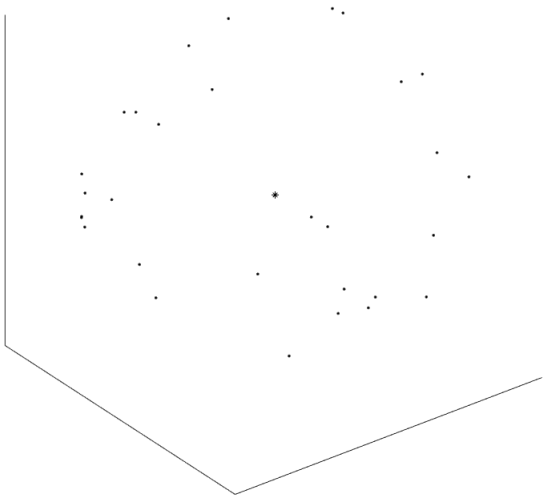

Figure 1.6: The black star illustrates one arbitrary dipole location $\mathbf{X}_d$. For this dipole location, 30 different moments $\mathbf{M}_d$ were generated and their direction starts from the black star and continues to the black dots. Note that a setup like this generates 30 different dipoles for our experiments.

Number of sensors: another degree of freedom in our experiments is that we can simulate measurements with a different number of sensors and

place them at various heights. This is important because geoscientists are interested in seeing if a new version of a lumometer with multiple sensors could provide us with better estimations for the sample's magnetization.

Sensors distance R from the revolution axis: in many simulations we set $R = 0.15$ meters, this distance is the default distance used by geoscientists in Cerege. Recall that the distance of the lunometer sensors can vary between $R = 0.05$ to $R = 0.3$ meters.

Measurement positions: another parameter of our experiments is the number of measurement positions. By default we use three different orthogonal positions. At each position the lunometer performs measurements on circular sections for each component of the magnetic field $\mathbf{B}_{[\mathbf{X}_d,\mathbf{M}_d]}$ at different heights which form a cylindrical geometry see Figure 1.2.

1.5 Setups of experiments

In the following chapters 2, 3, 4 and 5 we conduct simulations with synthetic data. In this section we collect all the setups of our experiments to come and we explain their characteristics. We do that for two reasons: the first reason is to help the reader with a handy reference, so one can find easily the experiments setup and the second reason, is to provide enough information for other researchers in order to reproduce our experiments and test our claims.

Descriptions of the setup of our experiments

For the selected synthetic data experiments, we set (for all of them) the sensors measurement distance from the revolution axis at $R = 0.15$, the measurement step at 1° and the moment strength at 0.001 Am^2. We also present experiments without angular noise, we do that because we observe that with the selected method of study, the angular noise does not affect significantly our results. We divide the experiments into five groups as follows.

First group of experiments: this group of synthetic data experiments consists of 4000 dipoles. To get them, we first generate 4000 radii evenly spread between 0 and R and select randomly only one dipole per cylinder surface and the cylinders are vertically ranging from $-R$ to R. The measurements are taken for a single measurement position and the three sensors are all located at the same height. The following tables show the information of these setups.

Table 1.1: Setup

# of cylinders	# of dipoles per cylinder surface	Total # of dipoles
4000	1	4000
# of generated moments	# of measurement positions	signal noise
1	1	0%
# of sensors	heights	type of sensor
3	0.015, 0.015, 0.015	B_r, $B_\perp$, B_τ

Table 1.2: Setup

# of cylinders	# of dipoles per cylinder surface	Total # of dipoles
4000	1	4000
# of generated moments	# of measurement positions	signal noise
1	1	5%
# of sensors	heights	type of sensor
3	0.015, 0.015, 0.015	B_r, $B_\perp$, B_τ

Second group of experiments: this group of experiments consists of 6000 dipoles, which are generated on the surfaces of 15 concentric cylinders whose radii are evenly distributed between 0 and R (400 dipoles per surface). Once again the cylinders are vertically ranging from $-R$ to R. This group also concerns data from a single measurement position. The sensors of these experiments are located at different heights.

Table 1.3: Setup

# of cylinders	# of dipoles per cylinder surface	Total # of dipoles
15	400	6000
# of generated moments	# of measurement positions	signal noise
1	1	0%
# of sensors	heights	type of sensor
3	0, 0.015, 0.03	B_r, $B_\perp$, B_τ

Table 1.4: Setup

# of cylinders	# of dipoles per cylinder surface	Total # of dipoles
15	400	6000
# of generated moments	# of measurement positions	signal noise
1	1	0%
# of sensors	heights	type of sensor
11	$-0.075, -0.06, -0.045, -0.030,$ $-0.015, 0, 0.015, 0.030,$ $0.045, 0.06, 0.075$	$B_\tau, B_\perp, B_r, B_\tau,$ $B_\perp, B_r, B_\perp, B_\tau,$ $B_r, B_\perp, B_\tau$

Table 1.5: Setup

# of cylinders	# of dipoles per cylinder surface	Total # of dipoles
15	400	6000
# of generated moments	# of measurement positions	signal noise
1	1	0%
# of sensors	heights	type of sensor
9	$0, 0.015, 0.03$ $0, 0.015, 0.03$ $0, 0.015, 0.03$	$B_r, B_\perp, B_\tau$ $B_r, B_\perp, B_\tau$ $B_r, B_\perp, B_\tau$

Third group of experiments: this group of experiments consists of 6000 dipoles, which are uniformly generated inside a ball with radius $r = 0.14$. This group concerns data from all three measurement positions, hence it is a complete data set. The sensors in these experiments are located at different heights.

Table 1.6: Setup

volume	# of dipoles	Total # of dipoles
ball of radius 0.14	6000	6000
# of generated moments	# of measurement positions	signal noise
1	3	0%
# of sensors	heights	type of sensor
3	$0, 0.015, 0.03$	$B_r, B_\perp, B_\tau$

Table 1.7: Setup

volume	# of dipoles	Total # of dipoles
ball of radius 0.14	6000	6000
# of generated moments	# of measurement positions	signal noise
1	3	0%
# of sensors	heights	type of sensor
11	$-0.075, -0.06, -0.045, -0.030,$ $-0.015, 0, 0.015, 0.030,$ $0.045, 0.06, 0.075$	$B_\tau, B_\perp, B_r, B_\tau,$ $B_\perp, B_r, B_\perp, B_\tau,$ $B_r, B_\perp, B_\tau$

Table 1.8: Setup

volume	# of dipoles	Total # of dipoles
ball of radius 0.14	6000	6000
# of generated moments	# of measurement positions	signal noise
1	3	5%
# of sensors	heights	type of sensor
3	$0, 0.015, 0.03$	$B_r, B_\perp, B_\tau$

Table 1.9: Setup

volume	# of dipoles	Total # of dipoles
ball of radius 0.14	6000	6000
# of generated moments	# of measurement positions	signal noise
1	3	5%
# of sensors	heights	type of sensor
11	$-0.075, -0.06, -0.045, -0.030,$ $-0.015, 0, 0.015, 0.030,$ $0.045, 0.06, 0.075$	$B_\tau, B_\perp, B_r, B_\tau,$ $B_\perp, B_r, B_\perp, B_\tau,$ $B_r, B_\perp, B_\tau$

Fourth group of experiments: in these experiments we study the effect of the dipole moment. For this reason we use three selected dipole locations of the Setup 1.6. More precisely we use the $\mathbf{X}_d(4) = [0.0228, -0.1080, 0.0690]$,

$\mathbf{X}_d(5) = [-0.0526, -0.0529, -0.0838]$ and $\mathbf{X}_d(6) = [0.0519, 0.1101, -0.0668]$ locations which correspond to the 4^{th}, 5^{th} and 6^{th} experiments location of Setup 1.6. For these cases we generate 1000 moments that varies randomly on a sphere around each $\mathbf{X}_d$. Finally we use the current lunometer configuration and 3 measurement positions for our experiments.

Table 1.10: Setup

	# of dipoles	Total # of dipoles
	3	3000
# of generated moments	# of measurement positions	signal noise
1000	3	0%
# of sensors	heights	type of sensor
3	$0, 0.015, 0.030$	$B_r, B_\perp, B_\tau$

Fifth group of experiments: here we have measurements from a single measurement position. For these experiments we use 1000 dipoles uniformly spread inside a ball of radius $r = 0.14$ and we use a single type of sensor ($B_\perp$) to take the measurements, but at eleven different heights.

Table 1.11: Setup

volume	# of dipoles	Total # of dipoles
ball of radius 0.14	1000	1000
# of generated moments	# of measurement positions	signal noise
1	1	5%
# of sensors	heights	type of sensor
11	$-0.075, -0.06, -0.045, -0.030,$ $-0.015, 0, 0.015, 0.030,$ $0.045, 0.06, 0.075$	$B_\perp, B_\perp, B_\perp, B_\perp,$ $B_\perp, B_\perp, B_\perp, B_\perp,$ $B_\perp, B_\perp, B_\perp$

CHAPTER 2

Approximation methods in 2D and their link with the dipole location

In Chapter 1, we saw the data acquisition process and the physical model of our study. In this chapter, we start dealing with our first subproblem, namely the estimation of the dipole location $\mathbf{X}_d$. More precisely we see how we can manipulate the information we get from the pointwise measurements of the components of the magnetic field $\mathbf{B}_{[\mathbf{X}_d,\mathbf{M}_d]}$, in order to extract useful information for the dipole location $\mathbf{X}_d$. Our strategy is to work in a 2D space instead of a 3D one. We can do this by focusing our study on the measurements from a single component of the magnetic field $\mathbf{B}_{[\mathbf{X}_d,\mathbf{M}_d]}$ (radial, tangential or vertical) which are taken on a single measurement plane, at sensors locations on a circle. Our first goal for this chapter is to explain how our reduced 2D problem is linked with rational functions and essentially with a pole estimation inside the unit disk $\mathbb{D}$. This approach was inspired by the article [21].
Such pole estimates, actually available for the field components at different heights and in 3 orthogonal directions, will allow us to compute an estimate of the dipole location $\mathbf{X}_d$ in Chapter 4.
Note that in this chapter we explain how to treat the available signal and what is the physical model of our study. Then we use Grid and PHC methods in order to initialize properly RARL2 which is the software that provides us with a pole estimation inside the unit disk $\mathbb{D}$. Finally we do a comparison between the Grid and PHC methods.

2.1 Measurement treatment

Let us consider one section of measurements, take for instance measurements from position 1 (where by convention the cubic box is seated on the $0xy$ plane, for the other two measurement positions the cubic box is seated on

the $0xz$ and $0yz$ planes respectively). From the data acquisition process in Chapter 1, we saw that the measurements of a magnetic field component are taken on a circular path around the sample, with revolution axis $0z$ which passes through the center of the acrylic box where the sample is enclosed. The sample is placed inside the acrylic box in such a way that the revolution axis of each measurement position passes near its mass center, with this way the origin of our coordinate system is a rough approximation of the rock's mass center. Because we want to work on the unit circle $\mathbb{T}$, we scale the geometry of our data. We do that by dividing with R the distance between the revolution axis and the sensors location see Figure 2.1.

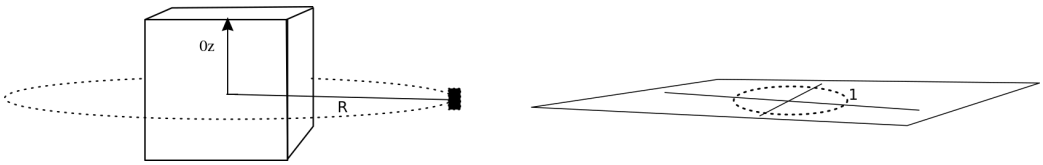

Figure 2.1: The picture on the left illustrates the actual geometry of our data acquisition process, for a single magnetic field component. The black rectangle illustrates the sensor's location. The distance of the sensor from the revolution axis $0z$ is R. The picture on the right illustrates the 2D scaled geometry of our study, which is on the complex plane. The dashed circle on the right picture is the unit circle $\mathbb{T}$. In both pictures, the available measurements are given at points located on the dashed circles.

Now there are two kinds of information we need to scale: the sensor's locations at specific points $\mathbf{X} = (x, y, z)$, and the unknown dipole location $\mathbf{X}_d = (x_d, y_d, z_d)$. As we did in paper [20], we introduce the complex number $\xi = x + \mathrm{i}\, y$, where $\mathrm{i} \in \mathbb{C}$ is the imaginary number $\mathrm{i}^2 = -1$, so that the measurements on the actual geometry are indeed known for values of ξ that all satisfy $|\xi| = R$. Accordingly, we introduce the complex number $\xi_d = x_d + \mathrm{i}\, y_d$. Moreover the magnetic source that we are looking for is necessarily inside the sample, which is itself inside the cubic box surrounded by the circles of radius R where the sensors lie. This implies that $|z_d| < R$ and $|\xi_d| < R$.

We scale our information by dividing by R. Hence in our scaled geometry we have

$$\xi' := x' + \mathrm{i}y' := \frac{x + \mathrm{i}\, y}{R} = \frac{\xi}{R}, \;\; h := \frac{z}{R}, \;\; \xi'_d := x'_d + \mathrm{i}\, y'_d := \frac{x_d + \mathrm{i}\, y_d}{R}, \;\; h_d := \frac{z_d}{R}.$$

Now, for any ξ' satisfying $|\xi'| = 1$ we have $\overline{\xi'} = 1/\xi'$. We also have that $|h_d| < 1$ and $|\xi'_d| < 1$.

2.1.1 Raw data

Our analysis starts with the available data. Let us denote by b_{rj}, $b_{\perp j}$ and $b_{\tau j}$ respectively the values of the radial, vertical and tangential components of $\mathbf{B}_{[\mathbf{X}_d,\mathbf{M}_d]}$ at sensors locations (x_j, y_j, h), where $x_j + \mathrm{i}y_j = \xi_j = R\,\xi'_j = R\,e^{\mathrm{i}\theta_j}$, for $j = 1, ..., N = 360$, the number of pointwise measurements.

2.1.2 Rational function of the physical model

To continue our study we are taking advantage of the measurements of the components of the magnetic field $\mathbf{B}_{[\mathbf{X}_d,\mathbf{M}_d]}(\mathbf{X}) \in \mathbb{R}$ (radial, tangential or vertical) at point $\mathbf{X} = (x, y, z)$ with (x, y) on a circular path.

In our work in [20] we saw that if $\mathbf{c} = (c_1, c_2, c_3)$ is an arbitrary vector of $\mathbb{R}^3$ with $\gamma = c_1 + \mathrm{i}\,c_2$, and observing that $x' = x/R = (\xi' + \overline{\xi'})/2$ and $y' = y/R = (\xi' - \overline{\xi'})/(2\mathrm{i})$, we have, for any ξ' satisfying $|\xi'| = 1$,

$$\begin{aligned}
\frac{\mathbf{X}}{R} \cdot \mathbf{c} &= \frac{x}{R}c_1 + \frac{y}{R}c_2 + \frac{z}{R}c_3 \\
&= \frac{\xi' + \overline{\xi'}}{2}c_1 + \frac{\xi' - \overline{\xi'}}{2\mathrm{i}}c_2 + hc_3 \\
&= \frac{1}{2\xi'}\left(\xi'^2 c_1 + c_1 - \mathrm{i}\xi'^2 c_2 + \mathrm{i}c_2 + 2hc_3\xi'\right) \\
&= \frac{1}{2\xi'}\left((c_1 - \mathrm{i}c_2)\xi'^2 + 2c_3 h\xi' + (c_1 + \mathrm{i}c_2)\right) \\
&= \frac{1}{2\xi'}\left(\overline{\gamma}\,\xi'^2 + 2\,c_3 h\,\xi' + \gamma\right). \qquad (2.1)
\end{aligned}$$

Now, the measurement available at point $\mathbf{X}$ is $\mathbf{B}_{[\mathbf{X}_d,\mathbf{M}_d]}(\mathbf{X}) \cdot \mathbf{v}$ with $\mathbf{v}$ being either $\mathbf{v}_\perp = (0, 0, 1)$ or $\mathbf{v}_r = (x/R, y/R, 0)$ or $\mathbf{v}_\tau = (-y/R, x/R, 0)$ (vertical, radial or tangential respectively) with directions as illustrated in the figure below.

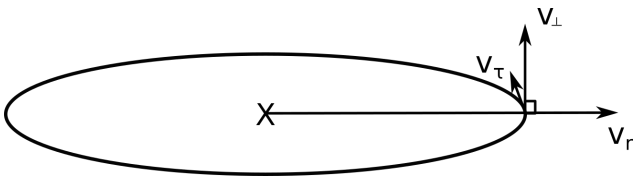

Figure 2.2: Illustration of the direction of the vectors $\mathbf{v}_\perp = (0, 0, 1)$, $\mathbf{v}_r = (x/R, y/R, 0)$ and $\mathbf{v}_\tau = (-y/R, x/R, 0)$.

Observing that

$$\begin{aligned}
&\mathbf{X}\cdot\mathbf{v}_\perp = z,\\
&\mathbf{X}\cdot\mathbf{v}_r = R,\\
&\mathbf{X}\cdot\mathbf{v}_\tau = 0,\\
&\mathbf{v}_\perp\cdot\mathbf{c} = c_3,\\
&\mathbf{v}_r\cdot\mathbf{c} = \frac{\mathbf{X}}{R}\cdot(c_1,c_2,0),\\
&\mathbf{v}_\tau\cdot\mathbf{c} = \frac{\mathbf{X}}{R}\cdot(c_2,-c_1,0)
\end{aligned} \tag{2.2}$$

we can conduct the computations for the quantities $\mathbf{B}_{[\mathbf{X}_d,\mathbf{M}_d]}(\mathbf{X})\cdot\mathbf{v}$.
Note that the denominator as well as the terms $|\mathbf{X}-\mathbf{X}_d|^2$ and $\mathbf{M}_d\cdot(\mathbf{X}-\mathbf{X}_d)$ are common for each measurement component.
Let's investigate the structure of $\mathbf{B}_{[\mathbf{X}_d,\mathbf{M}_d]}(\mathbf{X})\cdot\mathbf{v}$.

Study of the radial component: the first measurement component of the magnetic field which we study is the radial one. In this case our main equation namely Equation (1.8) takes the form:

$$\mathbf{B}_{[\mathbf{X}_d,\mathbf{M}_d]}(\mathbf{X})\cdot\mathbf{v}_r = -\frac{\mu_0}{4\pi}\,\frac{|\mathbf{X}-\mathbf{X}_d|^2\,(\mathbf{M}_d\cdot\mathbf{v}_r) - 3\,[\mathbf{M}_d\cdot(\mathbf{X}-\mathbf{X}_d)]\,((\mathbf{X}-\mathbf{X}_d)\cdot\mathbf{v}_r)}{(|\mathbf{X}-\mathbf{X}_d|^2)^{\frac{5}{2}}}.$$

Observe that the denominator contains the same quantity as the first term of the numerator but with a different power. Because of that we can focus our study on the numerator and simultaneously extract some information for the denominator. Let's investigate now the structure of expression $\mathbf{B}_{[\mathbf{X}_d,\mathbf{M}_d]}(\mathbf{X})\cdot\mathbf{v}_r$ for the radial component of our magnetic field. The analysis of the numerator terms is the following:

- $|\mathbf{X}-\mathbf{X}_d|^2 = |\xi-\xi_d|^2 + (z-z_d)^2 = R^2\left[(\xi'-\xi'_d)(\overline{\xi'}-\overline{\xi'}_d) + (h-h_d)^2\right]$.
  In the scaled geometry on the unit circle $\mathbb{T}$ it holds that $|\xi'|^2 = \xi'\overline{\xi'} = 1$, hence we get:

  $$|\mathbf{X}-\mathbf{X}_d|^2 = -\frac{R^2}{\xi'}\left[\overline{\xi'}_d\xi'^2 - (1+|\xi'_d|^2+(h-h_d)^2)\xi' + \xi'_d\right] = -\frac{R^2}{\xi'}p(\xi'),$$

  where the expression inside the bracket is a polynomial

  $$p(\xi') = \overline{\xi'}_d\xi'^2 - (1+|\xi'_d|^2+(h-h_d)^2)\xi' + \xi'_d$$

  of degree less or equal to two.

- Let

  $$\mathbf{M}_d = \begin{pmatrix} M_1\\ M_2\\ M_3\end{pmatrix}.$$

From the 5^{th} equation of Equations (2.2) we have that $\mathbf{M}_d \cdot \mathbf{v}_r = \frac{\mathbf{X}}{R} \cdot (M_1, M_2, 0)$ and from Equation (2.1) we get that

$$\mathbf{M}_d \cdot \mathbf{v}_r = \frac{1}{2\xi'} \left[(M_1 - \mathrm{i}M_2)\xi'^2 + (M_1 + \mathrm{i}M_2) \right],$$

where the expression inside the bracket is a polynomial of variable ξ' of degree less or equal to two.

- $\mathbf{M}_d \cdot (\mathbf{X} - \mathbf{X}_d) = \mathbf{M}_d \cdot \mathbf{X} - \mathbf{M}_d \cdot \mathbf{X}_d$ and by using the scaled geometry we get that:

$$\mathbf{M}_d \cdot (\mathbf{X} - \mathbf{X}_d) = R \left[\begin{pmatrix} M_1 \\ M_2 \\ M_3 \end{pmatrix} \cdot \begin{pmatrix} x' \\ y' \\ h \end{pmatrix} - \begin{pmatrix} M_1 \\ M_2 \\ M_3 \end{pmatrix} \cdot \begin{pmatrix} x'_d \\ y'_d \\ h_d \end{pmatrix} \right]$$

and with the use of Equation (2.1) we get

$$\mathbf{M}_d \cdot (\mathbf{X} - \mathbf{X}_d) = \frac{R}{2\xi'}[(M_1 - \mathrm{i}M_2)\xi'^2 + 2M_3 h\xi' + (M_1 + \mathrm{i}M_2) - 2\xi'(M_1 x'_d + M_2 y'_d + M_3 h_d)]$$

$$= \frac{R}{2\xi'}[(M_1 - \mathrm{i}M_2)\xi'^2 + 2(-M_1 x'_d - M_2 y'_d + M_3(h - h_d))\xi' \quad + (M_1 + \mathrm{i}M_2)],$$

where the expression inside the bracket is a polynomial of variable ξ' of degree less or equal to two.

- $(\mathbf{X} - \mathbf{X}_d) \cdot \mathbf{v}_r = \mathbf{X} \cdot \mathbf{v}_r - \mathbf{X}_d \cdot \mathbf{v}_r$, by using the 2^{nd} and 5^{th} equations of Equations (2.2) we get that:

$$(\mathbf{X} - \mathbf{X}_d) \cdot \mathbf{v}_r = R - \frac{\mathbf{X}}{R} \cdot (x_d, y_d, 0).$$

Now from Equation (2.1) we have

$$\begin{aligned} (\mathbf{X} - \mathbf{X}_d) \cdot \mathbf{v}_r &= \frac{2\xi' R}{2\xi'} - \frac{R}{2\xi'} \left((x'_d - \mathrm{i}y'_d)\xi'^2 + x'_d + \mathrm{i}y'_d \right) \\ &= \frac{R}{2\xi'} \left(2\xi' - (x'_d - \mathrm{i}y'_d)\xi'^2 + x'_d + \mathrm{i}y'_d \right) \end{aligned}$$

where the expression inside the bracket is a polynomial of variable ξ' of degree less or equal to two.

By doing computations on the numerator with moment (M_1, M_2, M_3) and defining $\Delta_h = h - h_d$, we end up with a polynomial $\kappa(\xi')$ of degree less or equal to four as follows.

$$\kappa(\xi') = a_r + b_r\xi' + c_r\xi'^2 + \overline{b_r}\xi'^3 + \overline{a_r}\xi'^4,$$

with coefficients:

$$
\begin{aligned}
a_r &= \frac{1}{4}(x'_d + \mathrm{i}y'_d)M_1 + \frac{1}{4}(\mathrm{i}x'_d - y'_d)M_2, \\
b_r &= \frac{1}{2}(-2 + \Delta_h^2 - 2{x'_d}^2 + {y'_d}^2 - 3\mathrm{i}x'_d y'_d)M_1 + \\
&\quad + \frac{\mathrm{i}}{2}(-2 + \Delta_h^2 + {x'_d}^2 - 2{y'_d}^2 + 3\mathrm{i}x'_d y'_d)M_2 + \frac{3}{2}\Delta_h(x'_d + \mathrm{i}y'_d)M_3, \\
c_r &= \frac{7}{2}(x'_d M_1 + y'_d M_2) - 3\Delta_h M_3.
\end{aligned}
$$

At the same time the denominator consists in a second degree polynomial $p(\xi')$ to the power of $5/2$. Let us denote the structure $\mathbf{B}_{[\mathbf{X}_d,\mathbf{M}_d]}(\mathbf{X}) \cdot \mathbf{v}_r$ by the function $f_r(\xi')$ as follows:

$$
f_r(\xi') = -\frac{\mu_0}{4\pi}\frac{R^2}{{\xi'}^2}\frac{\kappa(\xi')}{\left(-\frac{R^2}{\xi'}p(\xi')\right)^{\frac{5}{2}}}. \tag{2.3}
$$

Note that $f_r(\xi')$ is not a rational function, due to the denominator's square root. This introduces some difficulties because it is harder to compute the branch point of $f_r(\xi')$ inside the unit disk $\mathbb{D}$ than the poles of a rational function. However by squaring both sides of Equation (2.3) we get that:

$$
f_r^2(\xi') = -\frac{\mu_0^2}{16\pi^2 R^6}\frac{\xi'\kappa^2(\xi')}{p^5(\xi')}, \tag{2.4}
$$

which is a rational function.
We can work in a similar way for the components $\mathbf{B}_{[\mathbf{X}_d,\mathbf{M}_d]}(\mathbf{X}) \cdot \mathbf{v}_\tau$ and $\mathbf{B}_{[\mathbf{X}_d,\mathbf{M}_d]}(\mathbf{X}) \cdot \mathbf{v}_\perp$ as follows.

Study of the tangential component: the terms we have to compute in order to study the structure of the tangential magnetic field component $\mathbf{B}_{[\mathbf{X}_d,\mathbf{M}_d]}(\mathbf{X}) \cdot \mathbf{v}_\tau$ are the following:

- $\mathbf{M}_d \cdot \mathbf{v}_\tau$: from the 6^{th} equation of Equations (2.2) we get that:

  $$
  \mathbf{M}_d \cdot \mathbf{v}_\tau = \frac{\mathbf{X}}{R} \cdot (M_2, -M_1, 0),
  $$

  and from Equation (2.1) we get that

  $$
  \mathbf{M}_d \cdot \mathbf{v}_\tau = \frac{1}{2\xi'}\left[(M_2 + \mathrm{i}M_1){\xi'}^2 + (M_2 - \mathrm{i}M_1)\right],
  $$

  where the expression inside the bracket is a polynomial of variable ξ' of degree less or equal to two.

- $(\mathbf{X}-\mathbf{X}_d)\cdot\mathbf{v}_\tau = \mathbf{X}\cdot\mathbf{v}_\tau - \mathbf{X}_d\cdot\mathbf{v}_\tau$, by using 3^{rd} and 6^{th} equations of Equations (2.2) and Equation (2.1) we get that:

$$(\mathbf{X}-\mathbf{X}_d)\cdot\mathbf{v}_\tau = 0 - \frac{\mathbf{X}}{R}\cdot(y,-x,0) = -\frac{R}{2\xi'}\left((y'_d+\mathrm{i}x'_d)\xi'^2 + (y'_d-\mathrm{i}x'_d)\right),$$

  where the expression inside the bracket is a polynomial of variable ξ' of degree less or equal to two.

As before, by doing computations on the numerator with moment (M_1, M_2, M_3) and defining $\Delta_h = h - h_d$, we end up with a polynomial $\theta(\xi')$ of degree less or equal to four.

$$\theta(\xi') = a_\tau + b_\tau\xi' + c_\tau\xi'^2 + \overline{b_\tau}\xi'^3 + \overline{a_\tau}\xi'^4,$$

with coefficients:

$$\begin{aligned}
a_\tau &= \frac{1}{4}(-\mathrm{i}x'_d + y'_d)M_1 + \frac{1}{4}(x'_d + \mathrm{i}y'_d)M_2,\\
b_\tau &= \frac{\mathrm{i}}{2}(-1-\Delta_h^2 + 2x_d'^2 - y_d'^2 + 3\mathrm{i}y'_dx'_d)M_1 +\\
&\quad + \frac{1}{2}(1+\Delta_h^2 + x_d'^2 - 2y_d'^2 + 3\mathrm{i}x'_dy'_d)M_2 + \frac{3}{2}\Delta_h(-\mathrm{i}x'_d + y'_d)M_3,\\
c_\tau &= \frac{5}{2}(y'_dM_1 - x'_dM_2).
\end{aligned}$$

As before we compute a (non rational) function

$$f_\tau(\xi') = -\frac{\mu_0}{4\pi}\frac{R^2}{\xi'^2}\frac{\theta(\xi')}{\left(-\frac{R^2}{\xi'}p(\xi')\right)^{\frac{5}{2}}},$$

for the $\mathbf{B}_{[\mathbf{X}_d,\mathbf{M}_d]}(\mathbf{X})\cdot\mathbf{v}_\tau$ structure. By squaring both sides of the above function we get the rational function:

$$f_\tau^2(\xi') = -\frac{\mu_0^2}{16\pi^2R^6}\frac{\xi'\theta^2(\xi')}{p^5(\xi')}. \tag{2.5}$$

Study of the vertical component: the last structure we have to study concerns the measurements of the vertical magnetic field component $\mathbf{B}_{[\mathbf{X}_d,\mathbf{M}_d]}(\mathbf{X})\cdot\mathbf{v}_\perp$. Here we need to compute the terms:

- $\mathbf{M}_d\cdot\mathbf{v}_\perp = \begin{pmatrix} M_1\\ M_2\\ M_3\end{pmatrix}\cdot\begin{pmatrix}0\\0\\1\end{pmatrix} = M_3,$

  which is a constant and

- $(\mathbf{X} - \mathbf{X}_d) \cdot \mathbf{v}_\perp = \mathbf{X} \cdot \mathbf{v}_\perp - \mathbf{v}_\perp \cdot \mathbf{X}_d = R(h - h_d)$,
  which comes from the 1^{st} and 4^{th} equations of Equations (2.2) and it is a constant too.

As a result this time the numerator computations with moment (M_1, M_2, M_3) and $\Delta_h = h - h_d$ provides us with a polynomial $s(\xi')$ of degree less or equal to two.

$$s(\xi') = a_\perp + b_\perp \xi' + \overline{a_\perp} \xi'^2,$$

with coefficients:

$$\begin{aligned} a_\perp &= -\frac{3}{2}\Delta_h(M_1 + \mathrm{i}M_2) - (x'_d + \mathrm{i}y'_d)M_3, \\ b_\perp &= 3\Delta_h(x'_d M_1 + y'_d M_2) + (1 + x'^2_d + y'^2_d - 2\Delta_h^2)M_3. \end{aligned}$$

The (non rational) function $f_\perp(\xi')$ that derives from our computations is

$$f_\perp(\xi') = -\frac{\mu_0}{4\pi}\frac{R^2}{\xi'}\frac{s(\xi')}{\left(-\frac{R^2}{\xi'}p(\xi')\right)^{\frac{5}{2}}}$$

and by squaring both of its sides we get the rational function:

$$f_\perp^2(\xi') = -\frac{\mu_0^2}{16\pi^2 R^6}\frac{\xi'^3 s^2(\xi')}{p^5(\xi')}. \tag{2.6}$$

Link between polynomial $p(\xi')$ and dipole location X_d: from the above study we know that the coefficients of the polynomial $p(\xi')$ (which appears in the denominator of the study at each component) are given by expression:

$$p(\xi') = \overline{\xi'}_d \xi'^2 - (1 + |\xi'_d|^2 + (h - h_d)^2)\xi' + \xi'_d.$$

The root ξ'_- of p in $\mathbb{D}$ is linked to ξ'_d, because the coefficients of p contain the information ξ'_d and h_d of the dipole X_d. Our goal now is to estimate ξ'_-. Note that in our study we denote with ξ'_- the location of the actual pole of our rational function and with $\hat{\xi'}_-$ its estimation. To avoid confusion we must clarify that we often call ξ'_- as the theoretical pole.

2.1.3 Combination of raw data and model's rational function on $\mathbb{T}$

Let us denote the rational functions of our model which are given from Equations (2.4), (2.5) and (2.6) as f^2. The function f^2 is defined for the whole complex plane $\mathbb{C}$ with exception its poles.

The third step of our analysis is to observe that for the points $\xi'_j = e^{\mathrm{i}\theta_j}$ at which we have values b_j (that consist of measurements b_{rj}, $b_{\perp j}$ or $b_{\tau j}$, see Section 2.1.1) on our circular path, it holds that

$$f^2(e^{\mathrm{i}\theta_j}) = b_j^2.$$

Continuing the treatment of our signal we observe that the rational functions f^2 of our model can be simplified by dividing with $e^{\mathrm{i}\theta_j} = \xi'_j$ when the data are acquired from B_r and B_τ sensors and by $e^{3\mathrm{i}\theta_j} = \xi'^3_j$ when the data are acquired from $B_\perp$ sensor. Equivalently our raw data have the forms: $\frac{f_r^2(e^{\mathrm{i}\theta_j})}{e^{\mathrm{i}\theta_j}} = \frac{b_{rj}^2}{e^{\mathrm{i}\theta_j}} = F_r(e^{\mathrm{i}\theta_j})$, $\frac{f_\tau^2(e^{\mathrm{i}\theta_j})}{e^{\mathrm{i}\theta_j}} = \frac{b_{\tau j}^2}{e^{\mathrm{i}\theta_j}} = F_\tau(e^{\mathrm{i}\theta_j})$,
and $\frac{f_\perp^2(e^{\mathrm{i}\theta_j})}{e^{3\mathrm{i}\theta_j}} = \frac{b_{\perp j}^2}{e^{3\mathrm{i}\theta_j}} = F_\perp(e^{\mathrm{i}\theta_j})$.
The physical model suggests that our treated data can be represented with rational functions F_r, $F_\perp$ and F_τ which, for simplicity, we denote as $F \in L^2(\mathbb{T})$. A handy reference at this point is that later on, in Chapter 3 we have a section dedicated to the polynomial p analysis (this section is called "Denominator analysis"). In that section we show that polynomial p has no root on $\mathbb{T}$. This is the reason why we can express F_r, $F_\perp$ and F_τ as $F \in L^2(\mathbb{T})$.
It holds that

$$F(e^{\mathrm{i}\theta}) = \underbrace{F^+(e^{\mathrm{i}\theta})}_{\text{poles outside } \mathbb{D}} \oplus \underbrace{F^-(e^{\mathrm{i}\theta})}_{\text{poles inside } \mathbb{D}},$$

where F^+ is an analytic function inside the unit disk $\mathbb{D}$ and F^- is an analytic function outside the unit disk $\mathbb{D}$. The part we are interested in studying is the F^- because it is a rational function with poles inside the unit disk $\mathbb{D}$. Note that the poles of F^- are related with the zeroes in $\mathbb{D}$ of the order 5 polynomial p^5 where p has degree less or equal to two.
For the rational function F, the above decomposition corresponds to that of $L^2(\mathbb{T}) = H^2 \oplus H_2^\perp$ in terms of Hardy spaces.

Definition 1 *The Hardy space $H_2^\perp$ consists of all functions $f(z) = \sum_{n<0} a_n z^n$ with $a_n \in \mathbb{C}$ (analytic outside $\mathbb{D}$) such that $\|f\|_2^2 = \sum_{n<0} |a_n|^2 < \infty$ (from Parseval theorem). Analogously, the Hardy space H_2 consists of all functions $f(z) = \sum_{n\geq 0} a_n z^n$ with $a_n \in \mathbb{C}$ (analytic in $\mathbb{D}$) such that $\|f\|_2^2 = \sum_{n\geq 0} |a_n|^2 < \infty$, see [24].*

Based on the available information we can compute an approximate repre-

sentation of F by using Fourier expansion, as in [25]:

$$F(e^{\mathrm{i}\theta}) \approx \sum_{l=0}^{N} c_l e^{\mathrm{i}l\theta} + \underbrace{\sum_{l=-N}^{-1} c_l e^{\mathrm{i}l\theta}}_{\text{stable part}},$$

where $2N+1$ is the total number of the Fourier coefficients c_l defined by the formulas

$$c_l = \frac{1}{2\pi}\int_{-\pi}^{\pi} F(e^{\mathrm{i}\theta})e^{-\mathrm{i}l\theta}d\theta \approx \frac{1}{N}\sum_{j=1}^{N} F(e^{\mathrm{i}\theta_j})e^{-\frac{\mathrm{i}l\theta_j}{N}}.$$

In our analysis $l \in \mathbb{Z}$, $N = 360$ (is the number of measurement points and it is an even number for us). In our study we use the Discrete Fourier Transform (DFT) to compute Fourier coefficients. The Fourier coefficients are split into a stable and unstable part. The important information now is contained in the stable part of the Fourier expansion which is the orthogonal projection F^- of F on $H_2^{\perp}$. This is a representation of F^- and has poles inside the unit disk $\mathbb{D}$. We do actually get its approximation F_N^-:

$$F_N^-(e^{\mathrm{i}\theta}) = \sum_{l=-N}^{-1} c_l e^{\mathrm{i}l\theta}\,.$$

The last step of our measurement treatment is that when the coefficients c_l of the stable part of the Fourier expansion F_N^- are computed, we normalize them by using the following formula for all $l = -1, .., -N$:

$$v_l = \frac{c_l}{\left(\sum_{l=-N}^{-1} |c_l|^2\right)^{\frac{1}{2}}}.$$

We do that because the computed c_l values are small (with modulus smaller than 10^{-12}). The normalization provides us with values v_l that can be expressed as a vector $\mathbf{v} = [v_{-1}, ..., v_{-N}] \in \mathbb{R}^n$. Observe that we can define a function W^- which is computed from the normalized F_N^- as:

$$W^-(e^{\mathrm{i}\theta}) = \sum_{l=-N}^{-1} v_l e^{\mathrm{i}l\theta} = \frac{F_N^-(e^{\mathrm{i}\theta})}{\|F_N^-\|_2}\,. \tag{2.7}$$

2.2 Grid method

As we mentioned before, Grid method and PHC method are used to initialize properly RARL2 which provides us with a pole estimation (denoted as $\hat{\xi'}_-$) inside the unit disk $\mathbb{D}$. However in our study we want to know the value

of the actual pole ξ'_-. We compute ξ'_- by solving a direct problem with the use of the exact location $\mathbf{X}_d$ of the dipole. For the experiments with simulated data, we compute both ξ'_- and $\hat{\xi}'_-$. The reason why we need to know the exact pole location ξ'_- is in order to evaluate the accuracy of the methods we develop, however for the computation of the pole estimate $\hat{\xi}'_-$ we obviously use only the measured signal and not the location of the dipole which creates it.
The first method of pole estimation consists of a naive discrete grid search (we essentially minimize the cost function on a finite set of points).

- The first step is to define a list of points in the disk $\mathbb{D}$ namely α_g with $g = 1, ..., 36000$, which forms our grid where the cost function will be evaluated, see Figure 2.3. We do that because we are interested to find a pole estimation $\hat{\xi}'_{\text{est}}$ inside the unit disk $\mathbb{D}$.

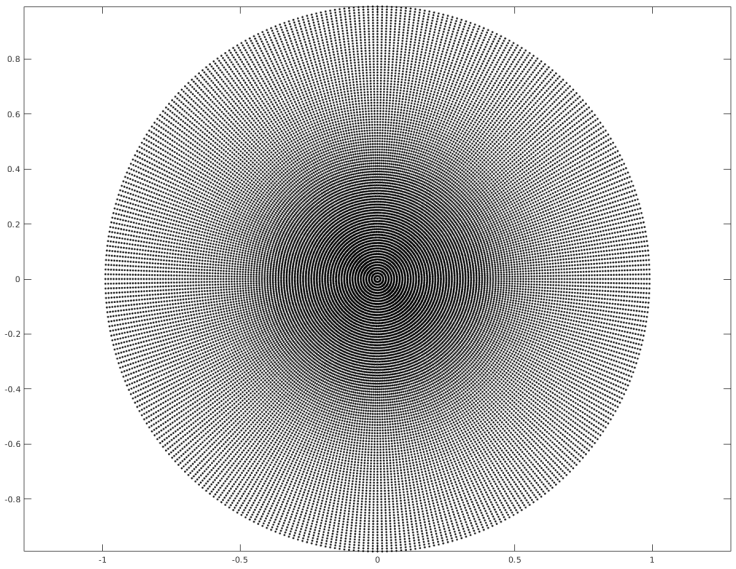

Figure 2.3: This picture illustrates the points α_g of our grid where we evaluate the cost function (black dots). The grid is formed from 100 equidistant points on the radius R taken every 1°.

- The next step is to define our cost function. The idea is to look for the best polynomial $Q(\xi' - \alpha_g)$ of degree less than or equal to four, that minimizes the criterion

$$\left\| \frac{Q(\xi' - \alpha_g)}{(\xi' - \alpha_g)^5} - W^-(\xi') \right\|_2 . \tag{2.8}$$

  For this criterion we use the Euclidean norm.

Note that we use polynomial $Q(\xi' - \alpha_g)$ instead having just an approximation with a polynomial $Q(\xi')$. We do that in order to work with a family of rational functions namely $\dfrac{(\xi' - \alpha_g)^k}{(\xi' - \alpha_g)^5}$ with $k = 0, 1, 2, 3, 4$. For this family we can expand our polynomial expressions as follows:

$$\frac{Q(\xi' - \alpha_g)}{(\xi' - \alpha_g)^5} = \frac{q_0 + q_1(\xi' - \alpha_g) + q_2(\xi' - \alpha_g)^2 + ... + q_4(\xi' - \alpha_g)^4}{(\xi' - \alpha_g)^5}$$
$$= \frac{q_0}{(\xi' - \alpha_g)^5} + \frac{q_1}{(\xi' - \alpha_g)^4} + \frac{q_2}{(\xi' - \alpha_g)^3} + \frac{q_3}{(\xi' - \alpha_g)^2} + \frac{q_4}{(\xi' - \alpha_g)}.$$

Since ξ'_j, α_g and $W^-(\xi'_j)$ are known quantities we can create the matrix $\mathbf{M}$ with size 360×5 such that:

$$\mathbf{M} = \left[(\xi'_j - \alpha_g)^{-1}, (\xi'_j - \alpha_g)^{-2}, (\xi'_j - \alpha_g)^{-3}, (\xi'_j - \alpha_g)^{-4}, (\xi'_j - \alpha_g)^{-5}\right],$$

$j = 1, \cdots, 360$. We can also create a vector $\mathbf{W}$ of size 360 which has as elements the values $W^-(\xi'_j)$. To compute the coefficients of the polynomial Q, our problem boils down to a search for a solution of the column vector $\mathbf{q} = [q_4, q_3, q_2, q_1, q_0]^T$, with size 5×1, of an overdetermined system

$$\mathbf{M}\,\mathbf{q} = \mathbf{W}\,.$$

Such a solution does not exist in general and we therefore compute the solution to the associated least squares problem of minimizing the discrete criterion:

$$\|\mathbf{M}\,\mathbf{q} - \mathbf{W}\|_2^2\,.$$

This can be computed by using the Moore-Penrose pseudo-inverse [26, Sec. 5.5.4] matrix $\mathbf{M}^+$. In this situation, the pseudo-inverse $\mathbf{M}^+$ of $\mathbf{M}$ is given by the expression

$$\mathbf{M}^+ = (\mathbf{M}^*\mathbf{M})^{-1}\mathbf{M}^*\,,$$

where $\mathbf{M}^*$ is the conjugate transposed matrix of $\mathbf{M}$. The solution to the least squares problem is then given by

$$\hat{\mathbf{q}} = \mathbf{M}^+\mathbf{W}.$$

This estimate $\hat{\mathbf{q}}$ of $\mathbf{q}$ furnishes an approximation of the coefficients of the polynomial $Q(\xi' - \alpha_g)$. We can then compute the Fourier expansion of $Q(\xi' - \alpha_g)/(\xi' - \alpha_g)^5$ depending on α_g and use its results to evaluate our criterion in Expression (2.8).
The α_g point from our grid which returns the minimum value for our Criterion (2.8), is our choice as the estimation $\hat{\xi'}_{\text{est}}$ for the pole location.

By collecting all the computed values of our Criterion (2.8) for each point α_g of our grid, we can plot a 3D surface as illustrated in Figures 2.4 and 2.5. One can see that depending on the data we can produce surfaces with various shapes. These surfaces are plotted by using as (x, y) coordinates the coordinates of the α_g points and as z coordinate the computed value of the Criterion (2.8) with respect to each α_g point.

More precisely in order to produce the results of Figures 2.4 and 2.5 we need to use synthetic data from the $B_\perp$ sensor at height $h = 0.015$ and with distance from the revolution axis equal to $R = 0.15$.

In Figure 2.4 for both pictures we use ideal data (without noise) taken at every 1° (hence N=360) their information for the dipole location and moment are collected in the following table.

Figure 2.4	dipole location	dipole moment
left picture	$[-0.0077, -0.0278, -0.1044]$	$[0.3731, -0.9058, 0.2004] \cdot 10^{-3}$
right picture	$[-0.0592, 0.0566, 0.1129]$	$[0.5069, 0.8495, -0.1457] \cdot 10^{-3}$

In Figure 2.5 in both pictures we use the same dipole. The difference between the pictures in Figure 2.5 comes from the fact that the picture on the left concerns ideal data in contrast to the picture on the right where our data are contaminated with 5% uniform noise on our measurements and our study continues without using any denoising technique. The information for the dipole location and moment is collected in the following table.

Figure 2.5	dipole location	dipole moment
both pictures	$[0.0287, 0.0310, 0.0072]$	$[-0.6816, 0.1428, 0.7175] \cdot 10^{-3}$

During our study we observed a plethora of different surface shapes not just those few we illustrate here. We also observe that the shape of the surface can affect the $\hat{\xi}'_{\text{est}}$ estimation. For instance surfaces with big flat valleys close to their global minimum increase the uncertainty for a good $\hat{\xi}'_{\text{est}}$ estimation because small perturbations at the bottom of the surface can lead to different estimations for the pole location estimation.

For synthetic data with 5% uniform noise and without any denoising treatment, the shape of the surface changes a little bit. This can be observed if one compares the two pictures in Figure 2.5. Observe that for noisy data the global minimum is lifted up which can create bigger uncertainty for cases with flat valleys close to their global minimum.

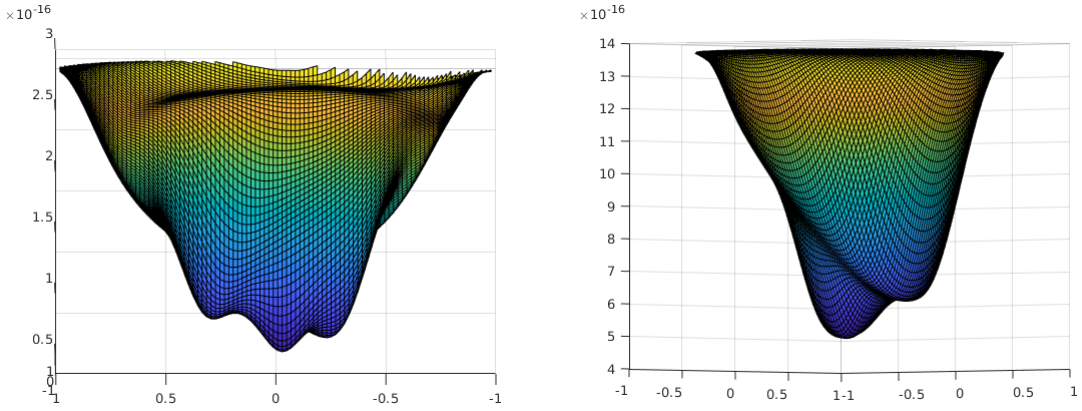

(a) (b)

Figure 2.4: These pictures illustrate two surface plots of our cost function (as given by Expression (2.8)) with different shapes. The picture on the left corresponds to $X_d = [-0.0077, -0.0278, -0.1044]$ and $M_d = [0.3731, -0.9058, 0.2004] \cdot 10^{-3}$. The picture on the right corresponds to $X_d = [-0.0592, 0.0566, 0.1129]$ and $M_d = [0.5069, 0.8495, -0.1457] \cdot 10^{-3}$.

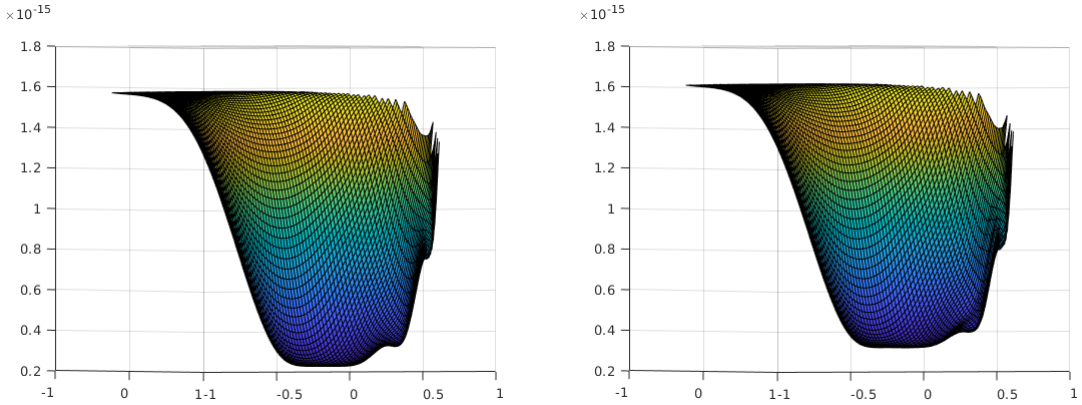

(a) This is a surface plot of our cost function for data without noise.

(b) This is a surface plot of our cost function for the same data with 5% uniform noise.

Figure 2.5: For both picture the dipole is placed at $X_d = [0.0287, 0.0310, 0.0072]$ with $M_d = [-0.6816, 0.1428, 0.7175] \cdot 10^{-3}$.

2.3 PHC method

Another way to find a pole estimation $\hat{\xi}'_{\text{est}}$ inside the unit disk $\mathbb{D}$ is with the use of the Principal Hankel Components approach (PHC) as described

in [27]. This is an order reduction method, which consists in a singular value decomposition of the Hankel matrix of W^- followed by a projection onto the space associated to the most significant P ones, P being the targeted reduced order.

• Once again we are interested by the function W^- introduced in (2.7) which contain the information of the stable part of the Fourier coefficients. We can represent this function with different ways but now we use a representation that comes from control theory and is called state space representation as they did in [27]. With this representation we get

$$W^-(\xi') = \mathbf{c}(\xi'\mathbf{I} - \mathbf{A})^{-1}\mathbf{b},$$

where $\mathbf{A}$ is a square matrix of size $n \times n$ for some $n \in \mathbb{N}$. While $\mathbf{b}$ is a column vector $n \times 1$ and $\mathbf{c}$ is a row vector $1 \times n$.
The advantage of this representation is that the matrix $\mathbf{A}$ may be chosen as a diagonal square matrix hence its elements on the diagonal are its eigenvalues while the others are zero. At the same time from the pole-residue form of a rational function we can associate the poles of a function with the elements of matrix $\mathbf{A}$.

Example: for instance consider the simple case of a rational function with the following pole-residue representation:

$$f(z) = \sum_{k=1}^{n} \frac{c_k}{z - \alpha_k},$$

where $c_k \in \mathbb{C}$, $\alpha_k \in \mathbb{C}$ for $k = 1, \cdots, n$.

$$f(z) = (c_1, c_2, ..., c_n) \begin{pmatrix} \frac{1}{z-\alpha_1} & 0 & \dots & \dots & 0 \\ 0 & \frac{1}{z-\alpha_2} & 0 & \dots & \vdots \\ \vdots & 0 & \ddots & & \vdots \\ \vdots & \vdots & & \ddots & 0 \\ 0 & \dots & \dots & 0 & \frac{1}{z-\alpha_n} \end{pmatrix} \begin{pmatrix} 1 \\ \vdots \\ \vdots \\ \vdots \\ 1 \end{pmatrix}$$

$$f(z) = \mathbf{c}(z\mathbf{I} - \mathbf{A})^{-1}\mathbf{b};$$

where

$$\mathbf{A} = \begin{pmatrix} \alpha_1 & 0 & \dots & \dots & 0 \\ 0 & \alpha_2 & 0 & \dots & \vdots \\ \vdots & 0 & \ddots & & \vdots \\ \vdots & \vdots & & \ddots & 0 \\ 0 & \dots & \dots & 0 & \alpha_n \end{pmatrix}.$$

So our goal now is to create and compute the proper matrix $\mathbf{A}$ because its eigenvalues will give us the poles we are looking for. To do that we use the coefficients v_l of the expression (2.7) of W^- and we create the truncated Hankel matrix $\mathbf{\Phi}_N$, a symmetric matrix with constant entries along the antidiagonals [28, Ch.1], with size $\frac{N}{2} \times \frac{N}{2}$ which is defined as:

$$\mathbf{\Phi}_N = \begin{bmatrix} v_{-1} & v_{-2} & v_{-3} & \dots & v_{-\frac{N}{2}} \\ v_{-2} & v_{-3} & & \dots & \vdots \\ v_{-3} & & \ddots & & \vdots \\ \vdots & \vdots & & \ddots & \\ v_{-\frac{N}{2}} & \dots & \dots & & v_{-N} \end{bmatrix}. \tag{2.9}$$

We follow this approach, due to the fact that the elements of the Hankel matrix coincide with a combination of matrices $\mathbf{A}$, $\mathbf{c}$ and $\mathbf{b}$ as follows:

$$\mathbf{\Phi}_N = \begin{bmatrix} \mathbf{cb} & \mathbf{cAb} & \mathbf{cA^2b} & \dots & \mathbf{cA}^{\frac{N}{2}}\mathbf{b} \\ \mathbf{cAb} & \mathbf{cA^2b} & & \dots & \vdots \\ \mathbf{cA^2b} & & \ddots & & \vdots \\ \vdots & \vdots & & \ddots & \\ \mathbf{cA}^{\frac{N}{2}}\mathbf{b} & \dots & \dots & & \mathbf{cA}^N\mathbf{b} \end{bmatrix},$$

which can be written as:

$$\mathbf{\Phi}_N = \mathcal{O}\,\mathcal{C}\,, \text{ with } \mathcal{O} = \begin{pmatrix} \mathbf{c} \\ \mathbf{cA} \\ \vdots \\ \vdots \\ \mathbf{cA}^{\frac{N}{2}} \end{pmatrix}, \ \mathcal{C} = \left(\mathbf{b}, \mathbf{Ab}, ..., \mathbf{A}^{\frac{N}{2}}\mathbf{b}\right),$$

the last two matrices being known in control theory as observability matrix $\mathcal{O}$ and controlability matrix $\mathcal{C}$, both of size $\frac{N}{2} \times \frac{N}{2}$. In this representation $\mathbf{c}$ has size $1 \times \frac{N}{2}$, $\mathbf{A}$ has size $\frac{N}{2} \times \frac{N}{2}$ and $\mathbf{b}$ has size $\frac{N}{2} \times 1$. Recall that in our study $N = 360$. Based on [27] for $\frac{N}{2} > 50$ the truncated Hankel matrix $\mathbf{\Phi}_N$ yielded good results for all the examples they tried. For this reason we are confident that we have a sufficiently big number of Fourier coefficients compare to the number of poles we want to estimate.

• Our problem now boils down to form the observability matrix $\mathcal{O}$. That happens becuse in [27] they define a process where matrix $\mathbf{A}$ can be computed through proper manipulations of matrix $\mathcal{O}$. To compute the observability matrix $\mathcal{O}$ we use the PHC algorithm as they did in [29]. The idea is

to use singular value decomposition (SVD) and then compute the observability and controlability matrices as follows. First we compute the SVD of $\mathbf{\Phi}_N$:

$$\mathbf{\Phi}_N = \mathbf{U}\mathbf{\Sigma}\mathbf{V}^*,$$

where $\mathbf{\Sigma}$ is a diagonal matrix and $\mathbf{U}$, $\mathbf{V}$ are unitary matrices.

In [30] is explained that the singular values are given in decreasing order, hence the first $P \leq N/2$ singular values will be bigger when compared to the others. From the number of these singular values they define the number of the stable poles. Hence our Hankel matrix can take the form:

$$\mathbf{\Phi}_N = [\mathbf{U}_P \ \ \mathbf{U}_T] \begin{bmatrix} \mathbf{\Sigma}_P & 0 \\ 0 & \mathbf{\Sigma}_T \end{bmatrix} \begin{bmatrix} \mathbf{V}_P^* \\ \mathbf{V}_T^* \end{bmatrix}.$$

Note that U_P is a $N/2 \times P$ matrix, Σ_P is a $P \times P$ square matrix of the P highest singular values and V_P^* is a $P \times N/2$ matrix. Now we can compute a "reduced" observability matrix $\hat{\mathcal{O}}$ of size $N/2 \times P$ as in [29]:

$$\hat{\mathcal{O}} = \mathbf{U}_P \mathbf{\Sigma}_P^{\frac{1}{2}}.$$

Observe that we care to compute the observability matrix only for the first P singular values because we know that they have a link with the stable poles. Using the reduced observability matrix $\hat{\mathcal{O}}$, we can compute the matrix $\hat{\mathbf{A}}$ with size $P \times P$ as they did in [27], with $P = 5$. Let $\hat{\mathcal{O}}_l$ and $\hat{\mathcal{O}}_f$ the matrices of size $(N/2-1) \times P$ formed by deleting the last and first row of $\hat{\mathcal{O}}$, respectively. As a solution to the overdetermined system of equations $\hat{\mathcal{O}}_l \, \hat{\mathbf{A}} = \hat{\mathcal{O}}_f$, $\hat{\mathbf{A}}$ may be computed as the solution to the associated least square problem, and is given by:

$$\hat{\mathbf{A}} = (\hat{\mathcal{O}}_l^* \hat{\mathcal{O}}_l)^{-1} \hat{\mathcal{O}}_l^* \hat{\mathcal{O}}_f \, .$$

• Because with PHC method we compute up to 5 poles in $\mathbb{D}$ (but in our problem we are looking for a single pole of order 5), the last step is to average the solutions of the eigenvalues of the matrix $\hat{\mathbf{A}}$. Figure 2.6 illustrates the behavior of the PHC method and its averaged eigenvalues for ideal and noisy data. Note that in order to produce the pictures in Figure 2.6, we use the same dipole location and moment as for the pictures in Figure 2.5 with the same convention where the left pictures illustrate ideal data and right pictures illustrate noisy data (with 5% uniform noise on the signal).

Figure 2.5	Dipole location	dipole moment
both pictures	$[0.0287, 0.0310, 0.0072]$	$[-0.6816, 0.1428, 0.7175] \cdot 10^{-3}$

The average of the computed eigenvalues of the PHC method provides another estimation $\hat{\xi'}_{\text{est}}$ for the ξ'_- pole location.

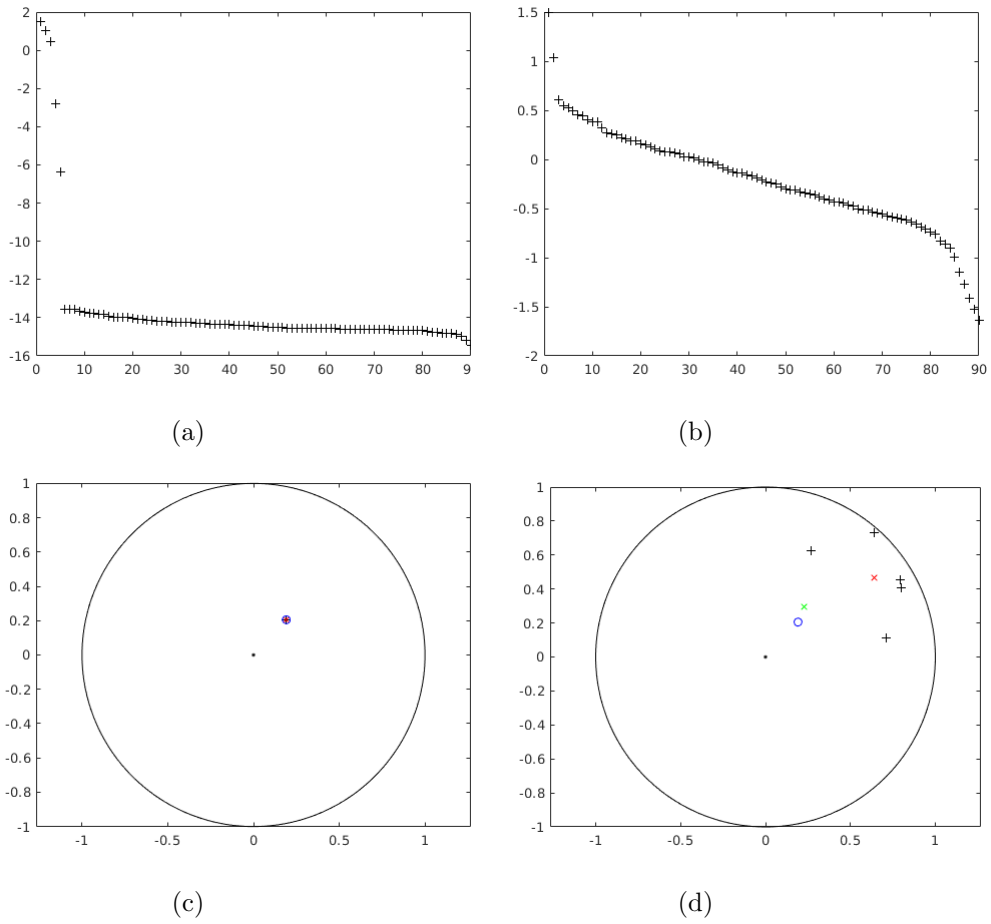

Figure 2.6: Picture on the left illustrate the SVD decomposition (top) and the PHC pole estimation $\hat{\xi'}_{\text{est}}$ (bottom) for synthetic data without noise. Picturse on the right illustrate the same information for synthetic data with 5% uniform noise on the measurements. The $\hat{\xi'}_{\text{est}}$ estimation in the picture below is based on the PHC method illustrated as red ex (it is computed as the mean value of the eigenvalues of matrix $\hat{\mathbf{A}}$ black crosses). The $\hat{\xi'}_{\text{est}}$ estimation from the Grid method illustrated as green ex. The theoretical pole ξ'_{-} illustrated as blue circle and the unit circle center illustrated with a black dot. The black crosses illustrate the singular values. At the top pictures we have all the computed singular values and at the bottom pictures we have the location in $\mathbb{D}$ of the first 5 singular values.

2.4 RARL2 algorithm

A way to compute best quadratic (discrete norm) stable rational approximant to $\dfrac{Q(\xi' - \hat{\xi'}_{\text{est}})}{(\xi' - \hat{\xi'}_{\text{est}})^5}$ with 1 single pole of order 5 is with the use of RARL2[4]

[4] `https://project.inria.fr/rarl2/`

algorithm.
From the PHC and the Grid method we get a $\hat{\xi'}_{\text{est}}$ estimation for the pole location (not necessarily the same see Figure 2.6(d)). We can use $\hat{\xi'}_{\text{est}}$ as initialization of a gradient descent algorithm which is called RARL2. Our final estimation $\hat{\xi'}_{-}$ for the pole location is the RARL2 solution and it is the pole estimation we use in our thesis.
The idea of RARL2 is to parametrize the rational function

$$\frac{Q(\xi' - \alpha_g)}{(\xi' - \alpha_g)^5} = \phi(\lambda_1, ..., \lambda_m)$$

with $m > 0$ parameters $\lambda_1, ..., \lambda_m$. Those parameters can be poles, coefficients or something else that can describe our function. In the present situation, they can be chosen as α_g and the coefficients q_k of Q, $k = 0, \cdots, 4$. The algorithm selects the parameters λ_j so as to minimze the criterion

$$J(\lambda_1, ..., \lambda_m) = \sum_{j=1}^{N} \left| \phi(\lambda_1, ..., \lambda_m)(e^{\mathrm{i}\theta_j}) - W^{-}(e^{\mathrm{i}\theta_j}) \right|^2 ,$$

which is differentiable, namely we can define the gradient of the criterion $J(\lambda_1, ..., \lambda_m)$.
RARL2 is basically an optimization method for which we provide as inputs the values $\mathbf{v} = [v_{-1}, ..., v_{-N}]$ and the initial point $\hat{\xi'}_{\text{est}}$ and it returns to us as a solution to the final estimation for the pole location $\hat{\xi'}_{-}$.

2.5 Comparison of PHC and Grid method

At this point it is useful to decide which method we will adopt to initialize the RARL2 algorithm. As we already discussed, each method has different features. PHC method performs well for a smooth function but it is sensitive to noise. On the other hand the accuracy of the grid method depends on the number of points that form the grid and it could face situations with uncertainty about the global minimum. For this reason, a comparison between PHC method and Grid method is essential. To understand their different behaviors, we have two kinds of errors that we are interested in, the initial-final percentage error (e_{if}) which is defined as

$$e_{if} = \frac{|\hat{\xi'}_{\text{est}} - \hat{\xi'}_{-}|}{|\hat{\xi'}_{-}|} \cdot 100.$$

Initial-final error compares how far our initialization point $\hat{\xi'}_{\text{est}}$ is from the RARL2 final pole estimation solution $\hat{\xi'}_{-}$. The other percentage error we are interested in, is the final-theoretical error (e_{ft}) which is defined as

$$e_{ft} = \frac{|\hat{\xi'}_{-} - \xi'_{-}|}{|\xi'_{-}|} \cdot 100.$$

In this case we compare how good the pole approximation of RARL2 method is compared to the actual pole.
During our study of the e_{ft} error we adopt the color code as illustrated in Figure 2.7.
In Figure 2.7(a) the error bar indicates the level of e_{ft} error. Where, yellow represents error levels with $e_{ft} < 5\%$, black represents error levels with $5\% \leq e_{ft} < 30\%$, red represents error levels with $30\% \leq e_{ft} < 100\%$ and green represents error levels with $100\% \leq e_{ft}$.
In Figures 2.7(b) we illustrate the e_{ft} absolute angle difference (converted in degrees) computed by the expression:

$$|\exp\left(\mathrm{i}(\mathrm{Arg}(\hat{\xi'}_{-}) - \mathrm{Arg}(\xi'_{-}))\right)|.$$

Here we depict with blue the angle differences for values smaller than 5°, with a range of colors that varies from light blue to green and orange for angle differences between 5° to 15° and with yellow for angle differences bigger than 15°.

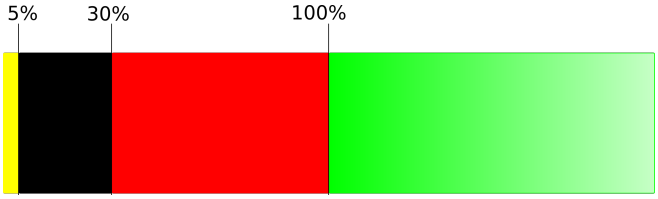

(a)

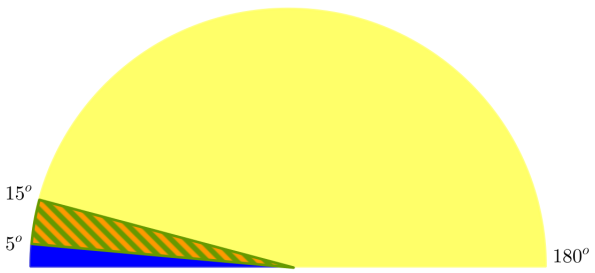

(b)

Figure 2.7: Color code regarding the e_{ft} error level and the absolute angle difference $|\exp\left(\mathrm{i}(\mathrm{Arg}(\hat{\xi'}_{-}) - \mathrm{Arg}(\xi'_{-}))\right)|$.

Study of data without noise: the first set of experiments for the comparison of PHC and grid method consists of 4000 dipoles uniformly spread inside a cylinder. These experiments concern data without noise from a single measurement position and with sensors that are located at the same height. We use the Setup 1.1 as described in Chapter 1.

We gather some of the results of PHC method in Table 2.1.

Table 2.1: PHC method

	B_r	$B_\perp$	B_τ
# of cases with $e_{if} > 0.5\%$	25	27	44
$\max(e_{if})\,\%$	2.8	5.4	4.3
$\max(e_{ft})\,\%$	6.4	4.4	4.6

For the 4000 dipoles without noise PHC method performs well. There are only a few cases for each sensor where the RARL2 does not select as final solution $\hat{\xi'}\_$ the initialization $\hat{\xi'}_{\text{est}}$. All of those cases concern dipoles that are located close to the sensors, because in that case the PHC method could compute eigenvalues that are located outside the unit disk $\mathbb{D}$ and consequently the $\hat{\xi'}_{\text{est}}$ is affected. We also do a comparison between the RARL2 and the theoretical solution. The $\max(e_{ft})$ is 6.4%. This concerns only few cases, either close to the sensors, or close to the revolution axis. The next step of our study is to check how the grid method performs.

We conduct the same simulations but this time by using the grid method see Table 2.2.

Table 2.2: Grid method

	B_r	$B_\perp$	B_τ
# of cases with $e_{if} > 0.5\%$	0	83	1
$\max(e_{if})\,\%$	0.17	1.5	0.6
$\max(e_{ft})\,\%$	29.4	73.4	53.4

The first observation regarding the grid method is that the selection of $\hat{\xi'}_{\text{est}}$ is not far away from the $\hat{\xi'}\_$ RARL2 final estimation. That means that $\hat{\xi'}_{\text{est}}$ is located close to the α_g point of our grid that minimizes our cost function. The second observation is that we do not always select the actual global minimum of our cost function. Note that even with ideal data we can have a dipole with e_{ft} up to 73.4%. This is an issue that we study and it has to do with the evaluation of our cost function at the points α_g of our grid. More precisely for situations with local minimum close to a global minimum or for cases with big flat valleys around the actual pole we can have bad estimations with the grid method. We saw that PHC method can also be affected by the dipoles locations. The difference between the Grid an the PHC method is how they estimate the initial $\hat{\xi'}_{\text{est}}$. On one hand the behavior of the grid method is affected directly from the shape of the cost function. That happens because grid method evaluates the cost functions at specific points and nearby local minimums can drastically affect our estimations. On the other hand PHC method is affected from dipole locations that either represent degenerate cases (for instance close to the revolution axis) or they are located close to the sensors.

One unexpected but interesting result is that the tangential B_τ sensor behaves differently compared to the radial B_r sensor. Though we conduct experiments to favor the one sensor against the other we observe that this behavior is inherent to the sensors features. We cannot explain what exactly generates this behavior and for this reason a more persistent investigation must be completed. However our simulations consistently confirm this different behavior and we are confident of the results we present.

In Figures 2.8(a), (c) and (e) one can see the distribution of the error e_{ft} between $\hat{\xi'}_-$ and ξ'_- solution. From those distributions one can observe that each sensor has a different behavior as we discuss before. The distribution of e_{ft} for the B_r radial sensor, decreasing constantly but slow. The distribution of e_{ft} for the $B_\perp$ vertical sensor decreasing faster than B_r but has few extreme cases with e_{ft} bigger than 50% and the distribution of e_{ft} for the B_τ tangential sensor has two peaks, one large for an error close to 0% and one small for an error close to 40%. This 40% error is visualized in Figure 2.8(f) from the collection of the red points close to the revolution axis.

Note that in Figures 2.8(a), (c) and (e): the vertical axis corresponds to the number of the dipoles and the horizontal axis, to the e_{ft} percentage error of RARL2 solution with respect to the theoretical one. Note also that in Figures 2.8(b), (d) and (f): we have illustrations of the 2D information of the dipoles. Here the vertical axis corresponds to the height z_d of a dipole and the horizontal axis correspond to its distance from the revolution axis $|x_d + \mathrm{i}y_d|$. The yellow dots represent cases with $e_{ft} < 5\%$, the black dots represent cases with $5\% \leq e_{ft} < 30\%$ and the red dots represent cases with $30\% \leq e_{ft}$. Note that the pictures at the top concern the B_r sensor and the middle and bottom ones the $B_\perp$ and B_τ sensors respectively.

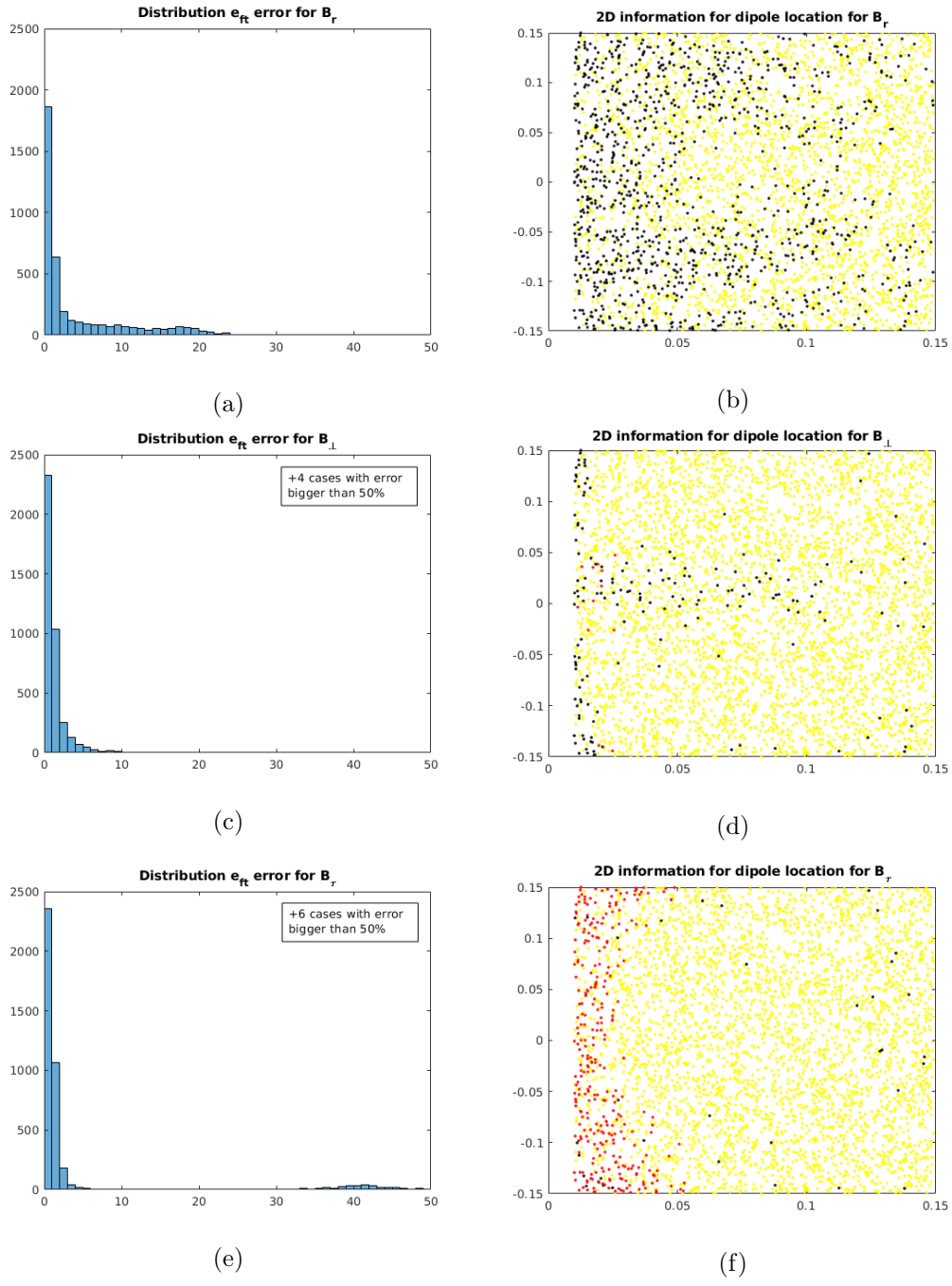

Figure 2.8: Illustrations of the grid method results for ideal data from a single measurement position. All the sensors located at the same height. The pictures on the left illustrate the distribution of e_{ft}. The pictures on the right visualise the dipole heights z_d and their distances $|x_d + \mathrm{i}y_d|$ from the revolution axis.

To ensure that the small peak close to the 40% value in the error distribution of the B_τ sensor in Figure 2.8(e), is also a feature of the sensor and not just an artifact of the way we define our grid α_g with $g = 1, ..., 36000$, we repeat the simulations for a denser grid β_G with $G = 1, ..., 49320$ points. The results regarding the e_{ft} are gathered in Table 2.3.

Table 2.3: Comparison of grids α_g with β_G

Grid		B_r	$B_\perp$	B_τ
α_g	$\max(e_{ft})\,\%$	29.4	73.4	53.4
α_g	# of cases with $e_{ft} > 30\%$	0	12	307
β_G	$\max(e_{ft})\,\%$	31	53.2	57.5
β_G	# of cases with $e_{ft} > 30\%$	2	6	187

Observe that with this approach we manage to decrease the number of dipoles that provide e_{ft} error bigger than 30% from 307 to 187 for the B_τ sensor. Nonetheless the distribution shape remains similar to the one in Figure 2.8(e) but with a smaller peak close to 40%. After reviewing the results derived from the algorithm, we were able to observe there were many cases for the B_τ sensor with errors larger than 30%. We determined that all of these cases, despite how their cost function surfaces look, have a local minimum located close to the global minimum.

From the above analysis we can conclude that for data without noise the PHC method performs better than the grid method. The grid method is also good but it has some features that add uncertainty under specific conditions. Though we can limit this uncertainty with a denser grid, it cannot be completely eliminated. And as a result, will always influence our results.

Study of noisy data: this set of experiments is designed as the previous one, only this time we contaminate the sensors measurements with 5% uniform noise as described in Setup 1.2 in Chapter 1. We compare once again the PHC and the grid method for the 4000 dipoles. The results are gathered in Tables 2.4 and 2.5.

Table 2.4: PHC method with noise

	B_r	$B_\perp$	B_τ
mean $(e_{if})\,\%$	148.8	131.4	147.3
mean $(e_{ft})\,\%$	96.0	81.1	59.2
# of cases with $e_{ft} > 30\%$	2898	2116	2010
# of cases with $e_{ft} > 100\%$	1158	904	836

Table 2.5: Grid method with noise

	B_r	$B_\perp$	B_τ
mean (e_{if}) %	0.04	0.1	0.04
mean (e_{ft}) %	93.0	23.8	54.7
# of cases with $e_{ft} > 30\%$	3093	967	1921
# of cases with $e_{ft} > 100\%$	1168	93	532

One early conclusion from the Table 2.4 is that the PHC method is untrustworthy for data without any denoising treatment. This is an expected result because we violate the conditions where this method holds. The max e_{if} error reaches a value up to 2000%, and its mean error is more than 130%. That means that for contaminated noisy data, PHC method provides essentially an arbitrary point in the unit disk $\mathbb{D}$ as pole estimation $\hat{\xi}'_{\text{est}}$ and it is up to RARL2 to recover a more suitable pole estimation. On the other hand, the grid method provides a point close to a minimum (not necessarily the global one) even for noisy data, since its max e_{if} error does not exceed the 2%. At this point it is useful to clarify that the grid method despite the fact that it uses less iterations of RARL2, is almost two times slower than the PHC method.

In Figures 2.9(a), (c) and (e) one can see the error distribution of the grid method for the e_{ft} error for each sensor. Their vertical axis corresponds to the number of the dipoles and their horizontal axis to the e_{ft} error of RARL2 solution with respect to the theoretical one. In addition, in Figures 2.9(b), (d) and (f) we include the absolute angle difference distribution between RARL2 $\hat{\xi}'_{\_}$ solution and the theoretical one $\xi'_{\_}$. The vertical axis at these pictures corresponds to the number of the dipoles and their horizontal axis to the angle difference expressed in degrees. Pictures at the top correspond to information of sensor B_r and pictures in the middle and bottom correspond to information from sensors $B_\perp$ and B_τ respectively.

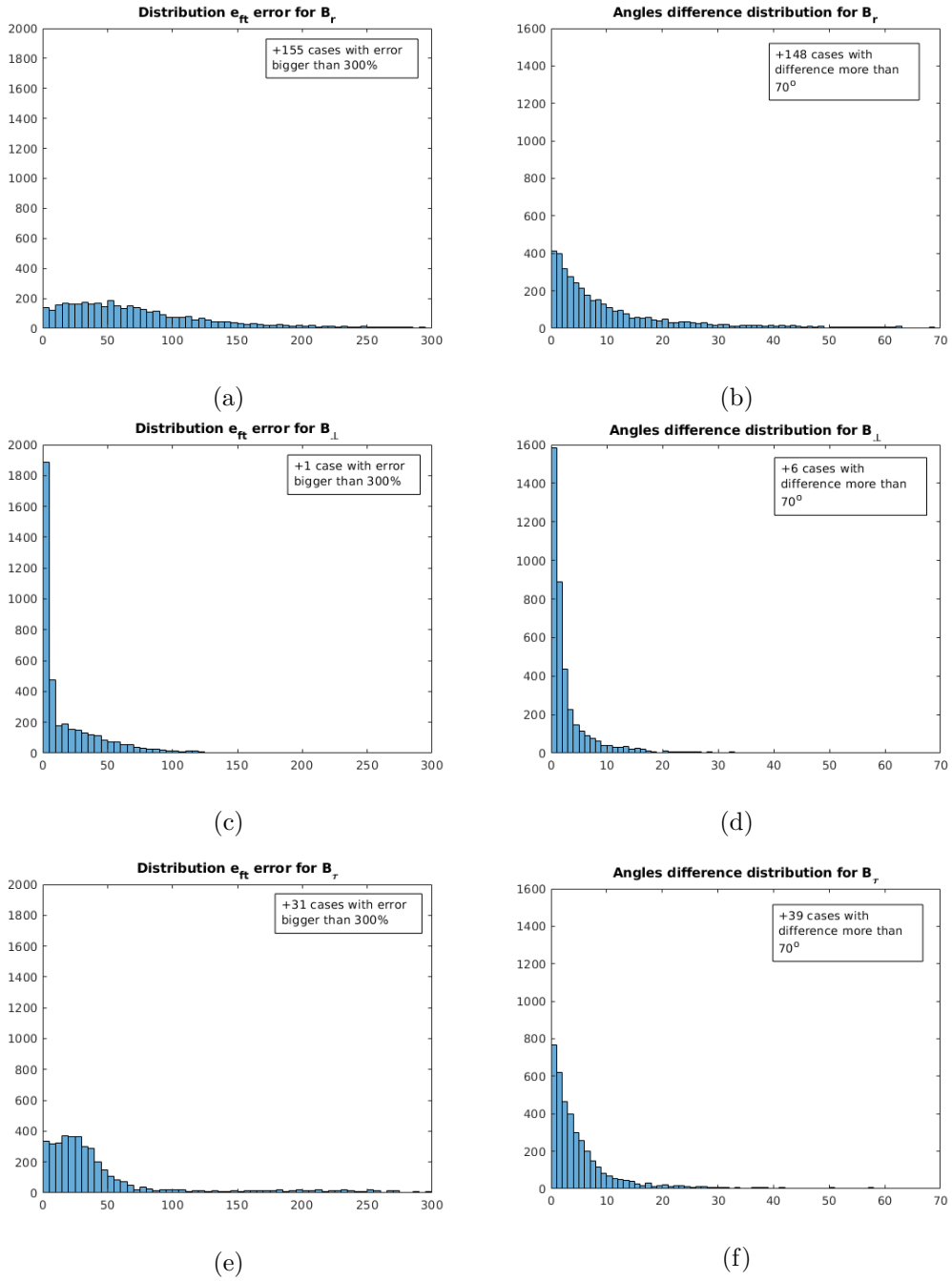

Figure 2.9: Illustrations of the grid method results for noisy data from a single measurement position with sensors at the same height. Pictures on the left show the e_{ft} distribution of each sensor and pictures on the right show the angle difference distribution for each sensor.

In Figure 2.10 we illustrate with different colors the e_{ft} error level information for each one of the dipole locations. As well as the regions where the absolute angle difference between $\hat{\xi'}_-$ and ξ'_- is expected to be high or low with respect to the sensor's distance.
In Figures 2.10(a), (c) and (e) we collect the 2D information of the actual dipoles of our experiment. Their vertical axis corresponds to the dipole height z_d and the horizontal axis corresponds to the dipole distance $|x_d + \mathrm{i}y_d| = \sqrt{x_d^2 + y_d^2}$ from the revolution axis. For the e_{ft} error levels we follow the color code of Figure 2.7(a). Hence the yellow dots represent cases with $e_{ft} < 5\%$, the black dots represent cases where $5\% \leq e_{ft} < 30\%$, the red dots represent cases where $30\% \leq e_{ft} < 100\%$ and the green dots represent cases where $100\% \leq e_{ft}$.
In Figures 2.10(b), (d) and (f) we illustrate the 2D regions information of the absolute angle differences between the $\hat{\xi'}_-$ and ξ'_- with respect to the sensor's distance. Here we follow the color code of Figure 2.7(b).
There is a very interesting observation by comparing the Figures 2.9(a), (c), (e), with the Figures 2.9(b), (d) and (f): The distribution of the e_{ft} error does not have the same shape as the distribution of the absolute angle differences. Based on that we can assume that there exist cases where we can have a larger error for the $\hat{\xi'}_-$ estimation compared to ξ'_- but at the same time a smaller error for their arguments. Roughly speaking the estimated argument of $\hat{\xi'}_-$ is more trustworthy than the modulus $|\hat{\xi'}_-|$, this is more obvious in Figures 2.10(b), (d) and (f), where the blue regions of the angle difference overlap areas with various e_{ft} errors. Note also that each sensor has a different behavior. With strong evidence that the $B_\perp$ sensor performs better than the B_r and the B_τ for the same data.
To conclude this chapter, we studied 2 initialization methods for the pole estimation $\hat{\xi'}_{\text{est}}$, namely the PHC and the grid method and we applied to both of them RARL2 in order to obtain our final result $\hat{\xi'}_-$. We tested PHC and grid method for ideal and noisy data and explored their features for each measurement sensor. Though PHC method is superior with ideal data, its features do not allow it to perform well in situations with noisy data. On the other hand grid method, despite the fact that it is computationally heavier than PHC, has a good performance for both ideal and noisy data. We observe that for noisy data, grid method is better than PHC. In addition when we use grid method for noisy data, we can identify regions where the argument of its solution is well estimated. For this reason in this thesis we use the grid method as initialization for the RARL2. After computing the estimation $\hat{\xi'}_-$ for the pole location, we are in position to study and see how this information is linked with the actual dipole location. Chapters 3 and 4 are focused on that aspect and additional computations provided in Chapter 5.

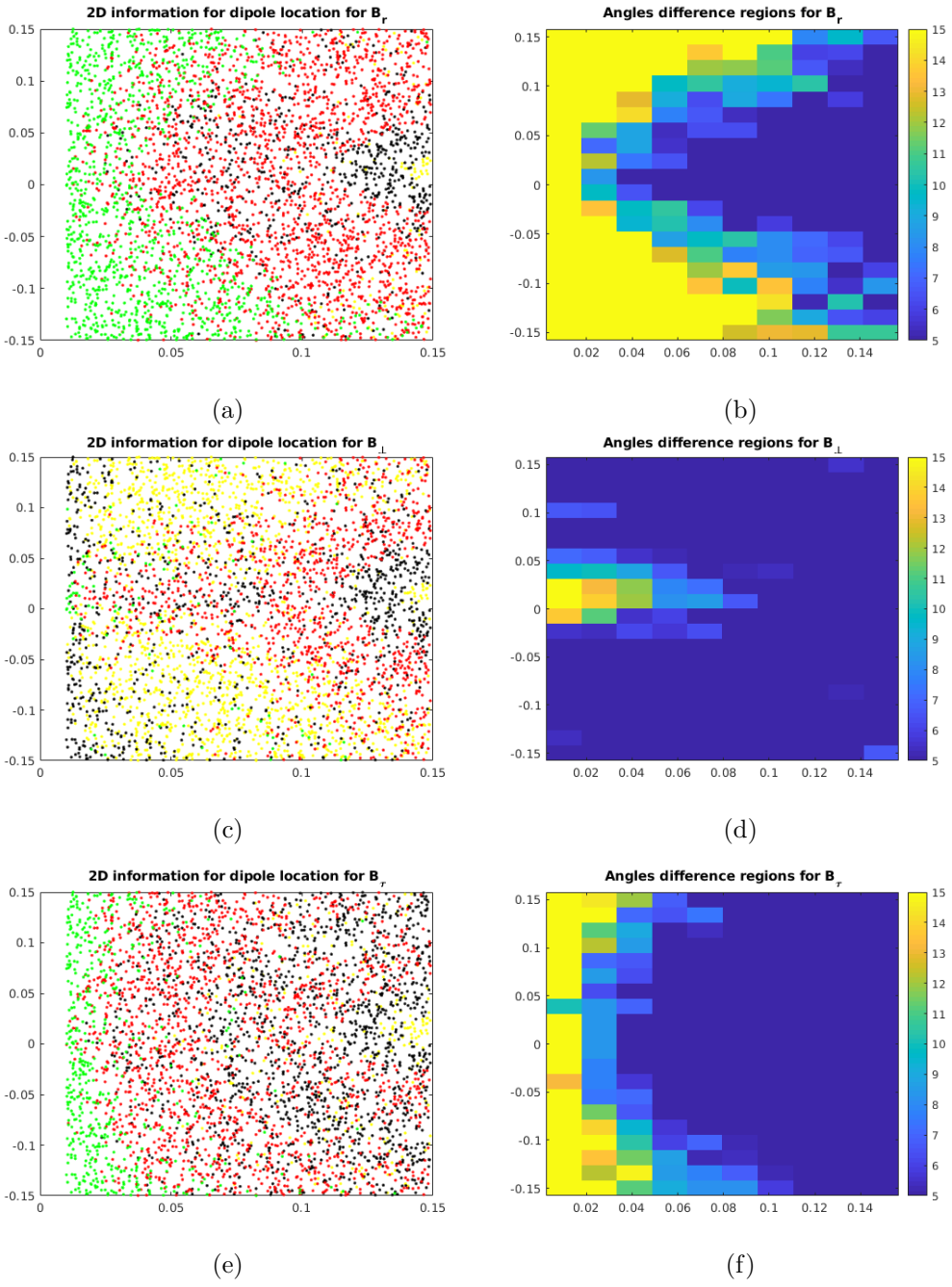

Figure 2.10: Illustrations of the grid method results for noisy data from a single measurement position with sensors located at the same height. Pictures on the left illustrate the 2D information of the actual dipoles with the color code of Figure 2.7(a) for the e_{ft} error. Pictures on the right illustrate the 2D regions information of the absolute angle differences with the color code of Figure 2.7(b).

CHAPTER 3

Dipole location estimation with several methods

In this chapter we are interested in discovering the dipole location $\mathbf{X}_d = (x_d, y_d, z_d) \in \mathbb{R}^3$. In Chapter 2 and article [20, sec. 4] we explained how to estimate the pole $\hat{\xi'}_- \in \mathbb{C}$ of our rational function f^2. We also saw the link between $\hat{\xi'}_-$ and $\mathbf{X}_d$ and we observed the sensors behavior. In order to estimate $\mathbf{X}_d$ we develop several methods each one with its own special features. The goal of this chapter is to understand how these methods work, what their features are and which one is the best candidate to estimate the dipole location $\mathbf{X}_d$. The presentation of these methods in this chapter has the following logic: first we present the planes method, this method provides a general idea for the direction of the dipole location $\mathbf{X}_d$. Then we present three methods namely linear combination, parabola and circles methods respectively. All of these methods take advantage of the information recovered by the planes method and each one of these three methods can estimate a dipole location $\hat{\mathbf{X}}_d$ from a single measurement position. To decide which method is the best candidate to estimate the dipole location $\mathbf{X}_d$ we conducted experiments with synthetic data and we analyzed their features. To start our study, a key observation which comes from Chapter 2 is that the denominator of our main equation, Equation (1.8) namely $|\mathbf{X} - \mathbf{X}_d|^5$, is the same for all components of the magnetic field $\mathbf{B}_{[\mathbf{X}_d, \mathbf{M}_d]}(\mathbf{X})$ and is independent of the moment of the dipole. Together with the fact that the denominator can be linked to the pole of some rational function f^2, with proper manipulation of the denominator we can extract useful information for the dipole location.

3.1 Denominator analysis

In this section we want to study the denominator of our rational functions f^2. We did part of this study in Chapter 2 where we observed that the

denominator $p^5(\xi')$ concerns a polynomial $p(\xi')$ of variable ξ' with degree less or equal to two. Let us consider the measurements provided on one circular path. By using the notations of Chapter 2 on the unit circle $\mathbb{T}$ geometry we get that

$$\xi' = x' + \mathrm{i}y' = \frac{x + \mathrm{i}\, y}{R} = \frac{\xi}{R},\ \ h = \frac{z}{R},\ \ \xi'_d = x'_d + \mathrm{i}\, y'_d = \frac{x_d + \mathrm{i}\, y_d}{R},\ \ h_d = \frac{z_d}{R}.$$

Now, one can observe that the denominator is a positive real number that has the following expression:

$$|\mathbf{X} - \mathbf{X}_d|^5 = \left(|\mathbf{X} - \mathbf{X}_d|^2\right)^{\frac{5}{2}} = \left(|\xi - \xi_d|^2 + (z - z_d)^2\right)^{\frac{5}{2}}.$$

Now we focus our study on the expression $|\mathbf{X} - \mathbf{X}_d|^2$ inside the parenthesis. In this case we can recall from Chapter 2 that the square distance between the sensor and the dipole position is equal to

$$|\mathbf{X} - \mathbf{X}_d|^2 = -\frac{R^2}{\xi'}\left[\overline{\xi'_d}\xi'^2 - \left(1 + |\xi'_d|^2 + (h - h_d)^2\right)\xi' + \xi'_d\right] = -\frac{R^2}{\xi'}p_h(\xi'), \tag{3.1}$$

where $p_h(\xi')$ is another notation for the polynomial $p(\xi')$ with variable ξ', of degree less or equal to two, which concerning measurements at height h. Polynomial $p_h(\xi')$ is given by

$$p_h(\xi') = \overline{\xi'_d}\xi'^2 - \left(1 + |\xi'_d|^2 + (h - h_d)^2\right)\xi' + \xi'_d\,. \tag{3.2}$$

In Chapter 2 we saw that by squaring the measurement data b^2 we can get a rational function f^2 with structure $f^2 = \xi' q(\xi')^2 / p_h(\xi')^5$, where $q(\xi')$ is a polynomial of degree less or equal to four. The poles of function f^2 are the points where the denominator vanishes. That means those points are the roots of polynomial $p_h(\xi')$ in Equation (3.2) which depend only on the dipole position $\mathbf{X}_d$.

Study of $p_h(\xi')$: lets start our study of the $p_h(\xi')$ polynomial with a remark.

Remark 1 *When $\xi'_d = 0$, Equation (3.2) is simplified to*

$$p_h(\xi') = -\left(1 + (h - h_d)^2\right)\xi'.$$

This simplified expression represents degenerated cases that are located on the revolution axis. This expression is equal to 0 only if $\xi' = 0$. Since RARL2 provides us with a pole estimation inside the unit disk $\mathbb{D}$ we expect that it should compute $\hat{\xi}'_- = 0$. From our experiments with ideal data RARL2 indeed computes $\hat{\xi}'_- = 0$ (with error that varies between 10^{-10} to 10^{-16}). Despite the good results of RARL2 in those degenerated cases we are unable

to continue our study as we do in the rest of the chapter, where it is necessary to have $\hat{\xi}'_- \neq 0$. In cases like those we are interested in studying the data from the other two measurement positions. If RARL2 computes $\hat{\xi}'_- = 0$ for all three measurement positions, then we have a strong indication that the dipole $\mathbf{X}_d$ is located at the origin of the coordinate system $\mathbf{X}_d = (0, 0, 0)$.

After that remark we can focus our study on the generic case where $\xi'_d \neq 0$.

Proposition 1 *We claim that, the two complex roots ξ'_- and ξ'_+ of p_h satisfy that $|\xi'_-| \leq |\xi'_d| < 1 < |\xi'_+|$, that $\xi'_\pm$ and ξ'_d share the same complex argument and that, when h varies, $|\xi'_-|$ reaches its maximal value $|\xi'_d|$ once, at $h = h_d$.*

The process of proving this proposition will set the base of our understanding for the linear combination and the geometrical methods.

Proof.

The polynomial $p_h(\xi')$ has complex value coefficients, nonetheless by using the change of variable $\xi' = t\dfrac{\xi'_d}{|\xi'_d|}$ as one can find in [20,21,31], our polynomial can be expressed (up to a multiplicative constant) as a polynomial with real valued coefficients:

$$p_h(\xi') = \xi'_d\, \mathfrak{p}_h(t),$$

where $\mathfrak{p}_h(t)$ is a polynomial of degree 2 in variable t given by

$$\mathfrak{p}_h(t) = t^2 - \frac{1 + |\xi'_d|^2 + (h - h_d)^2}{|\xi'_d|} t + 1. \tag{3.3}$$

At this point we can focus our study on the polynomial $\mathfrak{p}_h(t)$ which have up to two roots denoted as t_- and t_+.

Remark 2 ***Vieta's formulas***

Vieta's formulas give us the relation between the coefficients and the sum and product of the roots. In the general case for a second order polynomial $q(x) = \alpha x^2 + \beta x + \gamma$ with coefficients α, β, γ and roots r_1, r_2, the Vieta's formulas give

$$r_1 + r_2 = -\frac{\beta}{\alpha}, \;\; r_1 r_2 = \frac{\gamma}{\alpha}$$

When applied in our case for $\mathfrak{p}_h(t)$, we get:

$$t_- t_+ = 1, \tag{3.4}$$

$$t_- + t_+ = \frac{1 + |\xi'_d|^2 + (h - h_d)^2}{|\xi'_d|} \tag{3.5}$$

Note that from Equation (3.4) we can compute t_+ from t_- by taking $t_+ = \dfrac{1}{t_-}$.

Definition 2 *We use the notation convention that $t_- \leq t_+$, and with the use of Equations* (3.4) *and* (3.5) *we deduce the information that $0 < t_- \leq 1 \leq t_+$.*

Lemma 1 *The polynomial $\mathfrak{p}_h(t)$ has real valued roots.*

This lemma can be proved by computing the discriminant of $\mathfrak{p}_h(t)$:

$$\begin{aligned}\Delta &= \left(-\frac{1+|\xi'_d|^2+(h-h_d)^2}{|\xi'_d|}\right)^2 - 4 \\ &= \frac{\left(1+|\xi'_d|^2+(h-h_d)^2\right)^2 - (2|\xi'_d|)^2}{|\xi'_d|^2} \\ &= \frac{\left((|\xi'_d|+1)^2+(h-h_d)^2\right)\left((|\xi'_d|-1)^2+(h-h_d)^2\right)}{|\xi'_d|^2} > 0.\end{aligned}$$

The discriminant is strictly positive because $|\xi'_d| < 1$ as we saw in Chapter 2 and the above formula involves only additions, multiplications and divisions of positive numbers. Hence the polynomial $\mathfrak{p}_h(t)$ has two real valued roots t_- and t_+.

Lemma 2 *The modulus of ξ'_- is equal to t_-.*

This can be proved directly with the use of the change of variable

$$|\xi'_-| = \left|t_- \frac{\xi'_d}{|\xi'_d|}\right| = |t_-| \frac{|\xi'_d|}{|\xi'_d|} = t_-.$$

Lemma 3 *The argument of $\xi'_\pm$ is equal with the argument of ξ'_d:*

$$Arg(\xi'_\pm) = Arg(\xi'_d)$$

This directly follows from the change of variables $\xi'_\pm = t_\pm \dfrac{\xi'_d}{|\xi'_d|}$ and the fact that $t_\pm > 0$ are positive real numbers.

Lemma 4 *The root t_- of $\mathfrak{p}_h(t)$ as a function of h, attains its maximum value at $h = h_d$, moreover $t_- \leq |\xi'_d|$.*

In order to prove this lemma we use Equation (3.5). Let $\rho = h - h_d$, then we can see the above expression as a function

$$\aleph(\rho) = \frac{1+|\xi'_d|^2+\rho^2}{|\xi'_d|},$$

of variable ρ and parameter $|\xi'_d| \neq 0$. The function $\aleph(\rho)$ obviously reaches its unique minimum value when $\rho = 0$ which is equivalent to $h = h_d$. By using this information on function $\aleph(\rho)$ and with the use of Equations (3.4) and (3.5) we get:

$$\aleph(0) \leq \aleph(\rho) \Leftrightarrow |\xi'_d| + \frac{1}{|\xi'_d|} \leq t_- + \frac{1}{t_-}.$$

Now we bring everything on the same side and we simplify it by using that $0 < |\xi'_d| t_- < 1$, with $|\xi'_d| < 1$ from Chapter 2 and $t_- \leq 1$ from Definition 2. Hence we get:

$$(|\xi'_d| - t_-)(|\xi'_d| t_-) + (t_- - |\xi'_d|) \leq 0 \Leftrightarrow (|\xi'_d| - t_-)(|\xi'_d| t_- - 1) \leq 0 \Rightarrow |\xi'_d| - t_- \geq 0$$

which proves that $t_- \leq |\xi'_d|$ for $|\xi'_d| \neq 0$.
Thereby we establish the overall claim of Proposition (1).

■

We have now all the tools to analyze the relations between the polynomials $p_h(\xi')$, $\mathfrak{p}_h(t)$ and the dipole location $\mathbf{X}_d$. To exploit those relations we develop several methods that follow.

3.2 Planes method

We start our study with the information furnished by ξ'_-. Our goal is to constrain the area where the dipole $\mathbf{X}_d$ is located. The planes method as its name indicates, defines a plane for each measurement position. Though the planes method can be applied for one position only, the combination of the information from all three measurement positions restrict even further the area of $\hat{\mathbf{X}}_d$. In this section we study how we compute this method and how it restricts the possible location of $\hat{\mathbf{X}}_d$. Keep in mind that with this method we do not estimate a specific point but a region in space.
The idea of the planes method comes from the information we get from Lemma 3. More specifically Lemma 3 states that $\mathrm{Arg}(\xi'_-) = \mathrm{Arg}(\xi'_d)$, namely the direction of the dipole can be estimated through the $\mathrm{Arg}(\xi'_-)$. This direction can be illustrated as a perpendicular (half) plane with respect to the measurement plane that passes through the revolution axis see Figure 3.1. Note that planes method depends only on the information of $\mathrm{Arg}(\xi'_d)$ and not the modulus $|\xi'_d|$.
By construction, the lunometer has a different height h_i for each sensor. From Equation (3.3) we get that by changing the parameter h for some specific ξ'_d and h_d we must compute a different t_- root for each height. Consequently in the ideal case, we expect that RARL2 algorithm will provide us with a different $\hat{\xi'}_{(i)-}$ for each sensor's measurements but all of which with

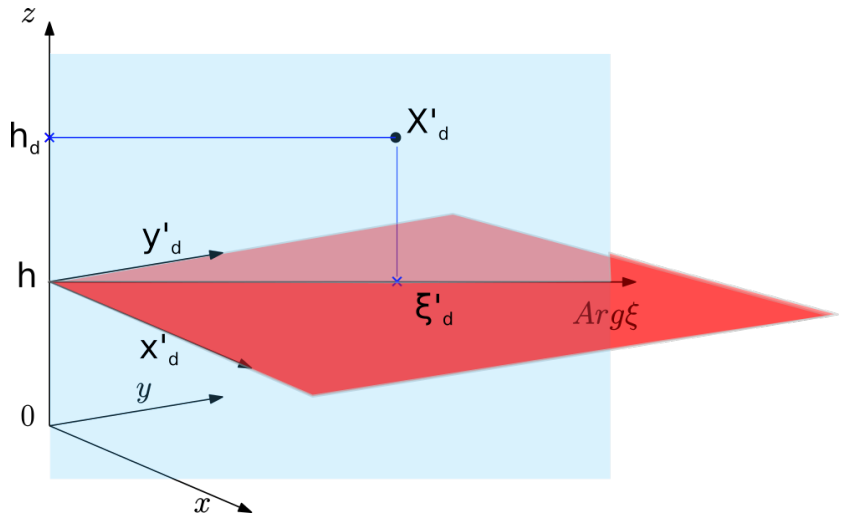

Figure 3.1: In this illustration the measurement plane (also complex plane) of our study is in red. The quantity $\text{Arg}(\xi'_d)$ defines the direction of the perpendicular (half) plane denoted with light blue color where the dipole must belong. Note that the perpendicular plane passes through the revolution axis $0z$.

the same argument. However, due to approximation errors the argument of $\hat{\xi}'_{(i)-}$ estimation is not necessarily the same as the argument of the actual pole $\xi'_{(i)-}$ (see the absolute angle difference in Figure 2.10 in Chapter 2). As a result their corresponding perpendicular planes could differ. Because we recover different perpendicular planes from the $\hat{\xi}'_{(i)-}$ estimations, an averaged plane must be defined in order to continue our study.

3.2.1 Theoretical framework of our averaged plane

Having a list of $\text{Arg}(\hat{\xi}'_{(i)-})$ and due to the fact that we expect $\text{Arg}(\hat{\xi}'_{(i)-}) \approx \text{Arg}(\xi'_d)$, we compute the average angle (in radians), in the range $[-\pi, \pi]$ as illustrated in the Algorithm 1. If the $\text{Arg}(\hat{\xi}'_{(i)-})$ angles range on more than a half of a circle, we specify to Matlab to return **error** which in our study we usually associate it with the value Inf.

Study of cases with range that exceed 90°: in order to decide what to do with cases that $\text{Arg}(\hat{\xi}'_{(i)-})$ angles range on more than 90°, we conduct experiments with synthetic noisy data for 6000 dipoles which are contained in a ball. For these experiments we use the measurements of a single position (more precisely the first position of Setup 1.8). Now we are interested in answering two questions. The first one is whether cases with big range provide bad estimations for the averaged plane (see Figure 3.2(a)) and the

Algorithm 1 Computation of the average angle

Function: AvgAngle
Input: $\xi_1, ..., \xi_N$ a list of non-zero complex numbers
Output: Θ, "average" argument of $\xi_1, ..., \xi_N$

for k=1 to N **do**
  $\theta_k \longleftarrow \text{Arg}(\xi_k)$
end for
RangeAngle $\longleftarrow \max_{k=1,...,N}(\theta_k) - \min_{k=1,...,N}(\theta_k)$
rot $\longleftarrow$ **false** /* rot stands for rotation */
if RangeAngle $> \pi$ **then**
  /* Either the angles are spread on more than a half-plane, */
  /* or they are clustered around $-\pi \equiv \pi\,[2\pi]$ */
  /* We check it by rotating everything by π */
  for k=1 to N **do**
    $\theta_k \longleftarrow \text{NormalizeAngle}(\theta_k + \pi)$
  end for
  rot $\longleftarrow$ **true**
  RangeAngle $\longleftarrow \max_{k=1,...,N}(\theta_k) - \min_{k=1,...,N}(\theta_k)$
  if RangeAngle $> \pi$ **then**
    return error
  end if
end if
$\Theta \longleftarrow \frac{\sum_{k=1}^{N} \theta_k}{N}$
if rot = **true then**
  /* Rotate it back */
  $\Theta \longleftarrow \text{NormalizeAngle}(\Theta + \pi)$
end if
return Θ

Function: NormalizeAngle(θ)
Input: an angle $\theta \in \mathbb{R}$
Output: θ', the unique determination of θ in $[-\pi, \pi)$
$\theta' \longleftarrow \text{Arg}(\exp(\text{i}\,(\theta + \pi)))$
return θ'

second one is whether bad estimation of the averaged plane is an indication of a bad estimation of $|\hat{\xi'}_{(i)-}|$.

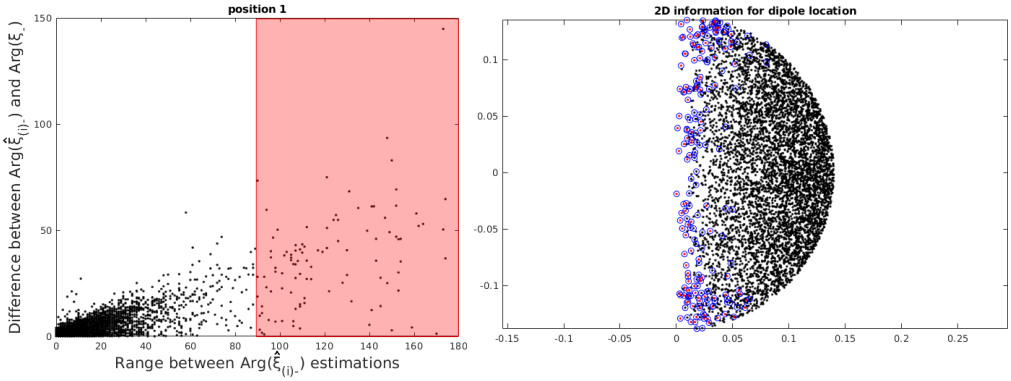

(a) (b)

Figure 3.2: The picture on the left illustrates the range between $\text{Arg}(\hat{\xi'}_{(i)-})$ converted in degrees (horizontal axis) and the range between the actual dipole's angle $\text{Arg}(\xi'_d)$ compared to the averaged angle (vertical axis) also converted in degrees. The red rectangle encloses cases whose $\text{Arg}(\hat{\xi'}_{(i)-})$ range is bigger than 90°. The picture on the right provides the 2D information $|x_d + \mathrm{i}y_d|$ horizontal axis and z_d vertical axis for the dipoles locations black dots. Red dots correspond to dipoles with $\text{Arg}(\hat{\xi'}_{(i)-})$ range more than 90°, and blue circles for similar cases but with range more than 60°. For both pictures we use the first position of Setup 1.8 for noisy data with the use of the grid method.

From our 6000 dipoles analysis we saw that there are 101 cases with $\text{Arg}(\hat{\xi'}_{(i)-})$ ranges that exceed 90° for which an arbitrary averaged angle is computed as one can see in Figure 3.2(a). The mean value for these computed average angles is 36°. There are also 91 cases with $\text{Arg}(\hat{\xi'}_{(i)-})$ ranges between 60° and 90°. For these 91 cases the mean averaged angle is 20°. The behavior of the 91 cases with ranges between 60° and 90° is more predictable. The distribution of the ranges for the 6000 dipoles can be seen in Figure 3.3. We also observe that the dipole locations of all of the cases with $\text{Arg}(\hat{\xi'}_{(i)-})$ ranges that exceed 60° are located around the revolution axis (see Figure 3.2(b)). So, to answer the first question, our experiments confirm that cases with a range bigger than 90° provide unreliable averaged angles.
For the second question we want to check whether a bad estimation of the averaged plane interpreted as bad estimations of $|\hat{\xi'}_{(i)-}|$. For this reason we compute the e_{av} error as follows:

$$e_{av} = \frac{\sum_{i=1}^{S} \left| \frac{|\hat{\xi'}_{(i)-} - \xi'_{(i)-}|}{|\xi'_{(i)-}|} \right|}{S} \cdot 100,$$

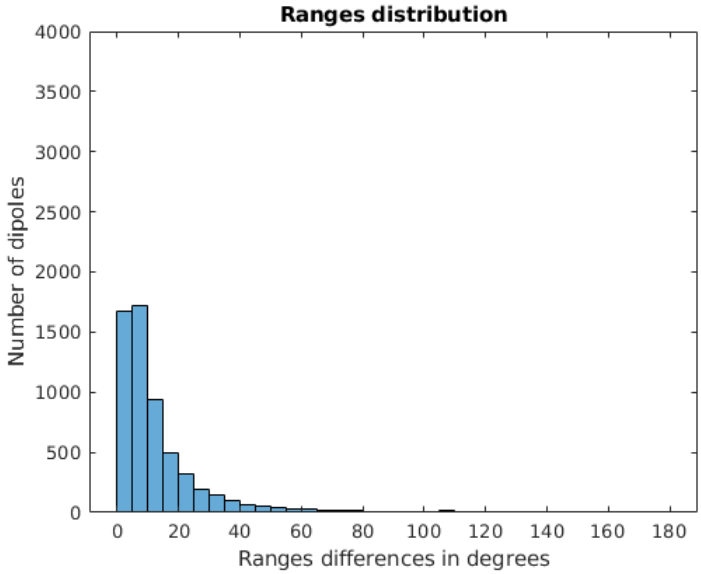

Figure 3.3: This picture illustrates the distribution of the ranges $\text{Arg}(\hat{\xi'}_{(i)-})$ for the 6000 dipoles of our experiments. For these experiments we use noisy data from the first position of Setup 1.8 with the use of the grid method.

where S corresponds to the number of sensors. Which is the averaged error of the $\hat{\xi'}_{(i)-}$ estimates given by all the sensors with respect to the theoretical poles $\xi'_{(i)-}$, for one given experiment. In Figure 3.4 one can see the distribution of the e_{av} error for the cases with $\text{Arg}(\hat{\xi'}_{(i)-})$ ranges (converted in degrees) less than 60°, between 60° to 90° and more than 90° respectively. Observe that the shape of the e_{av} distribution for the cases with $\text{Arg}(\hat{\xi'}_{(i)-})$ ranges less than 60° and between 60° to 90° are similar, in contrast to the cases with ranges more than 90°.
That is an indication that we can exclude cases with $\text{Arg}(\hat{\xi'}_{(i)-})$ ranges more than 90° because they provide unreliable information for both the average angle and the e_{av} error. On the other hand cases with $\text{Arg}(\hat{\xi'}_{(i)-})$ ranges between 60° to 90° have a predictable behavior which is slightly worse but similar when compared to the cases with ranges less than 60°.

Remark 3 ***Data disregarding process***
From our analysis we conclude that with the current lunometer configuration, we can disregard information for cases with ranges that exceed 90°.

We are aware that the current disregarding process rejects all the data of a given position, without concerning if some sensors provide good estimations. For this reason in Chapter 5 we test if a lunometer with more sensors, can find a cluster of sensors with good estimations. Our study provides us with

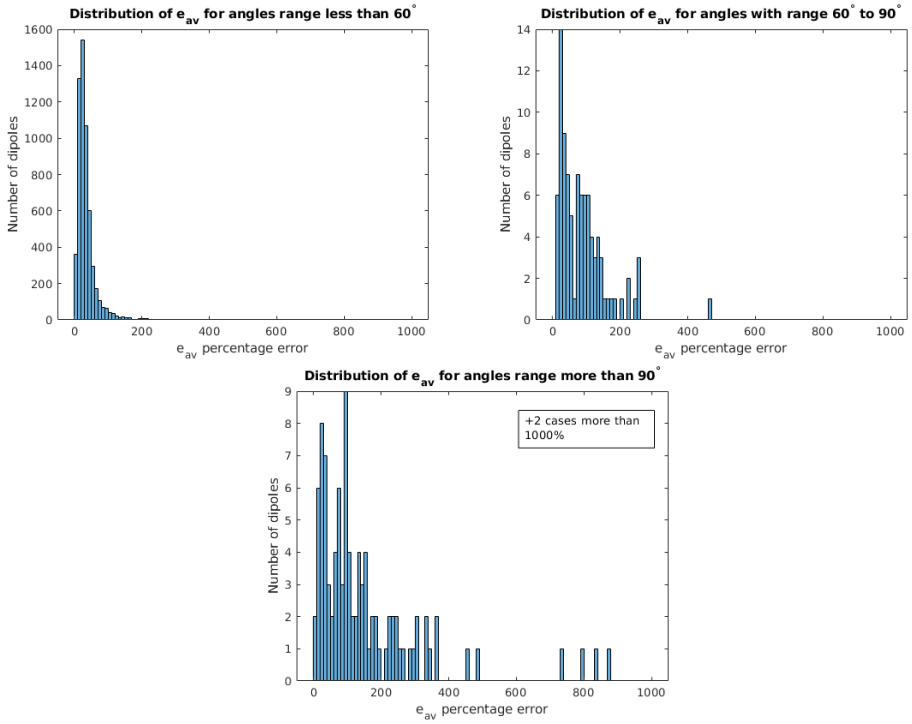

Figure 3.4: These pictures illustrate the e_{av} error for the cases with $\text{Arg}(\hat{\xi'}_{(i)-})$ ranges (converted in degrees) less than 60°, between 60° to 90° and more than 90° respectively. For these experiments we use noisy data from the first position of Setup 1.8 with the use of the grid method.

some evidences that we can indeed define a cluster of sensors with good estimations, however the experiments are at preliminary stages and more simulations must be conducted in order to have a clear answer.
Until now we saw how to compute the average angle/plane for a single measurement position. Hence by combining the information of all three measurement positions we have in total up to three averaged planes as one can see in Figure 3.5.

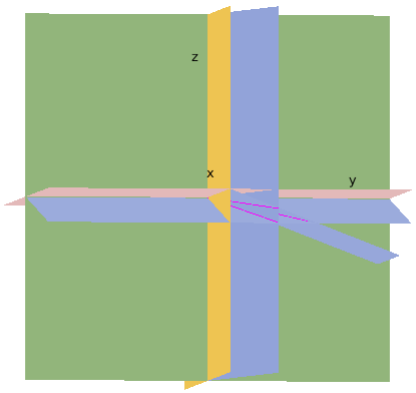

Figure 3.5: This picture illustrates the complex planes of the three measurement positions with red, green and yellow color. The averaged plane for each measurement positions are colored blue. The pairwise intersection of the averaged planes are denoted with (magenta) lines.

Solid angle investigation: this investigation concerns cases where all 3 averaged planes are computed. This investigation conducted to provide an intuition about the combination of the three averaged planes. Its results based on emperical observations, for this reason we do not use it in our numerical experiments study in Chapter 5. In our study the intersection of any pair of averaged planes defines a line in the space, hence three lines overall see Figure 3.5. From those lines we can compute the solid angle as part of a corresponding tetrahedron [32, Theorem 1, Lemma 1], [33] with one of its vertices placed at the origin of our coordinate system.
Let's present shortly the notion of solid angle. A solid angle is related to the surface area of a ball. This surface area can be formed from the intersection of the ball with any geometric object (cone, tetrahedron, etc.). In fact any closed curve on the surface of a ball $\mathbb{B}$, can define lines that meet at a vertex (*e.g.* at the center of the ball $\mathbb{B}$) and creates a solid angle. That means that we can define a solid angle for various shapes, with most common shapes under study in literature be the cones, tetrahedrons and cubes, projecting them onto the surface of the ball. In the lecture notes [34] is described as how to compute a solid angle for a cone, a tetrahedron or a polyhedron.

In our study we are interested only for the solid angle of a tetrahedron, which we will describe in a while. Solid angle is measured in steradian (sr) (SI unit). Note that there are 4π steradians in a sphere in comparison to the 2π of the circle radians. Though the surface area of a ball is $4\pi r^2$ and depends on the radius r of the ball, because we measure an angle, we are not influenced from the ball radius, for this reason solid angle will always measure 4π steradians and the surface area of a steradian will be equal to r^2.

Remark 4 *[32, Sec. 1] The solid angle of a tetrahedron with a vertex on the center of a ball $\mathbb{B}$ is the area of the spherical triangle on the ball $\mathbb{B}$. This spherical triangle formed by the intersection points between the tetrahedron and the sphere see Figure 3.6.*

In our case, in order to compute the solid angle defined by the three averaged planes, we need first to compute the dihedral angles between each pair of averaged planes.

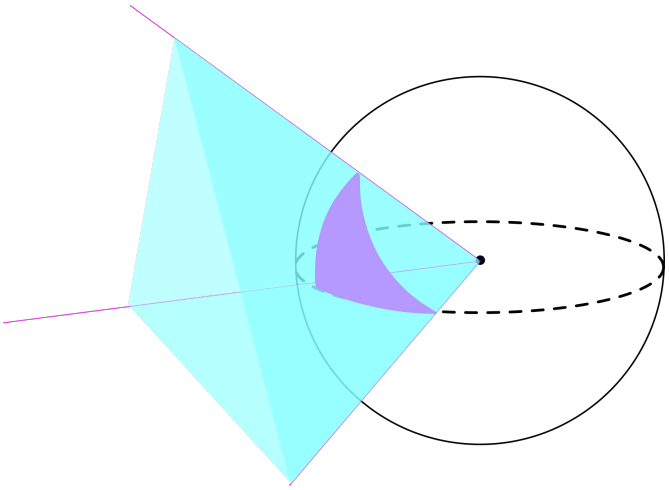

Figure 3.6: For this illustration the magenta lines correspond to the pairwise intersection of the averaged planes. The corresponding spherical triangle on the surface of the unit ball $\mathbb{B}$ (whose surface defines the solid angle) is colored with purple. With light blue color one can see the tetrahedron shape we describe before.

Definition 3 *[35, ch. 8 Sec. 2] The dihedral angle α_c is the angle that formed between two planes with $c = (\{1,2\},\{2,3\},\{3,1\})$ and c denote the possible pairs of our three averaged plains.*

To compute the angle between two planes we need first to know the equation of each plane in the form $A_p x + B_p y + C_p z = D_p$ with p define a plane (in our experiments this is a known information with $p = 1, 2, 3$). Then we define

a normal vector for each plane $n_p = (A_p, B_p, C_p)$ and then the dihedral angle is computed as the angle between the normal vectors n_p as they do in [36, ch.17] with the use of the following formula:

$$\alpha_{12} = \arccos \left| \frac{A_1A_2 + B_1B_2 + C_1C_2}{\sqrt{A_1^2 + B_1^2 + C_1^2}\sqrt{A_2^2 + B_2^2 + C_2^2}} \right|.$$

Similarly we can compute the α_{23} and α_{31}.
Now we can compute the solid angle ϕ also known as spherical excess for the spherical triangles, based on [32, Lemma 1, ch. 8 Sec. 2] as follows:

$$\phi = \alpha_{12} + \alpha_{23} + \alpha_{31} - \pi.$$

The idea of the spherical excess is that the sum of the angles of a spherical triangle will always be bigger or equal to π. This is based on a property of the sum of the angles of a spherical triangle which states that, their sum is greater than 180° and less than 540° [35, sec. 2]. For this reason the solid angle ϕ of our spherical triangle varies between $(0, 2\pi)$. This can be translated as, smaller solid angles provide us with more restricted regions where the dipole $\hat{\mathbf{X}}_d$ should be located. For this reason we want a solid angle ϕ as small as possible. In our study we use the solid angle ϕ as an empirical indicator for the confidence we should have in our estimations. During those first experimentations we adopt an empirical threshold of $3.04 \cdot 10^{-4}$ *sr* which is an approximation of 1 square degree. Square degree is not an SI unit, however it provides an illustration to measure parts of a sphere, in the same way degrees measure parts of a circle. One steradian is equal to $(180/\pi)^2$ square degrees so we can convert steradians to square degrees and the opposite. Note that because this threshold is empirical and based on a personal selection which narrows the solid angle to a square degree, we have used it only to identify cases which deserve extra attention.

3.2.2 Test of planes method, simulations with synthetic data

Remark 5 *An important remark regarding the simulations with synthetic data that follows is that they concern ideal data (data without noise). That happens because the goal of Chapter 3 is to compare the linear combination, parabola and circles method that follows under ideal conditions. However it was important for us to illustrate the behavior of the planes method for noisy data. That was the reason why we decide to study until now the planes method with noisy data from the first measurement position of Setup 1.8.*

From now on we test the planes method by conducting experiments with ideal synthetic data concerning 6000 dipoles inside a ball as described in Setups 1.6 and 1.7 of Chapter 1.

Study of data without noise for the current lunometer configuration: the first experiment we conduct concerns cases with the current lunometer configuration and without noise as described in Chapter 1. For this setup of experiments we conduct measurements for all three measurement positions (Setup 1.6), hence it is a complete set of data. Note that because the planes method does not compute a precise estimation for the dipole $\mathbf{X}_d$, there is no direct way to compare the planes method with the methods we develop later on.
The general results of our experiment are the following:

Experiment	$\text{Arg}(\hat{\xi'}_{(i)-})$ range more than 90°	Average solid angle	Maximum value of solid angle
Setup 1.6	1	$1.36 \cdot 10^{-4}$	0.02

One first observation is that there is only one case with $\text{Arg}(\hat{\xi'}_{(i)-})$ range more than 90°, which is estimated at the first measurement position. We also observe that the maximum solid angle of our experiments is equal to 0.02 *sr* or approximately 65 square degrees which covers 0.15% of the unit sphere surface (a sphere has approximately 41264 square degrees). That means that we have good results for every experiment (which is expected since we deal with ideal data). We face in total 485 cases with solid angle bigger than our $3.04 \cdot 10^{-4}$ threshold, which corresponds to 8.1% of our cases. This is a good indication for the robustness of our method, it tells us basically that with ideal data we can have high confidence for the dipole direction to almost 91% of our averaged planes estimations.

Study of data without noise for multiple sensors: to see how this method behaves with more sensors, we use the Setup 1.7. We conduct the data acquisition process with 11 sensors, as described in Chapter 1.
The general results are the following:

Experiment	$\text{Arg}(\hat{\xi'}_{(i)-})$ range more than 90°	Average solid angle	Maximum value of solid angle
Setup 1.7	3	$7.7 \cdot 10^{-5}$	0.071

In this set of experiments we face 3 cases where $\text{Arg}(\hat{\xi'}_{(i)-})$ range more than 90°. From our investigation we observe that there is 1 case for each measurement position, hence there are 3 cases in total where we do not compute a solid angle. We observe also that the average value of the solid angle for the remaining cases is smaller than our $3.04 \cdot 10^{-4}$ threshold, with

only 263 cases that exceed it. The maximum value for the solid angle in our experiments is 0.071 or 233 square degrees which covers 0.5% of unit sphere surface. In conclusion, the experiments show that more sensors estimate better the dipole direction.
As an extra confirmation of our theory that the solid angle contains the dipole location X_d we select 100 random cases from both of the above experiments and we test if the dipole is actually located between the averaged planes. Indeed for all of the selected cases the dipole was located inside the tetrahedron formed by our averaged planes.

3.3 Linear combination method

We continue our study with the linear combination method. The idea of this method is to manipulate properly the information from Expression (3.5) and solve a linear system. For this reason we introduce the notation λ_h:

$$\lambda_h := \frac{1 + |\xi_d'|^2 + (h - h_d)^2}{|\xi_d'|} = t_+ + t_-. \tag{3.6}$$

Note that λ_h depends only on t_- and t_+, hence we can estimate it from the available data and we will consider it as a known quantity. Now, from Expression (3.6) for $S \geq 3$ we get:

$$\begin{aligned}
\lambda_{h_1}|\xi_d'| &= 1 + |\xi_d'|^2 + (h_1 - h_d)^2, \\
\lambda_{h_2}|\xi_d'| &= 1 + |\xi_d'|^2 + (h_2 - h_d)^2, \\
&\vdots \\
\lambda_{h_S}|\xi_d'| &= 1 + |\xi_d'|^2 + (h_S - h_d)^2.
\end{aligned}$$

Those equations concern data at heights h_i, $i = 1, ..., S$ with unknowns $|\xi_d'|$, h_d. To simplify the system we subtract from the first equation the other $S - 1$ equations and we get:

$$\begin{cases}
(\lambda_{h_1} - \lambda_{h_2})|\xi_d'| = (h_1 - h_d)^2 - (h_2 - h_d)^2, \\
(\lambda_{h_1} - \lambda_{h_3})|\xi_d'| = (h_1 - h_d)^2 - (h_3 - h_d)^2, \\
\qquad\qquad\vdots \\
(\lambda_{h_1} - \lambda_{h_S})|\xi_d'| = (h_1 - h_d)^2 - (h_S - h_d)^2.
\end{cases}$$

By expanding the squares on the right side of the system we end up with

$$\begin{cases}
(\lambda_{h_1} - \lambda_{h_2})|\xi_d'| + 2(h_1 - h_2)h_d = h_1^2 - h_2^2, \\
(\lambda_{h_1} - \lambda_{h_3})|\xi_d'| + 2(h_1 - h_3)h_d = h_1^2 - h_3^2, \\
\qquad\qquad\vdots \\
(\lambda_{h_1} - \lambda_{h_S})|\xi_d'| + 2(h_1 - h_S)h_d = h_1^2 - h_S^2,
\end{cases}$$

which we can express in a matrix form as $A\mathrm{x} = B$ with:

$$A = \begin{bmatrix} \lambda_{h_1} - \lambda_{h_2} & 2(h_1 - h_2) \\ \lambda_{h_1} - \lambda_{h_3} & 2(h_1 - h_3) \\ \vdots & \vdots \\ \lambda_{h_1} - \lambda_{h_S} & 2(h_1 - h_S) \end{bmatrix}, \ \mathrm{x} = \begin{bmatrix} |\xi'_d| \\ h_d \end{bmatrix} \text{ and } B = \begin{bmatrix} h_1^2 - h_2^2 \\ h_1^2 - h_3^2 \\ \vdots \\ h_1^2 - h_S^2 \end{bmatrix}.$$

For $S \geq 4$, the above linear system of $S-1$ equations is overdetermined. Overdetermined systems usually do not have exact solutions [26, Sec. 5.3] but we can find a solution of x denoted as $\hat{\mathrm{x}}$ by solving the least squares problem $\hat{\mathrm{x}} = \mathrm{Argmin}_{\mathrm{x}\in\mathbb{R}^2}|B - A\mathrm{x}|^2$, where $|\cdot|$ is the Euclidean norm. This can be done, *e.g.*, by using the Moore-Penrose pseudo-inverse [37] matrix A^+. The A^+ of A is given by the expression $A^+ = (A^T A)^{-1} A^T$ where A^T is the transposed matrix of A. The solution to the least squares problem is then given by $\hat{\mathrm{x}} = A^+ B$.

Special case with $S = 3$: note that in the particular case when $S = 3$, our system $A\mathrm{x} = B$ has two equations with two unknowns (hence it is not an overdetermined system anymore). In that case matrix A is a square 2×2 matrix.

- If its determinant $\mathrm{Det}A \neq 0$, then A is an invertible matrix and we can compute its unique solution $\mathrm{x} = A^{-1}B$, where A^{-1} is the inverse matrix of A.

- If its determinant $\mathrm{Det}A = 0$ then the equations of the system

$$\begin{cases} (\lambda_{h_1} - \lambda_{h_2})|\xi'_d| + 2(h_1 - h_2)h_d = h_1^2 - h_2^2, \\ (\lambda_{h_1} - \lambda_{h_3})|\xi'_d| + 2(h_1 - h_3)h_d = h_1^2 - h_3^2, \end{cases}$$

  are not independent and we have infinitely many solutions or no solution at all.

  Let's study the value of $\mathrm{Det}A$. For $S = 3$ we know that

$$A = \begin{bmatrix} \lambda_{h_1} - \lambda_{h_2} & 2(h_1 - h_2) \\ \lambda_{h_1} - \lambda_{h_3} & 2(h_1 - h_3) \end{bmatrix},$$

  and its determinant is

$$\mathrm{Det}A = 2\left[(\lambda_{h_1} - \lambda_{h_2})(h_1 - h_3) - (\lambda_{h_1} - \lambda_{h_3})(h_1 - h_2)\right].$$

  For $i \neq j$, Equation (3.6) gives that

$$\lambda_{h_i} - \lambda_{h_j} = \frac{1}{|\xi'_d|}(h_i - h_j)(h_i + h_j - 2h_d).$$

Which for our problem provides $\mathrm{Det}A \neq 0$ because we study general cases with $|\xi'_d| \neq 0$ and $h_i \neq h_j$.

When $h_i = h_j$ we have $\lambda_{h_i} = \lambda_{h_j}$. Consequently for the square matrix A we get $\mathrm{Det}A = 0$ when $h_1 = h_2$ or $h_2 = h_3$ or $h_1 = h_3$. However we must emphasize that a situation like that is impossible with the current lunometer configuration which enforce that $h_i \neq h_j$.

3.3.1 Test of linear combination method, simulations with synthetic data

The theoretical framework of this method is the following: we know that the sensors take measurements at known heights h_i. For each sensor we can compute the λ_{h_i} coefficient through the pole estimations $\xi'_{(i)-}$ as follows:

$$\lambda_{h_i} = |\xi'_{(i)-}| + \frac{1}{|\xi'_{(i)-}|}.$$

To illustrate the behavior of the linear combination method we conducted simulations with ideal synthetic data. We use the Setups 1.3 and 1.4 of the experiments without noise as described in Chapter 1. Both of them consist of 6000 dipole experiments that spread on cylinder surfaces around the revolution axis and for measurements taken at one position. We denote with $\hat{\mathbf{X}}_d = (\xi_d, z_d)$ the 3D estimation from the dipole location. In this experiment, $\hat{\mathbf{X}}_d$ is computed from the information of a single measurement position.

Study of data without noise for the current lunometer configuration: for these experiments we use the Setup 1.3 for a single measurement position as described in Chapter 1.
The result of the linear combination method is an estimation $\hat{\mathbf{X}}_d$ for the dipole location $\mathbf{X}_d$. To analyze our data we compute the percentage error between the estimated and the actual dipole e_{lin} normalized by the radius R of our sensors distance from the revolution axis as follows

$$e_{lin} = \frac{|\hat{\mathbf{X}}_d - \mathbf{X}_d|}{R} \cdot 100.$$

For the current lunometer configuration (special case when $S = 3$) (and with $|\xi'_d| \neq 0$), $Ax = B$ linear system boils down to a system of two equations with two unknowns. That means that RARL2 should provide us with different $\hat{\xi'}_{(i)-}$ pole estimations at each height, this claim is based on the theoretical root $\xi'_{(i)-}$ from Equation (3.3) for cases with same $(|\xi'_d|, h_d)$ and different h. However RARL2 due to approximation and numerical errors provide us with some cases where the $\hat{\xi'}_{(i)-}$ approximations are equal. As a result our computations for the λ_{h_i} coefficients are contaminated from these bad

approximations. This affect our Matlab computations for the e_{lin} dipole error and we get as a result Inf or NaN. We observe that these cases (which correspond to less than 1% of our experiments) are exactly the same cases that provide us with an Inf value for their condition number. We can see where they are located in Figure 3.7(a).

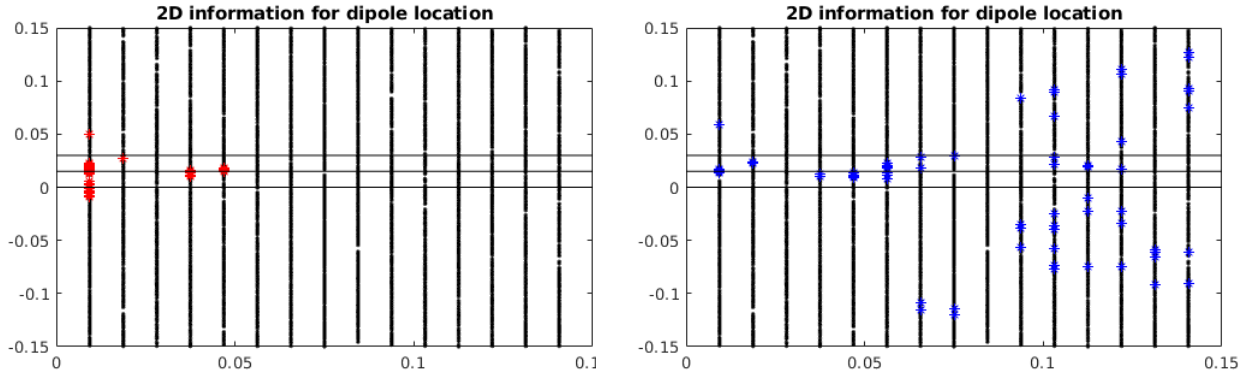

(a) (b)

Figure 3.7: In both pictures the vertical axis shows the information z_d and the horizontal axis the information $|\xi_d|$ for the 6000 generated dipole locations (black dots). The black horizontal lines correspond to the heights of the sensors. For the picture on the left, the red stars illustrate dipole locations with Inf condition number/excluded cases. For the picture on the right, the blue stars illustrate dipole locations that provide us with e_{lin} error more than 1000%. Both pictures illustrate results of the linear combination method.

We computed the condition number in order to check the sensitivity of our matrix A. There are 49 cases with infinite condition numbers, the remaining 5951 cases have a mean condition number of $3.14 \cdot 10^{11}$ with a median condition number located at 40. This is an indication of the sensitivity of our linear equation system. The distribution of the logarithm of the condition numbers we compute can be seen in Figure 3.8.
The general results of our analysis are the following:

Experiment	Average e_{lin}	# of excluded cases	# of dipoles with $e_{lin} > 1000\%$	# of dipoles with $e_{lin} > 50\%$
Setup 1.3	$3.75 \cdot 10^{11}$	49	71	2685

Note that the average e_{lin} is: $3.75 \cdot 10^{11}\%$, for the remaining 5951 dipoles after removing the cases with infinite value for their condition number.
Let us discuss in more detail some of the above results. Figure 3.7(a) illustrates the 2D information for the cases with Inf value for their condition number which are also the excluded cases. Figure 3.7(b) is a similar plot but

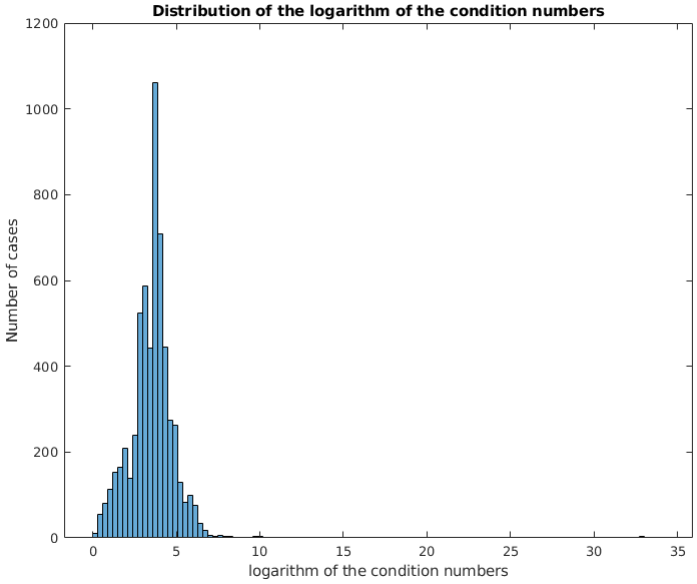

Figure 3.8: This picture illustrates the logarithm of the condition number, for the 5951 remaining cases of the experiment with Setup 1.3 for data without noise (from a single measurement position) and with the current lunometer configuration. These illustrations concern the linear combination method.

concerns the dipoles with e_{lin} bigger than 1000% and Figure 3.9 illustrates the distribution of the e_{lin} error. From the study of the 71 cases with e_{lin} error more than 1000%, we observe that they concern cases where at least two estimated poles are equal.

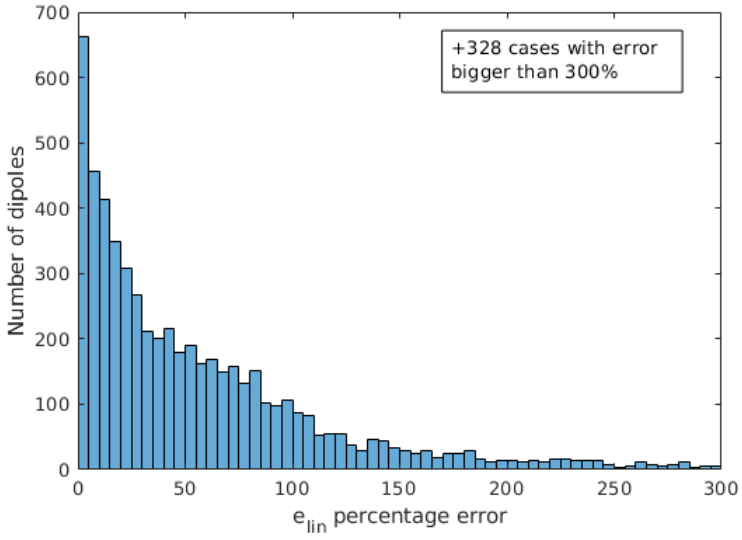

Figure 3.9: This picture illustrates the distribution of the e_{lin} of the linear combination method for errors up to 300%. Its vertical axis corresponds to the number of dipoles and its horizontal axis to the e_{lin} percentage error. These experiments concern the linear combination method with the use of ideal data.

From our analysis we observe that we can have good estimations of the $\xi'_{(i)-}$ but nonetheless the linear combination method will provide us with uncertain estimations of $\hat{\mathbf{X}}_d$. This claim is based on the comparison of the mean e_{ft} error with the e_{lin} error. Note that e_{ft} error is given as we defined it in Chapter 2

$$e_{ft} = \frac{|\hat{\xi}'_- - \xi'_-|}{|\xi'_-|} \cdot 100.$$

Though these two percentage errors have different nature. Their comparison shows that for mean e_{ft} less than 2% (good estimations of $\hat{\xi}'_{(i)-}$ correspond to 3948 dipoles in total) we have e_{lin} with an average of $4.4 \cdot 10^{11}$% and a median of 30% (bad estimations of $\hat{\mathbf{X}}_d$ with the linear combination method).

Study of data without noise for multiple sensors: at this point we are interested in studying the behavior of a lunometer with multiple sensors and how it affects the results of the linear combination method. To investigate this scenario we conducted experiments for data without noise, but this time we use 11 sensors instead of 3. We use the Setup 1.4 for the 6000 dipole experiments for a single measurement position as described in Chapter 1.
For this setup of experiments the general results of our analysis are the following:

Experiment	Average e_{lin}	# of excluded cases	# of dipoles with $e_{lin} > 1000\%$	# of dipoles with $e_{lin} > 50\%$
Setup 1.4	17.2	0	0	694

Though we do not exclude any dipole with the linear combination method, we have to address that 3 cases are not taken into account due to the planes method. That happens because these cases have $\text{Arg}(\hat{\xi}'_{(i)-})$ with range bigger than 90°. For these experiments, the results are better compared to the 3 sensors experiments. Once again we computed the condition number of the linear combination system. This time the mean condition number is 12 with a median condition number equal to 9.5. Note also that here the average e_{lin} is 17,2%. The distribution of the log of the condition numbers for this experiment is given in Figure 3.10.

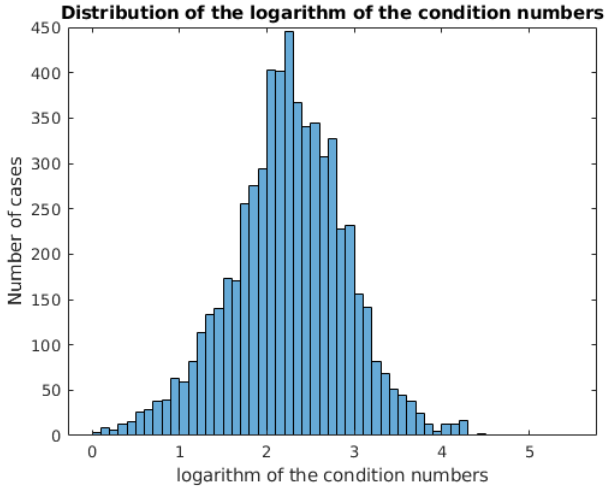

Figure 3.10: This picture illustrates the logarithm of the condition number, for the 5997 remaining cases of the experiments of Setup 1.4 for data without noise (from a single measurement position) and with 11 sensors. For this experiment we use the linear combination method.

One first observation from our experiments, is that when we use 11 sensors the maximum e_{lin} is 247%. In Figure 3.11 one can see the dipoles which provide e_{lin} more than 100%. Those cases correspond to 179 dipoles in total, which represent 3% of the measurements. Once again we observe good estimations of e_{ft} does not translate to small e_{lin}. Finally the distribution of the e_{lin} and the mean e_{lin} by radius can be seen in Figures 3.12(a) and (b) respectively. Note that we illustrate the information of mean e_{lin} by radius only for the 11 sensors. That happens because in the case with the 3 sensors in our previous experiments we have many cases with big errors that influence our results. From the e_{lin} distribution we can see that more than 50% of the dipole experiments provide us with e_{lin} less than 5%. Another

interesting observation is the behavior of the mean e_{lin} with respect to the measurement radius which denotes that dipoles which are located further from the revolution axis and consequently are closer to the sensors provide us with better results. This observation is consistent with the analysis we completed in Chapter 2.

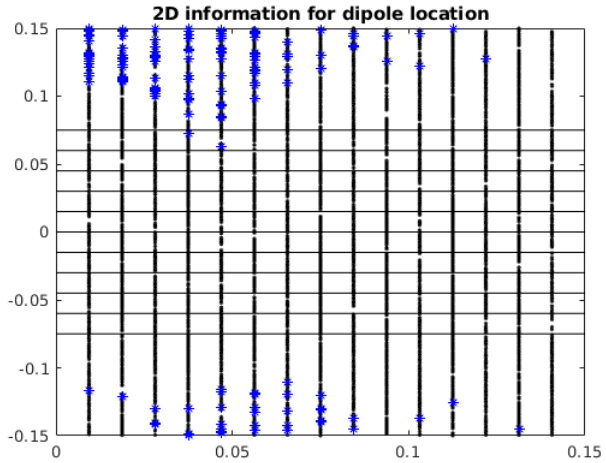

Figure 3.11: The vertical axis shows the information z_d and the horizontal axis the information $|\xi_d|$ for the 6000 generated dipole locations (black dots). The black horizontal lines correspond to the heights of the sensors. The blue stars illustrate dipole locations that provide us with error more than 100%. For this experiments we use the linear combination method.

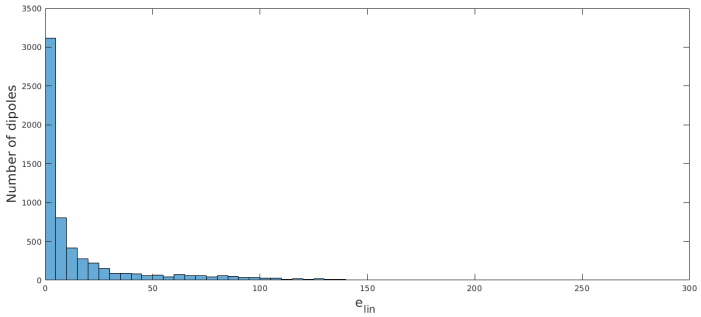

(a)

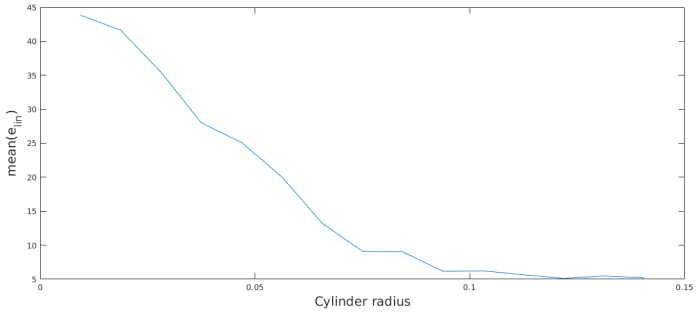

(b)

Figure 3.12: The top picture illustrates the distribution of the e_{lin} error for the linear combination method. Its vertical axis corresponds to the number of dipoles and its horizontal axis to the e_{lin} error. The bottom picture illustrates the mean e_{lin} (vertical axis) with respect to the cylinder radius (horizontal axis).

In conclusion linear combination method performs poorly with the current lunometer's configuration despite the fact that we use synthetic ideal data. It does have the potential to provide better results (for instance with the use of 11 sensors) but for the scope of this study the main observation is its high sensitivity.

3.4 Parabola method

The first goal of the parabola method is to estimate the height z_d of the dipole location, by knowing that information we can further compute also the $|\xi_d|$. As happened with the previous methods, parabola method can be used either for a single measurement position or with a combination of two or three measurement positions. The idea of this method is the following, each measurement position allows one to estimate a height to which $\hat{\mathbf{X}}_d$ belongs. This height (which is related to the vertex of the parabola) defines

a plane parallel to the measurement plane. We can have in total 3 of those planes due to the different measurement positions, each recovered plane has information for the heights of the dipole $\mathbf{X}_d$ which are associated with the $\hat{z}_d$, $\hat{x}_d$ and $\hat{y}_d$ information for the first, second and third measurement position respectively. Hence a combination of all three recovered planes should provide us with an estimate of the $\hat{\mathbf{X}}_d$.
The parabola method is a geometrical method inspired from Lemma 4. When we studied the function $\aleph(\rho)$ at the beginning of this chapter we get the expression

$$\aleph(\rho) = \frac{1 + |\xi'_d|^2 + \rho^2}{|\xi'_d|}.$$

In the generic case when $|\xi'_d| \neq 0$, one can observe that this expression has the form of a vertical parabola which attains its minimum value at $\rho = 0$ (which is equivalent to $h = h_d$). We will focus our study on the general case where $|\xi'_d| \neq 0$.
By expanding the term $(h - h_d)^2$ of Equation (3.6) we get:

$$\lambda_h = \frac{1}{|\xi'_d|}h^2 - \frac{2h_d}{|\xi'_d|}h + \frac{1 + |\xi'_d|^2 + h_d^2}{|\xi'_d|}. \tag{3.7}$$

Equation (3.7) has the form $\lambda_h = \alpha h^2 + \beta h + \gamma$ (which is the standard form of a horizontal parabola see Figure 3.13) with h varying on the vertical axis and λ_h varying on the horizontal axis where the coefficients α, β and γ are unknown.
Now, in theory, in order to recover a parabola equation (compute the coefficients $\alpha, \beta, \gamma \in \mathbb{R}$) one only needs to know three of its points. In our study the parabola points $(\lambda_{h_i}, h_i) \in \mathbb{R}^2$ are defined from the heights of the sensors h_i with $i = 1, ..., S$ and from the estimated λ_{h_i} coefficients. This brings us back to solve a linear problem with the same logic as we did in the linear combination method before. This time the system we want to solve is the following:

$$\begin{cases} \alpha h_1^2 + \beta h_1 + \gamma = \lambda_{h_1}, \\ \alpha h_2^2 + \beta h_2 + \gamma = \lambda_{h_2}, \\ \qquad\qquad \vdots \\ \alpha h_S^2 + \beta h_S + \gamma = \lambda_{h_S} \end{cases}$$

Which we can express in a matrix form as $A\mathrm{x} = B$ with:

$$A = \begin{bmatrix} h_1^2 & h_1 & 1 \\ h_2^2 & h_2 & 1 \\ \vdots & \vdots & \vdots \\ h_S^2 & h_S & 1 \end{bmatrix}, \ \mathrm{x} = \begin{bmatrix} \alpha \\ \beta \\ \gamma \end{bmatrix} \text{ and } B = \begin{bmatrix} \lambda_{h_1} \\ \lambda_{h_2} \\ \vdots \\ \lambda_{h_S} \end{bmatrix}.$$

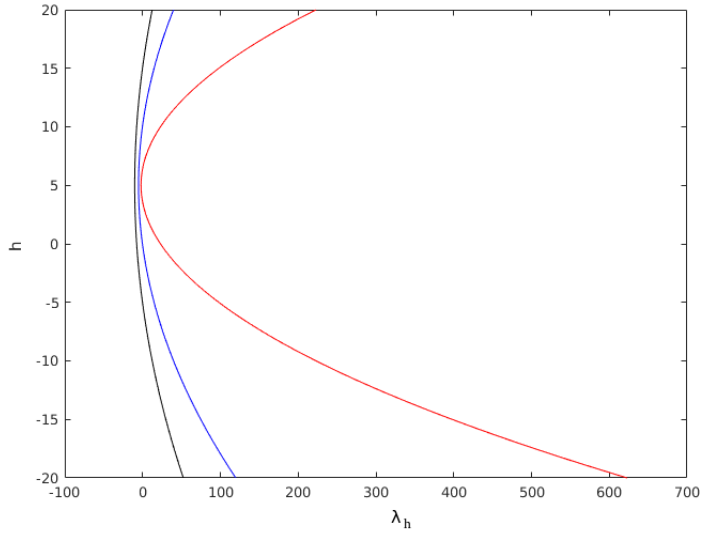

Figure 3.13: This is an illustration of three different examples of parabola in Equation (3.7). The one in black corresponds to $|\xi_d'| = 1$, the one in blue to $|\xi_d'| = 5$, and the one in red to $|\xi_d'| = 10$. For this illustration the height of the dipole is set to be $h_d = 5$.

For $S \geq 4$, the above linear system of S equations is overdetermined. So we can use the Moore-Penrose pseudo-inverse matrix $A^+ = (A^T A)^{-1} A^T$ where A^T is the transposed matrix of A and we can compute the solution to the least squares problem as $\hat{\mathrm{x}} = A^+ B$. For the special case where $S = 3$ we have three equations with three unknowns and by solving the linear system of these equations we can define the parabola.
The first point we are interested in calculating with the parabola method is the vertex of the parabola, because at that point we get $h_i = h_d = z_d/R$ and this is where the parallel plane with respect to our measurement plane will be located. When h_d is known, one could consider also to recover the information for $|\xi_d'|$ since its value is related to the computed coefficients α, β, γ. Due to time limitations we didn't study these relations. However it is interesting information for further research. In order to test the parabola method we conduct experiments with synthetic ideal data.

3.4.1 Test of the parabola method, simulations with synthetic data

Study of data without noise for the current lunometer configuration: in order to test the parabola method, we conduct experiments with ideal synthetic data. At first we use the Setup 1.3 of the experiments as described in Chapter 1. This is the setup with the 6000 dipoles located on

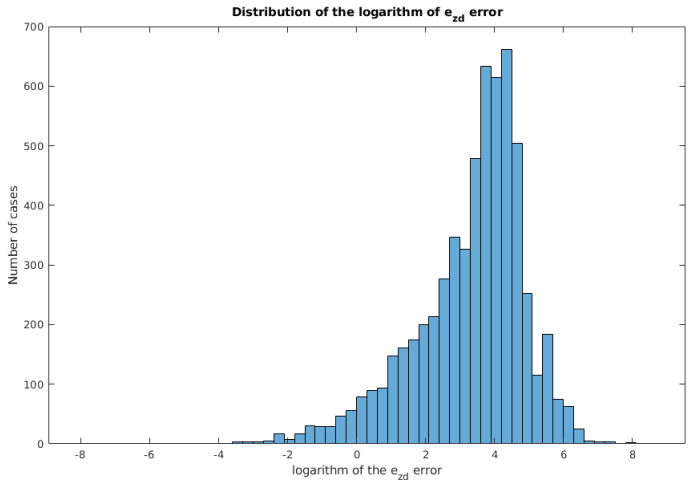

Figure 3.14: This picture illustrates the distribution of the logarithm of the e_{z_d} error for the parabola method with 3 sensors measurements form a single position.

the surfaces of concentric cylinders. We use one measurement position with the current lunometer configuration of the 3 sensors. The goal of this experiment is to test how sensitive the parabola method is under ideal conditions. To do that we compute the parabola peak percentage error e_{z_d} as follows

$$e_{z_d} = \frac{|\hat{z}_d - z_d|}{R} \cdot 100. \tag{3.8}$$

The obtained results are as follows:

Experiment	Averaged percentage e_{z_d}	# of excluded cases	# of cases with e_{z_d} more than 1000%	# of cases with e_{z_d} more than 50%
Setup 1.3	67.6%	18	10	2483

With the current lunometer configuration from the 6000 dipoles of our experiment, we exclude in total 18 cases. Those 18 cases concern dipoles for which the $\xi'_{(i)-}$ estimations have the same value at each height h_i. In those cases our Matlab computations provide us with the value NaN as the solution for the parabola peak. For the remaining 5982 cases the averaged percentage e_{z_d} of the parabola method is 67.6%.

This large averaged e_{z_d} error, is strong evidence that with the current lunometer configuration, parabola method is too sensitive. Indeed 41% of our experiments provide us with $e_{z_d} > 50\%$. The distribution of the logarithm of the e_{z_d} error can be seen in Figure 3.14

Study of data without noise for multiple sensors: to complete the study of this method we also conducted ideal data experiments with 11 sensors, we used the Setup 1.4 as described in Chapter 1. The goal of these experiments is to verify if more sensors could increase the accuracy of the parabola method. The general results of our analysis are the following:

Experiment	Averaged percentage z_d error	# of excluded cases	# of cases with error more than 1000%	# of cases with error more than 50%
Setup 1.4	81.1%	0	74	707

For the second experiment we have 11 sensors. Once again we have to address that 3 cases are not taken into account due to the planes method, for cases with $\text{Arg}(\hat{\xi}'_{(i)-})$ and a range larger than 90°. This is something we expected because we have already studied this setup of experiments with the linear combination method. For the rest of the cases the averaged e_{z_d} error is 81.1%. This result is a little bit misleading because the error increases with more sensors due to the fact that we get more cases with $e_{z_d} > 1000\%$ (74 cases in total) but at the same time we have only 11% of our experiments which provide us with $e_{z_d} > 50\%$. The distribution of the logarithm of the e_{z_d} error can be seen in Figure 3.15

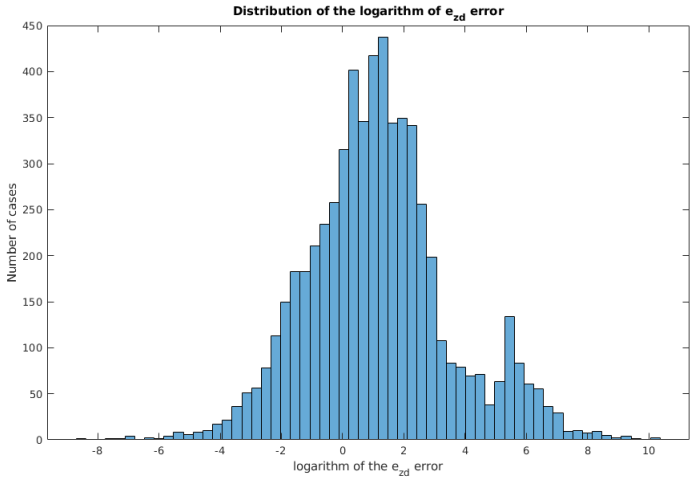

Figure 3.15: This picture illustrates the distribution of the logarithm of the e_{z_d} error for the parabola method with 11 sensors measurements form a single position.

The studies so far have shown, that the planes method is a good approach in restricting the search area for the dipole location $\mathbf{X}_d$. We can also see that with the current lunometer configuration, both the linear combination and the parabola method show sensitivity to estimate the information related to $\hat{\mathbf{X}}_d$ location. We continue our study with another geometrical method, that

of circles method.

3.5 Circles method

With this method, our goal is to recover an $\hat{\mathbf{X}}_d$ estimation for the dipole location through the geometrical study. The circles method can also provide us with an estimation $\hat{\mathbf{X}}_d$ for each measurement position. The circles method is also based on Equation (3.6)

$$\lambda_{h_i} := \frac{1 + |\xi'_d|^2 + (h_i - h_d)^2}{|\xi'_d|} = t_{(i)+} + t_{(i)-}$$

which we can rewrite as:

$$\lambda_{h_i}|\xi'_d| = 1 + |\xi'_d|^2 + (h_d - h_i)^2 \Leftrightarrow (h_d - h_i)^2 + (|\xi'_d|^2 - \lambda_{h_i}|\xi'_d|) = -1.$$

By completing the square of the term $(|\xi'_d|^2 - \lambda_{h_i}|\xi'_d|)$ (namely with the addition and subtraction of the term $\frac{\lambda_{h_i}^2}{4}$) we get:

$$\left(|\xi'_d| - \frac{\lambda_{h_i}}{2}\right)^2 + (h_d - h_i)^2 = \frac{\lambda_{h_i}^2}{4} - 1. \tag{3.9}$$

From the proof of Lemma 1 which we study at the beginning of this chapter in the section of the Denominator analysis, one can observe that $\Delta = \lambda_{h_i}^2 - 4$ (λ_{h_i} defined from Equation (3.6)) and we get that $\frac{\lambda_{h_i}^2}{4} - 1 > 0$.
Equation (3.9) implies that $(|\xi'_d|, h_d)$ lies on the circle with center $C_i = \left(\frac{\lambda_{h_i}}{2}, h_i\right)$ and radius $r_i = \frac{1}{2}\sqrt{\lambda_{h_i}^2 - 4}$.
Actually in Equation (3.9) if we replace ξ'_d and h_d by $t_{(i)-}$ and h_i respectively the equation still holds. More precisely by replacing and doing computations at the left part of Equation (3.9) we get:

$$\left(t_{(i)-} - \frac{t_{(i)+} + t_{(i)-}}{2}\right)^2 + (h_i - h_i)^2 = \left(\frac{2t_{(i)-} - t_{(i)-} - t_{(i)+}}{2}\right)^2$$
$$= \frac{(t_{(i)-} - t_{(i)+})^2}{4} = \frac{t_{(i)+}^2 + t_{(i)-}^2 - 2}{4}.$$

Now for the right part of Equation (3.9) we get:

$$\frac{\lambda_{h_i}^2}{4} - 1 = \frac{(t_{(i)+} + t_{(i)-})^2}{4} - 1 = \frac{t_{(i)+}^2 + t_{(i)-}^2 + 2 - 4}{4} = \frac{t_{(i)+}^2 + t_{(i)-}^2 - 2}{4}.$$

From the above computations we can see that the point $(t_{(i)-}, h_i)$ belongs on the circle of Equation (3.9). We can work with a similar method for the point $(t_{(i)+}, h_i)$.

For the current lunometer configuration we have three sensors $i = 1, 2, 3$ from which we get three circle equations. Theoretically, those circles must intersect at the actual dipole location $\mathbf{X}_d$. However numerical simulations reveal that we can not compute a single intersection point even for ideal data due to approximation errors of our methods (RARL2 is initialized by grid method and computes an approximation of $\xi'_{(i)-}$ and not the exact theoretical value). In addition floating point / rounding errors of Matlab also contribute to the uncertainty of our result. Figure 3.16 illustrates this behavior.

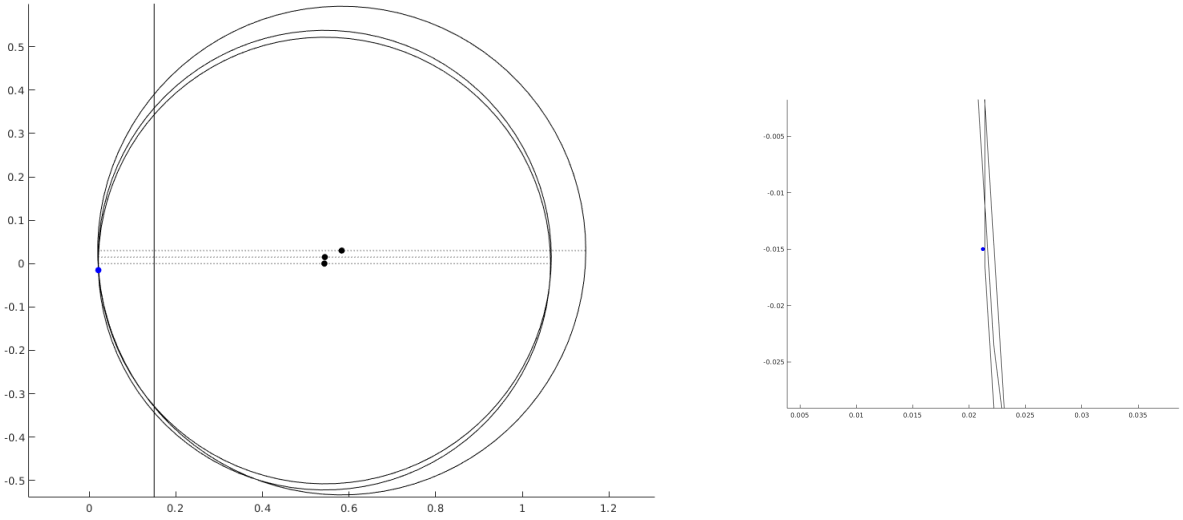

Figure 3.16: The picture on the left is an illustration of a theoretical intersection example of the three circles. For a dipole placed at $X_d = [0.015, 0.015, 0.015]$ with moment $M_d = [0.0723, 0.0721, 0.9948] \cdot 10^{-3}$ for data without noise from the second measurement position. The vertical black line indicates the sensors distance from the origin of our coordinate system $R = 0, 15$. The picture on the right is a close up of the area close to the dipole location (blue dot) from the first picture.

Another interesting observation comes from the circle center $C_i = \left(\frac{\lambda_{h_i}}{2}, h_i\right)$ and the use of Equation (3.6). From Equation (3.6) we know that $\lambda_{h_i} = t_{(i)-} + t_{(i)+} = |\xi'_-| + |\xi'_+|$. That means that the circle center is located at the middle of the segment defined by the points $(t_{(i)-}, h_i)$ and $(t_{(i)+}, h_i)$ where h_i is the height of the sensor, $t_{(i)-} = |\xi'_-|$ is the value of the pole estimation and $t_{(i)+} = \dfrac{1}{t_{(i)-}}$ can be computed from $t_{(i)-}$. This provides us with the information that we can use to compute the diameter of the circle (C_i, r_i)

from the points $(t_{(i)-}, h_i)$ and $(t_{(i)+}, h_i)$.

Remark 6 *From Lemma 4 we know that t_- attains its maximum value at $h = h_d$. Moreover, from the first Vieta's formula (3.4), we know that $t_+ = \frac{1}{t_-}$ with $0 < t_- < 1$. That means that at height $h = h_d$, not only t_- attains its maximum value but at the same time t_+ attains its minimum value. Since the points (t_-, h) and (t_+, h) define the diameter of the circle (C_i, r_i) we can claim that the circle with the smallest possible diameter must be located at the height $h = h_d$.*

3.5.1 Accuracy of the computed circles, simulations with synthetic data

At this point in order to test if the computed circles which were derived from the $\hat{\xi}'_{(i)-}$ estimations are good approximations of the circles computed from the theoretical poles $\xi'_{(i)-}$, we conduct preliminary experiments with synthetic ideal data for a single measurement position.

Study of data without noise for the current lunometer configuration: our setup of experiments uses the lunometer configuration as described in Setup 1.5. This setup concerns ideal data measurements from a single position for 6000 dipoles spread on the surfaces of concentric cylinders (like the Setup 1.3). This time for each height h_i, $i = 1, 2, 3$ we take measurements of all three of the components of the magnetic field $\mathbf{B}_{[\mathbf{X}_d, \mathbf{M}_d]}(\mathbf{X})$. This can help us to compare the results of each sensor as we did in Chapter 2. We use this setup of experiments only for the circles method because we conducted them at a later stage of our research. At that moment we were already aware that our final selection for our study would be the circles method. For this reason we conduct some extra experiments just for the circles method in order to address different questions we have.
The goal of these preliminary experiments is to test whether the recovered circles of our method are good approximations of the theoretical ones. To evaluate the circles we compute the percentage error e_{radii} for the recovered circles radius with respect to the theoretical ones as follows:

$$e_{radii} = \frac{|\text{Recovered Radius} - \text{Theoretical Radius}|}{\text{Theoretical Radius}} \cdot 100.$$

We also compute the percentage error $e_{hcenter}$ for the coordinate that corresponds to the horizontal axis (we write it in short as: hor) of the circles centers. We normalize this error by dividing with the theoretical radius too as follows:

$$e_{hcenter} = \frac{|\text{Recovered hor center} - \text{Theoretical hor center }|}{\text{Theoretical Radius}} \cdot 100.$$

The following table gathers the information for the average of e_{radii} and $e_{hcenter}$ per sensor and per corresponding height.

	B_r			$B_\perp$			B_τ		
heights	0	0.015	0.030	0	0.015	0.030	0	0.015	0.030
average e_{radii}	4.7	4.8	5.1	1.9	1.9	2.0	3.7	3.4	3.7
average $e_{hcenter}$	3.6	3.7	3.9	1.3	1.3	1.4	3.2	2.9	3.1

The first observation from the above table is that both average errors are small. The second observation is that their values barely vary with respect to the height, and they depend on the sensor. We also observe that the cases with $e_{radii} > 50\%$ and the cases with $e_{hcenter} > 50\%$ coincide. For this reason we have evidences that a comparison of our computed circles with the theoretical ones, can be based either by comparing their radius or by comparing their centers, hence we can further focus our study only on e_{radii}. In Figure 3.17 we can see the distributions of the e_{radii} and $e_{hcenter}$ for each sensor for height $h = 0$ (the other two height $h = 0.015$ and $h = 0.03$ have similar distributions). This is a good result because it confirms that the consistency of our analysis does not depend on the height of the measurements but on the measurement component. Interestingly enough, some features of the e_{radii} distribution remind us of the results we observed in Chapter 2, namely the B_r sensor has a distribution with a long right tail, the B_τ sensor has a distribution with two peaks though this time the peak of the distribution error is located close to 30% instead of 40% and the $B_\perp$ sensor has a fast decrease. In any case, those results show consistency with our previous analysis. From a general point of view, it seems that a multiple sensor lunometer constructed with $B_\perp$ sensors can provide better results for our estimation of $\hat{\mathbf{X}}_d$ dipole location. This is something that we will test in Chapter 5.

In conclusion, from our analysis with perfect data the recovered circles can be considered as good approximations of the theoretical ones. The key information now is the link between the intersection point between the C_i circles and the dipole location $\mathbf{X}_d$ as provided from Equation (3.9). The difficulty we face now, is how we can recover this intersection point since, even with ideal data, Matlab does not provide us with a unique common intersection point among the circles, see Figure 3.16. For this reason a pseudo-intersection point must be defined. The next chapter is dedicated to that issue and explains in more detail how we can compute such a point. Numerical simulations and examples are also provided.

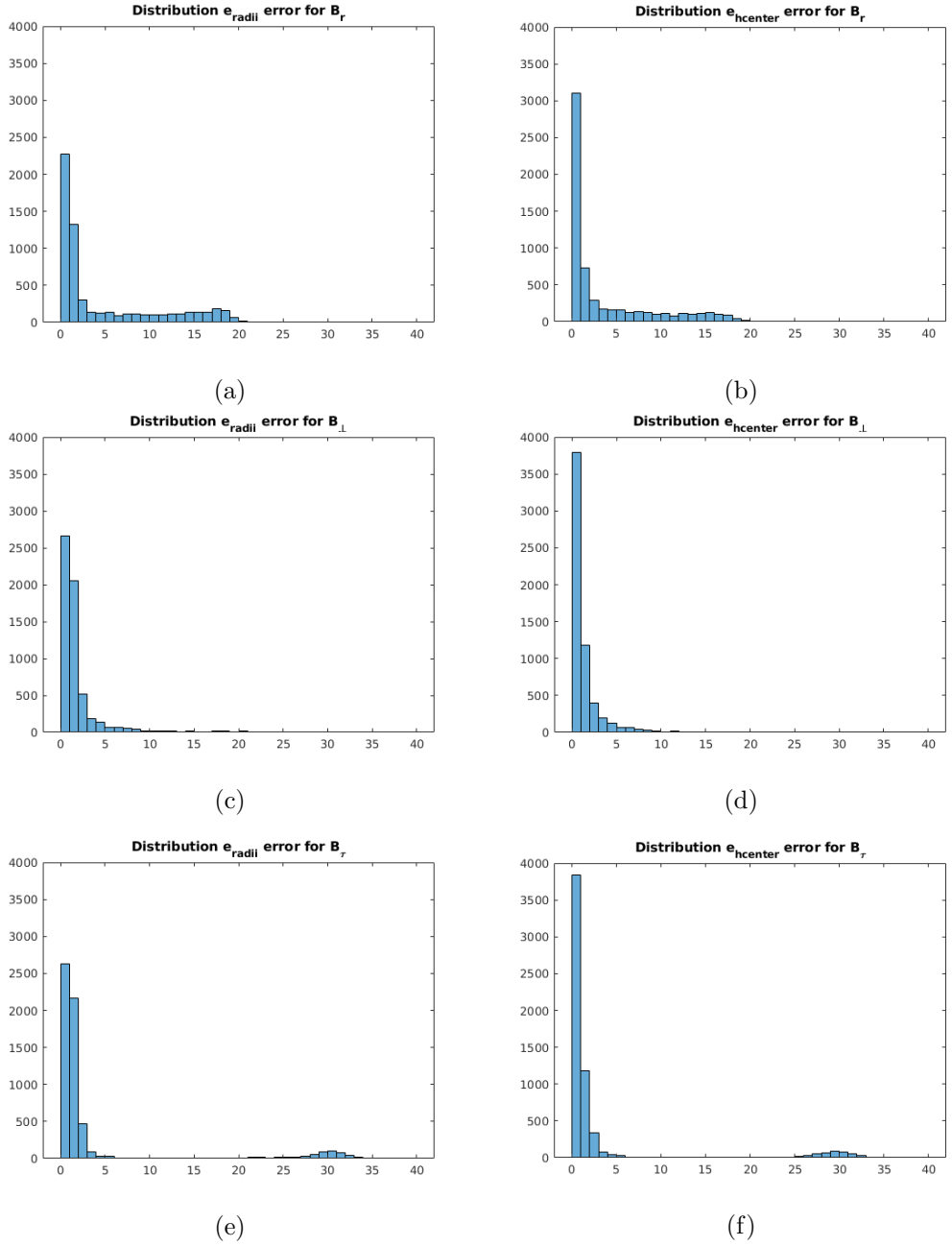

Figure 3.17: Pictures on the left have as vertical axis the number of the dipoles, and as horizontal axis the e_{radii}. Pictures on the right have as vertical axis the number of the dipoles, and as horizontal axis the $e_{hcenter}$. All of the pictures concern results of the circles method for ideal data from a single measurement position. For these illustrations the sensors height is $h = 0$.

CHAPTER 4

Circles pseudo-intersection (3D)

In this chapter we address the problem of how to define an intersection point for the circles method (this problem is illustrated in Figure 3.16). We call our recovered solution "pseudo-intersection" point $\hat{\mathbf{X}}_d$. Note that we have a "pseudo-intersection" point $\hat{\mathbf{X}}_d$ (for each measurement position). In theory $\hat{\mathbf{X}}_d$ must coincide with the actual intersection point $\mathbf{X}_d$ of the given $S \geq 3$ circles whenever it exists.

In this section we investigate three methods for computing a pseudo - intersection point $\hat{\mathbf{X}}_d$, namely the radical center, the minimization of the sum of the distances to three circles and the minimization of the sum of the squares of powers of a point with respect to given circles. The first two methods apply only when $S = 3$, in contrast to the third one where the number of circles can be $S \geq 3$. The radical center is a simplistic approach to solve our problem for three given circles. The minimization of the sum of the distances to three circles is solved by computing a finite list of points among which the minimization point must belong. Finally the third method relies on finding the common roots of two polynomials of a single variable. Each method provides a pseudo-intersection point $\hat{\mathbf{X}}_d$ with different sensitivity and characteristics which are studied. Note that the notation $\hat{\mathbf{X}}_d$ contain the 3D information of the dipole location (namely $(\hat{\xi}_d, \hat{z}_d)$), however when we study each measurement position individually we also use the notation $\hat{\mathbf{x}}_d$ which contain the 2D information of the dipole location $(|\hat{\xi}_d|, \hat{z}_d)$ for each measurement position. Numerical simulations illustrate the robustness and the properties of each method. At the end of this chapter we discuss how we can combine the information from different measurement positions by using the idea of the centroid and compute a final $\hat{\mathbf{X}}_d$ estimation. At that point we use the notation $\hat{\mathbf{X}}_d(p)$ with $p = 1, 2, 3$ for the recovered 3D information of the dipole location for each measurement position and the notation $\hat{\mathbf{X}}_d$ for their combination.

We also discuss a rough approximation which we use in [20]. In Chapter 5 we

conduct more simulations with synthetic data and we compare their results.

4.1 Radical center

The current lunometer configuration restricts the use of information from $S = 3$ circles. A natural and easy idea for a pseudo-intersection point estimation $\hat{\mathbf{x}}_d$ is by computing the radical center [38, ch.3] (also called power center) of those three circles. This method consists of computing firstly the three radical axes of the pairs of circles and secondly the intersection point of those axes. A description and numerical simulations of this method follow.

Definition 4 ***Power of a point*** *[38, ch.3, §43].*
The power of a point $P = (x, y) \in \mathbb{R}^2$ with respect to a circle C_i centered at $(x_i, y_i) \in \mathbb{R}^2$ with radius $R_i > 0$, is the real number $h_i(x, y)$ defined as:

$$h_i(x, y) = (x - x_i)^2 + (y - y_i)^2 - R_i^2, \tag{4.1}$$

and it indicates the "relative distance" of the point $P = (x, y)$ to a given circle C_i.

Remark 7 *Note that from the definition the following properties hold.*

$$\begin{aligned} &P \in C_i \Leftrightarrow h_i(x, y) = 0, \\ &P \in D_i \Leftrightarrow h_i(x, y) < 0, \\ &P \in \mathbb{R}^2 \backslash \overline{D_i} \Leftrightarrow h_i(x, y) > 0, \end{aligned}$$

where D_i is the open disk surrounded by the circle C_i and $\overline{D_i} = D_i \cup C_i$ is the closure.

Remark 8 *Note that from the above remark and Equation (4.1) we can deduce that the value of $P = (x, y)$ is getting bigger as we increase its distance from the circle C_i.*

Remark 9 *If there exists a common intersection point $P = (x, y) \in \mathbb{R}^2$ for $N \geq 2$ given circles C_i, then it holds that the corresponding powers h_i of P to C_i vanish:*

$$h_1(x, y) = ... = h_N(x, y) = 0.$$

Definition / Proposition 1 ***Radical axis*** *[38, ch.3, §45]*
The locus of a point P having equal power with respect to two given non concentric circles, is a certain line perpendicular to the line joining their centers which is called the radical axis (or power line) of the circles. If the two circles intersect, this is the line passing through their points of intersections see Figure 4.1.

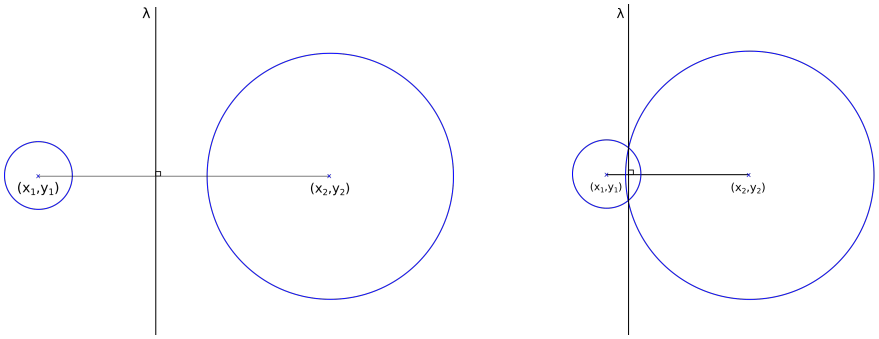

Figure 4.1: The above pictures illustrate the radical axis denoted as line λ for two different cases. The picture on the left shows a case where the two given circles are disjoint and the picture on the right shows a case where the two given circles intersect twice.

Proof. A way to prove that the locus of point $P = (x, y) \in \mathbb{R}^2$ having equal power with respect to two given non concentric circles $h_1(x, y) = h_2(x, y)$ is a certain line, comes from Equation (4.1). Solving Equation (4.1) for the x, y variables we get:

$$h_1(x,y) = h_2(x,y) \Leftrightarrow 2(y_2-y_1)y+2(x_2-x_1)x+x_1^2-x_2^2+y_1^2-y_2^2-R_1^2+R_2^2 = 0.$$

This is an equation of the form $\alpha x + \beta y + \gamma = 0$, with $\alpha = 2(x_2 - x_1)$, $\beta = 2(y_2-y_1)$ and $\gamma = x_1^2 - x_2^2 + y_1^2 - y_2^2 - R_1^2 + R_2^2$. For any non concentric pair of circles (*e.g.* intersecting, overlapping or disjoint circles), this is the equation of a line. ■

Remark 10 *For concentric circles the radical axis expression $h_1(x, y) = h_2(x, y)$ degenerates to $-R_1^2 + R_2^2 = 0$. It holds only when $R_1 = R_2$ which, practically, tells us that the concentric circles intersect if and only if they have the same radius. For the concentric cases where $R_1 \neq R_2$ the set of points with equal power with respect to both circles is empty.*

Theorem 1 ***Radical axes theorem*** *[38, ch.3, §46]*
The radical axes of three pairwise distinct circles, whose centers are not aligned, are concurrent. The point of concurrence is called the radical center see Figure 4.2.

A proof of this theorem is given in [38, ch.3, §46].

Remark 11 *If the centers of three given circles are aligned then their radical axes are parallel, in that case infinity can be considered as their concur point see Figure 4.2.*

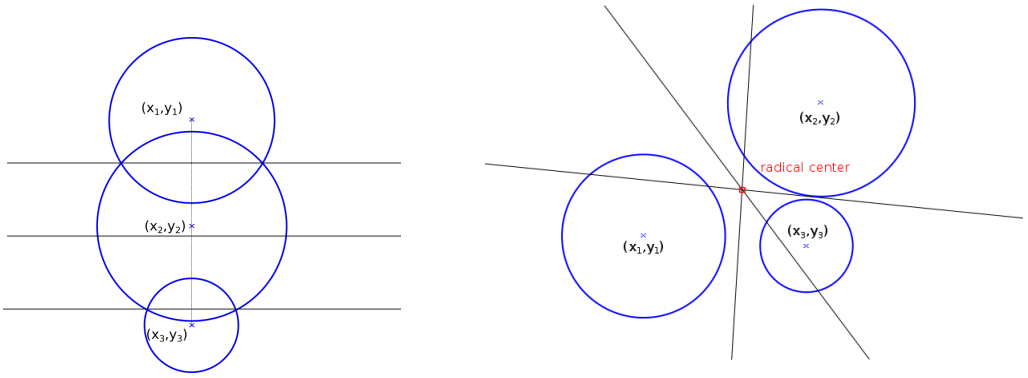

Figure 4.2: The above pictures illustrate two configurations for the circles centers (x_i, y_i), $i = 1, 2, 3$: aligned (left picture) and not aligned (right picture). In the first case the radical center can be considered to be the infinity, for the second case the radical center is shown as a red square.

Radical center is our first candidate for a pseudo-intersection point $\hat{\mathbf{x}}_d$. Indeed if there exists a common intersection point (x, y) for the three given circles of our study, then it must hold that $h_1(x, y) = h_2(x, y) = h_3(x, y) = 0$. This is a special case of the radical center which from Definition/Proposition 4 and Theorem 1 needs to satisfy the system of equations:

$$\begin{cases} h_1(x, y) = h_2(x, y), \\ h_2(x, y) = h_3(x, y), \\ h_1(x, y) = h_3(x, y). \end{cases}$$

The radical center at point $P = (x, y)$ is a very particular point for which the power of a point with respect to each one of the three given circles, is the same. From Remarks 7 and 8 we know that we prefer the power of a point at $P = (x, y)$ to be close to zero. For this reason radical centers with values close to zero are good candidates for our pseudo-intersection point in contrast to radical centers with big values that indicate that $P = (x, y)$ is far away from our circles.

4.1.1 Test of radical center method, simulations with synthetic data

Study without noise for the current lunometer configuration: to analyze the behavior of this method, we conduct experiments for 6000 dipoles without noise, for one measurement position, that are located on the surfaces of 15 concentric cylinders as described in Setup 1.3.
To analyze our data we compute the pseudo-intersection radical center percentage error (e_{pi_rc}) between the estimated $\hat{\mathbf{x}}_d$ and the theoretical pseudo-

intersection point $\mathbf{x}_d$, normalized by the radius R of our sensors distance from the revolution axis as follows:

$$e_{pi\_rc} = \frac{|\hat{\mathbf{x}}_d - \mathbf{x}_d|}{R} \cdot 100. \tag{4.2}$$

The theoretical pseudo-intersection point $\mathbf{x}_d$ is computed by using the information of the actual dipole location $\mathbf{X}_d$ (forward problem). The general results of our analysis are the following:

Experiment	Average e_{pi_rc}	# of excluded cases	# of dipoles with error more than 1000%	# of dipoles with error more than 50%
Setup 1.3	$4.4 \cdot 10^{11}$	0	72	3295

The first observation for this method is that we never encounter a situation where the radical center is at infinity. However, it has a high sensitivity with the median value of e_{pi_rc} equal to 56%. In Figure 4.3 one can see the dipoles that produce error more than 1000%. By studying those cases we observe that their $\hat{\xi'}_{(i)-}$ results almost align, in fact the pairwise differences between $\hat{\xi'}_{(i)-}$ differ after the second decimal in their real or imaginary part.

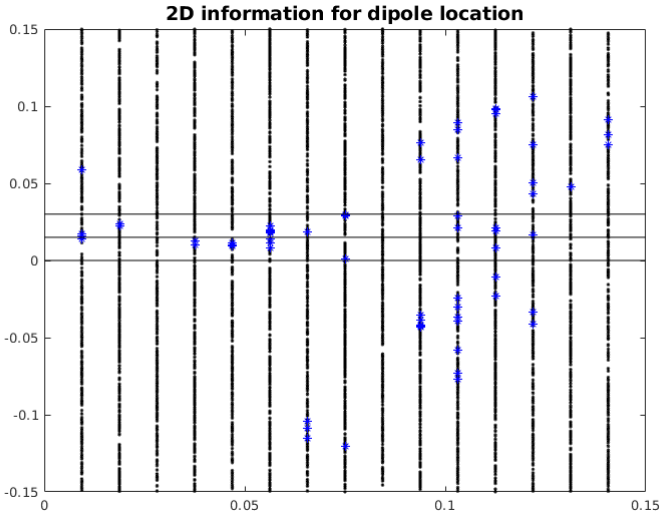

Figure 4.3: In this illustration the vertical axis shows the information z_d of the dipole location $\mathbf{X}_d$ and the horizontal axis the information $|\xi_d|$. The 6000 generated dipole locations (black dots) and the black lines correspond to the heights of the sensors. The blue stars illustrate dipole locations that provide us with error more than 1000%. These experiments concern ideal data processed with the radical center method.

The distribution of the e_{pi_rc} percentage error of the radical center method

can be seen in Figure 4.4. The behavior of the radical center method, is linked with the RARL2 poles estimations $\hat{\xi}'_{(i)-}$ and the circles we compute from them . Because the heights h_i of the sensors are close one to another, the $\hat{\xi}'_{(i)-}$ estimations tend to provide us with circle centers that in many cases are almost vertically aligned. That makes the radical axes concur at a point far away from the circles. This feature in addition with the fact that the method can be used only for $S = 3$ circles suggest that we should investigate other methods to compute a pseudo-intersection point $\hat{\mathbf{x}}_d$.

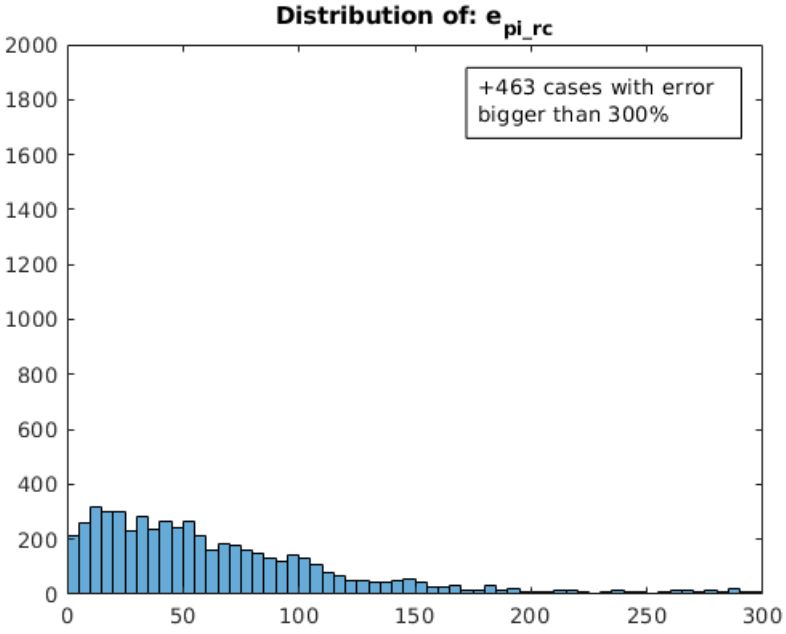

Figure 4.4: This picture illustrates the distribution of the e_{pi_rc} error for the radical center method. The vertical axis corresponds to the number of the dipoles and the horizontal axis corresponds to the e_{pi_rc} percentage error. These experiments concern ideal data form a single measurement position.

Note that since the radical center method performs poorly for ideal data there is no reason to test it for data contaminated with noise. Also, the fact that it is limited to $S = 3$ sensors does not allow us to conduct simulations with more sensors either.

4.2 Minimizing the sum of the distances to three given circles

The stability issues of the radical center naturally leads to the following informal question: does there exist a point $P = (x, y) \in \mathbb{R}^2$ the distance of which is minimum with respect to three given circles? To answer this question we need to define first the distance of a point to a circle.

Definition 5 ***Distance of a point to a circle***
Let a point $P = (x, y) \in \mathbb{R}^2$ and a circle $C_i \in \mathbb{R}^2$ centered at $(x_i, y_i) \in \mathbb{R}^2$ with radius $R_i > 0$. The distance from P to C_i is given by

$$d_i(P) = |\sqrt{(x - x_i)^2 + (y - y_i)^2} - R_i| =: f_i(x, y), \tag{4.3}$$

which defines a function $f_i(x, y)$. Now the question we asked can be expressed as follows: for three given circles C_1, C_2 and C_3, let the vector

$$V(P) = \begin{bmatrix} d_1(P) \\ d_2(P) \\ d_3(P) \end{bmatrix} \in \mathbb{R}^3,$$

can we find a point $P = (x, y)$ which minimizes its norm?
At this point a selection of a norm is necessary. There are three types of norm usually used, the $\|\cdot\|_1$, $\|\cdot\|_2$ and $\|\cdot\|_\infty$. The Euclidean $\|\cdot\|_2$ norm, also called least square, is a usual choice when there is no specific reason to select another norm and because it is associated with an Euclidean space. The uniform $\|\cdot\|_\infty$ norm, is selected when it is important to not neglect isolated large elements in the vector of distances. The $\|\cdot\|_1$ norm, also known as least absolute deviation or least absolute error, minimizes the sum of the absolute differences between the target value and the estimated values. In our case the $\|\cdot\|_1$ norm leads us to a tractable problem, with good geometric properties (for the three given circles) for this reason is the choice of preference.

Remark 12 *The $\|\cdot\|_1$ norm of the vector $V(P)$ is*

$$\|V(P)\|_1 = \sum_{i=1}^{3} |d_i(P)| = |d_1(P)| + |d_2(P)| + |d_3(P)| = \sum_{i=1}^{3} f_i(x, y) =: f(x, y).$$

Back to our problem for the three given circles, the function $f(x, y)$ is equal to

$$\begin{aligned} f(x, y) = |\sqrt{(x - x_1)^2 + (y - y_1)^2} - R_1| + |\sqrt{(x - x_2)^2 + (y - y_2)^2} - R_2| \\ + |\sqrt{(x - x_3)^2 + (y - y_3)^2} - R_3|, \end{aligned} \tag{4.4}$$

hence it is continuous on $\mathbb{R}^2$ but not differentiable everywhere: in fact f is not differentiable when one of the square roots of the function is equal to zero (hence at the centers of the given circles), and when one of the absolute values of the function is equal to zero. The function f is defined on the entire plane, but its value is increasing when we are moving away from the given circles. Hence we can restrict ourselves to a compact set which includes the given circles. In this compact set, the function f is continuous everywhere, so it has at least one minimum value.

We do not know the exact location of the minimal value but we know where we should search for it. Our strategy is to collect a list of points where this minimum value must be located. This list of points consists from the circles centers, the circles intersection points (if any), the isogonic centers and the Alhazen/"Alhazen-like" points.

From this list the circles centers and the pairwise circles intersections are easy to compute. To complete our list we need to study what happens in the differentiable and the non-differentiable domains of f as follows.

4.2.1 Domains where the function f is differentiable

If the minimum value belongs in the differentiable domain of function f then it must be reached at a critical point. The critical points are necessarily located either outside or inside the disks D_i of the given circles with exception to their centers (x_i, y_i). Because we exclude the domain where the function f is not differentiable, we end up with a function $f(x,y)|_\Delta$ which is differentiable everywhere in its domain Δ with $\Delta = \mathbb{R}^2 \setminus \bigcup_{i=1}^{3} \{C_i, (x_i, y_i)\}$. If a critical point is located outside a disk D_i then the absolute value with respect to that disk in Equation (4.4) can be replaced with a parenthesis. If a critical point is located inside a disk D_i then the absolute value with respect to that disk in Equation (4.4) can be replaced with a parenthesis with a negative sign in front. We do not know where a critical point is located but there are eight possible sub-domains Δ_j, $j = 1, ..., 8$ which we can study, based on the possible circles configurations.

Remark 13 *The possible differentiable sub-domains, for three given circles,*

are the following:

$$\begin{aligned}
\Delta_1 &= \mathbb{R}^2 \setminus \bigcup_{i=1}^{3} \overline{D}_i,\\
\Delta_2 &= D_2 \setminus \{\overline{D}_1 \cup \overline{D}_3 \cup (x_2, y_2)\},\\
\Delta_3 &= D_3 \setminus \{\overline{D}_1 \cup \overline{D}_2 \cup (x_3, y_3)\},\\
\Delta_4 &= D_1 \setminus \{\overline{D}_2 \cup \overline{D}_3 \cup (x_1, y_1)\},\\
\Delta_5 &= (D_1 \cap D_2 \cap D_3) \setminus \{(x_1, y_1) \cup (x_2, y_2) \cup (x_3, y_3)\},\\
\Delta_6 &= (D_1 \cap D_3) \setminus \{\overline{D}_2 \cup (x_1, y_1) \cup (x_3, y_3)\},\\
\Delta_7 &= (D_1 \cap D_2) \setminus \{\overline{D}_3 \cup (x_1, y_1) \cup (x_2, y_2)\},\\
\Delta_8 &= (D_2 \cap D_3) \setminus \{\overline{D}_1 \cup (x_2, y_2) \cup (x_3, y_3)\}.
\end{aligned}$$

For instance, if a critical point is located outside the given disks D_i, $i = 1, 2, 3$ then it belongs in the sub-domain $\Delta_1 = \mathbb{R}^2 \setminus \bigcup_{i=1}^{3} \overline{D}_i$, and the function $f(x, y)|_{\Delta_1}$ takes the form :

$$f(x, y)|_{\Delta_1} = \sum_{i=1}^{3} \left(\sqrt{(x - x_i)^2 + (y - y_i)^2} - R_i \right) =: \mathrm{Expr}_1(x, y). \tag{4.5}$$

Note that the expression on the right hand side of the above equation is differentiable in the whole domain Δ and this expression could have critical points even outside the sub-domain Δ_1. Having the above information in mind, our algorithm makes a list with all possible critical points of f. To do that we look for the critical points (in Δ) of the expressions $\mathrm{Expr}_j(x, y)$, $j = 1, .., 8$. A critical point (x, y) of Expr_j that additionally satisfies that $(x, y) \in \Delta_j$ is an actual critical point of f. Otherwise, it is not a critical point of f, but in any case, our list will collect all possible critical points of f.

Now let us study the gradient of $\mathrm{Expr}_1(x, y)$ (we can work in a similar way for the other $\mathrm{Expr}_j(x, y)$ cases). Without loss of generality we can compute the gradient for only one term of $\mathrm{Expr}_1(x, y)$ and get:

$$\nabla\left(\sqrt{(x - x_i)^2 + (y - y_i)^2} - R_i\right) = \frac{\begin{pmatrix} x - x_i \\ y - y_i \end{pmatrix}}{\left\| \begin{pmatrix} x - x_i \\ y - y_i \end{pmatrix} \right\|}. \tag{4.6}$$

Observe that Equation (4.6) defines a unit vector $u_i(x, y)$.

Remark 14 *The term R_i of Expression* (4.5) *has no influence after the use of ∇ operator. The simplification of R_i term and the unit vectors features in Equation* (4.6) *happens exactly because we use the $\|\cdot\|_1$ norm instead* e.g. *the Euclidean one.*

Proposition 2 *Equation* (4.6) *provides us with three unit vectors* u_1, u_2, u_3 *which come from the three terms of Expression* (4.5). *Depending on the considered expression* $Expr_j$ $(j = 1, ..., 8)$, *we get the following expressions for* $\nabla Expr_j(x, y)$, *for* $(x, y) \in \Delta$:

$$\begin{cases} \nabla Expr_1(x,y) = +u_1(x,y) + u_2(x,y) + u_3(x,y), \\ \nabla Expr_2(x,y) = +u_1(x,y) - u_2(x,y) + u_3(x,y), \\ \nabla Expr_3(x,y) = +u_1(x,y) + u_2(x,y) - u_3(x,y), \\ \nabla Expr_4(x,y) = -u_1(x,y) + u_2(x,y) + u_3(x,y), \\ \nabla Expr_5(x,y) = -u_1(x,y) - u_2(x,y) - u_3(x,y), \\ \nabla Expr_6(x,y) = -u_1(x,y) + u_2(x,y) - u_3(x,y), \\ \nabla Expr_7(x,y) = -u_1(x,y) - u_2(x,y) + u_3(x,y), \\ \nabla Expr_8(x,y) = +u_1(x,y) - u_2(x,y) - u_3(x,y). \end{cases} \tag{4.7}$$

Because in the Expressions (4.7) we are dealing with additions and subtractions of unit vectors and in the case of a critical point we want their combinations to be equal to zero, we can approach the problem geometrically.
For example if $u_1(x, y) + u_2(x, y) + u_3(x, y) = 0$, the addition of vectors can be illustrated by connecting each vector head to tail and the vectors add to zero if the head to tail connections form a closed loop. In our case, as we are dealing with unit vectors, their addition must form an equilateral triangle. A similar reasoning applies for the other expressions, see Figure 4.5. For instance, for the gradient of Expr_2 to be zero, the only difference is the direction of the $u_2(x, y)$ vector. Note also that if three unit vectors add up to zero, by placing their origins at the same point, they form angles as shown in Figure 4.6. Such angle properties hold for any of the expressions $\nabla\text{Expr}_j(x, y) = 0$.

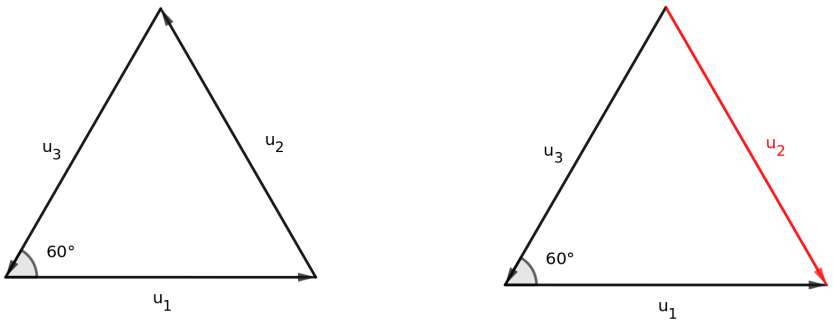

Figure 4.5: The picture on the left illustrates the orientation of the unit vectors if $\nabla\text{Expr}_1(x, y) = 0$. The picture on the right illustrates the orientation in the case when $\nabla\text{Expr}_2(x, y) = 0$.

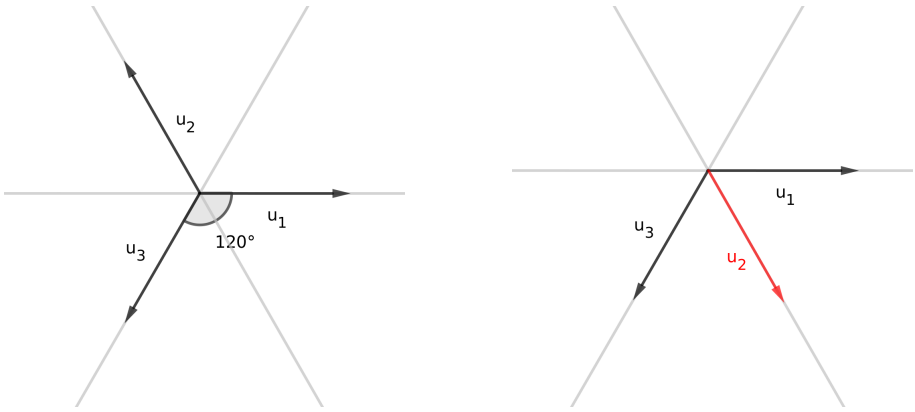

Figure 4.6: Both pictures correspond to rearrangements of the unit vectors of Figure 4.5 with their origins placed at the same point.

Figure 4.6 underlines that, the possible critical points we are interested in computing concern combinations of unit vectors with specific orientations (geometrical characteristics). These geometric characteristics can be described as: when we draw the lines through our potential critical point with respect to the orientations of the unit vectors, then the lines divide the space around the potential critical point, into six equal angles of 60° each.
Based on that observation our question becomes: can we find, for a triangle ABC, all points P such that when we draw the lines through P and the triangle vertices, the space around the points P is divided into six equal angles of 60° each? The answer to that question is yes, in literature there exist some points with the desired geometrical characteristics. They have been called isogonic centers of a triangle and in the Clark Kimberling's encyclopedia of triangle centers[5], they are denoted as $X(13)$ and $X(14)$ respectively.

Definition 6 ([39]) *A point is called an isogonic center of a triangle when the lines drawn through this point to the vertices of the triangle divide the space around it into six equal angles of* 60° *each.*

Our problem now is linked with the isogonic centers through the desired geometrical properties. Instead of computing all the possible critical points of $\nabla \text{Expr}_j(x, y)|_\Delta$ and then searching whether the geometrical properties we want hold, we can just search for the points where we know that the geometrical properties hold. To do this we form a triangle ABC beginning at the circle centers $A = (x_1, y_1)$, $B = (x_2, y_2)$, $C = (x_3, y_3)$ and we search for their isogonic centers.
There are two ways of construction in order to compute the isogonic centers

[5] `http://faculty.evansville.edu/ck6/encyclopedia/ETC.html`

as one can find in [39] and [40]. Both of these are based on the drawing of equilateral triangles on the sides of the given triangle.

Remark 15 *The way we compute the isogonic centers is described in [39] and it is the following. Let ABC be a triangle. For each side of the ABC triangle we draw outwardly equilateral triangles. Then for each equilateral triangle we draw its circumcircle see Figure 4.7. We end up with a concurrent point P among the three circumcircles. That happens because if we take a pair of circumcircles they intersect at a vertex of the triangle and at the point P we are interested about. At P because of the inscribed angles theorem it holds that it faces the sides of the triangle (which are chords of the circumcircles) with an angle of 120° each. That means that it also faces the third face of the triangle with an angle of 120° since $360 - 240 = 120$. Hence the point P must be on the third circumcircle circumference too. This point of concurrency is the first isogonic center $P = X(13)$ of the triangle. If the equilateral triangles were drawn inwardly, then we compute the second isogonic center $P' = X(14)$.*

In [40] they explain how to construct the isogonic centers by drwaing the lines AA', BB' and CC' as one can see in Figure 4.7 (and they also provide a proof).

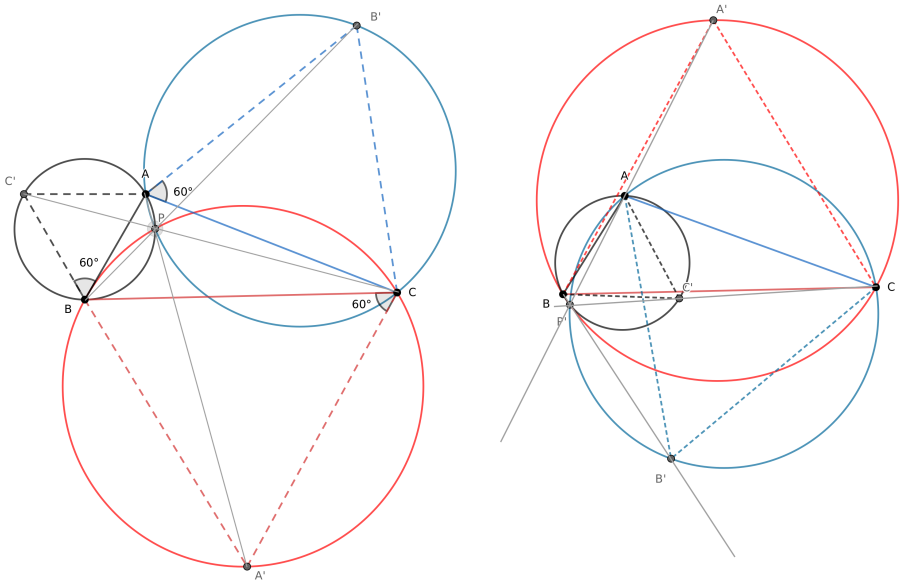

Figure 4.7: The picture on the left illustrates the construction of the first isogonic center $P = X(13)$. The picture on the right illustrates the construction of the second isogonic center $P' = X(14)$.

Remark 16 *In [39] they specify that every triangle has a unique $X(13)$ point. On the other hand the $X(14)$ point is unique for any triangle except*

the equilateral ones. For the equilateral triangles $X(14)$ is anywhere on its circumcircle circumference.

Consequently, if the circles centers $A = (x_1, y_1)$, $B = (x_2, y_2)$, $C = (x_3, y_3)$ do not form an equilateral triangle, the list we construct to contain all critical points of f can be limited to the two isogonic centers $X(13)$ and $X(14)$.

If on the other hand the circles centers $A = (x_1, y_1)$, $B = (x_2, y_2)$, $C = (x_3, y_3)$ form an equilateral triangle, we decide to contain in the list only the first isogonic center $X(13)$ and omit the other. We based this decision in the following idea. If our circles centers form an equilateral triangle there are two possible scenarios with the current lunometer configuration as illustrated in Figure 4.8. That happens because the three heights of the sensors are evenly distributed. The left case of Figure 4.8 is ideal for us because based on symmetrical properties the dipole should be located at the height of $B = (x_2, y_2)$. For this reason a good selection for a possible pseudo-intersection point could be the circle's center $B = (x_2, y_2)$. For the right case of Figure 4.8 we have at least one bad approximation of $\hat{\xi}'_{(i)-}$, in that case any point of the circumcircle circumference could be a pseudo-intersection point. Since the selection for a pseudo-intersection in the second cases is arbitrary we can select to use the three centers $A = (x_1, y_1)$, $B = (x_2, y_2)$, $C = (x_3, y_3)$ as possible pseudo-intersection points. That means that when we deal with equilateral triangles we can omit the point $X(14)$ because the possible pseudo-intersection points we select are already contained in our list (namely the circles centers).

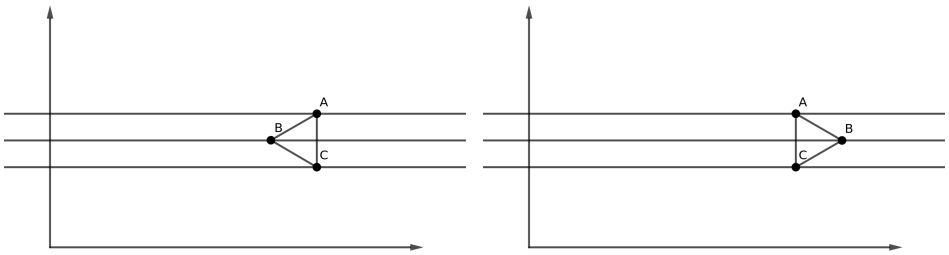

Figure 4.8: The black parallel lines indicate the heights of the sensors. Because of the sensors height limitations, there are only two possible ways the circles centers $A = (x_1, h_1)$, $B = (x_2, h_2)$, $C = (x_3, h_3)$ form an equilateral triangle, as illustrated on the two pictures above.

How we compute the isogonic centers is illustrated with the Algorithm 2.

Now we need to investigate the situation where the minimum of f would be reached at a point where it is not differentiable. The next section is dedicated to that problem.

Algorithm 2 Computation of the isogonic centers

Function: IsogonicCenters
Input: (x_1, y_1), (x_2, y_2), (x_3, y_3) the coordinates of the circles centers
/*For the pseudo-code we denote the circles centers also as C_1, C_2, C_3*/
Output: I_1, I_2 /* the two isogonic centers */

/* Computation of the first isogonic center I_1 */
$A \leftarrow \text{OutwardPointWrt}C_3(C_1, C_2)$
/* it computes the vertex point A of the outward (with respect to the direction of the vertex C_3) equilateral triangle AC_1C_2 */
$B \leftarrow \text{OutwardPointWrt}C_1(C_2, C_3)$
$D \leftarrow \text{OutwardPointWrt}C_2(C_1, C_3)$
$CA \leftarrow \text{CircleTroughPoints}(C_1, C_2, A)$
$CB \leftarrow \text{CircleTroughPoints}(C_2, C_3, B)$
$CD \leftarrow \text{CircleTroughPoints}(C_1, C_3, D)$
$I_1 \leftarrow \text{FindTheConcurrentPointOf}(CA, CB, CD)$
return I_1

/* Computation of the second isogonic center I_2 */
$H_1 \leftarrow \sqrt{(x_2 - x_1)^2 + (y_2 - y_1)^2}$
/* Distance between the points C_1 and C_2 */
$H_2 \leftarrow \sqrt{(x_3 - x_2)^2 + (y_3 - y_2)^2}$
$H_3 \leftarrow \sqrt{(x_1 - x_3)^2 + (y_1 - y_3)^2}$
if $H_1 = H_2$ & $H_2 = H_3$ **then**
  $I_2 \leftarrow []$
else
  $A' \leftarrow \text{InwardPointWrt}C_3(C_1, C_2)$
  /* it computes the vertex point A' of the inward (with respect to the direction of the vertex C_3) equilateral triangle $A'C_1C_2$ */
  $B' \leftarrow \text{InwardPointWrt}C_1(C_2, C_3)$
  $D' \leftarrow \text{InwardPointWrt}C_2(C_1, C_3)$
  $CA' \leftarrow \text{CircleTroughPoints}(C_1, C_2, A')$
  $CB' \leftarrow \text{CircleTroughPoints}(C_2, C_3, B')$
  $CD' \leftarrow \text{CircleTroughPoints}(C_1, C_3, D')$
  $I_2 \leftarrow \text{FindTheConcurrentPointOf}(CA', CB', CD')$
end if
return I_2

4.2.2 Domains where the function f is non differentiable

The domain where f is not differentiable consists of the circles centers (x_i, y_i), the possible intersection points and the circles circumferences C_i, with $i = 1, 2, 3$. We already discussed that the circles centers and the intersection points are treated separately in our list, hence in this subsection we are interested in investigating what happens on the domain

$$\Gamma = (C_1 \cup C_2 \cup C_3) \backslash (\{\text{intersections}\} \cup (x_1, y_1) \cup (x_2, y_2) \cup (x_3, y_3)).$$

Notice that we do not know whether the point $P = (x, y)$ which minimizes the norm $V(P)$ belongs to this domain, however we can study what properties this point should satisfy if it were to belong to this domain. Without loss of generality, we can assume that the point $P = (x, y)$ belongs to the first given circle C_1 (we can work with a similar method for the other two cases C_2 and C_3). On C_1, $f(x, y)$ takes the form

$$f(x,y)|_{C_1} = |\sqrt{(x-x_2)^2 + (y-y_2)^2} - R_2| + |\sqrt{(x-x_3)^2 + (y-y_3)^2} - R_3|. \tag{4.8}$$

Reasoning by cases as we did before, we partition C_1 into different sub-domains where the sign of each term inside the absolute values is fixed.

Remark 17 *The possible sub-domains are the following:*

$$\begin{aligned}
&\Gamma_1 = C_1 \backslash \{\overline{D}_2 \cup \overline{D}_3\},\\
&\Gamma_2 = C_1 \cap \overline{D}_2 \backslash (\{\text{intersections}\} \cup \overline{D}_3 \cup (x_2, y_2)),\\
&\Gamma_3 = C_1 \cap \overline{D}_3 \backslash (\{\text{intersections}\} \cup \overline{D}_2 \cup (x_3, y_3)),\\
&\Gamma_4 = C_1 \cap \overline{D}_2 \cap \overline{D}_3 \backslash (\{\text{intersections}\} \cup (x_2, y_2) \cup (x_3, y_3)),
\end{aligned}$$

For a point (x, y) in the sub-domain $\Gamma_1 = C_1 \backslash \{\overline{D}_2 \cup \overline{D}_3\}$ it holds:

$$f(x,y) = \sqrt{(x-x_2)^2 + (y-y_2)^2} - R_2 + \sqrt{(x-x_3)^2 + (y-y_3)^2} - R_3. \tag{4.9}$$

Let $\mathfrak{h}$ be the function defined on $\mathbb{R}^2$ by

$$\mathfrak{h}(x,y) = \sqrt{(x-x_2)^2 + (y-y_2)^2} - R_2 + \sqrt{(x-x_3)^2 + (y-y_3)^2} - R_3. \tag{4.10}$$

The functions f and $\mathfrak{h}$ differ on $\mathbb{R}^2$ but their restriction to Γ_1 coincide. Moreover, $\mathfrak{h}$ is differentiable on $\mathbb{R}^2 \backslash \{(x_2, y_2), (x_3, y_3)\}$. That means that if there exists a minimum value in the differentiable domain of function $\mathfrak{h}$ then it must be reached at a critical point. If this point belongs on the restricted path Γ_1 then it could be a candidate for a pseudo-intersection point.
As we are searching for possible critical points of function $\mathfrak{h}(x, y)$, we have to compute the derivative at points $P = (x, y)$ on the restricted path defined by our sub-domains. To do that we make use of the fact that whenever $\mathfrak{h}$ is a differentiable function of several variables and γ is a differentiable path, then

the univariate function g given by the composition $g : \mathfrak{h} \circ \gamma$ has a derivative given by

$$g'(\theta) = \langle \nabla \mathfrak{h}(\gamma(\theta)), \gamma'(\theta) \rangle,$$

where $\langle \cdot, \cdot \rangle$ denotes the inner product and ∇ the gradient.
Our first goal is to find an explicit formula for the derivative $g'(\theta)$. Because our restricted path is the circle circumference C_1 in order to simplify our computations and without loss of generality we can assume that our restricted path is the unit circle $\mathbb{T}$. This is just a change of coordinate system by using dilation and translation. Hence our γ path can be expressed as:

$$\gamma(\theta) = (\cos\theta, \sin\theta),$$

with $0 \leq \theta \leq 2\pi$. The derivative of $\gamma(\theta)$ is given by:

$$\gamma'(\theta) = (-\sin\theta, \cos\theta).$$

Since we work on the unit circle $\mathbb{T}$ it means that $\|\gamma'(\theta)\| = 1$.
The gradient of $\mathfrak{h}$ function $\nabla\mathfrak{h}(x, y)$ can be computed using the same logic as was used in order to compute Expressions (4.7) $\text{Expr}_j(x, y)|_\Delta$. As a result we end up once again with unit vector combinations $u_i(x, y)$ as in Equation (4.6), note that the direction of the unit vector depends on θ. Now the explicit expression of $g'(\theta)$ is

$$g'(\theta) = \frac{x_2 \sin\theta - y_2 \cos\theta}{\sqrt{(\cos\theta - x_2)^2 + (\sin\theta - y_2)^2}} + \frac{x_3 \sin\theta - y_3 \cos\theta}{\sqrt{(\cos\theta - x_3)^2 + (\sin\theta - y_3)^2}}.$$

Because it is difficult to solve $g'(\theta) = 0$ through the above equation, we will try to take advantage of the unit vectors relationships. This means that we will approach the problem through its geometric features.

Remark 18 *The derivatives of function g on each sub-domain Γ_1, Γ_2, Γ_3, Γ_4 are:*

$$\begin{cases} g'(\theta)|_{\Gamma_1} = \langle +u_2(\theta) + u_3(\theta), \gamma'(\theta) \rangle \\ g'(\theta)|_{\Gamma_2} = \langle -u_2(\theta) + u_3(\theta), \gamma'(\theta) \rangle \\ g'(\theta)|_{\Gamma_3} = \langle +u_2(\theta) - u_3(\theta), \gamma'(\theta) \rangle \\ g'(\theta)|_{\Gamma_4} = \langle -u_2(\theta) - u_3(\theta), \gamma'(\theta) \rangle. \end{cases} \tag{4.11}$$

Note that for simplicity of the notations we will write a unit vector as u_i instead of $u_i(\theta)$.

We can focus our study only on the expressions at the right side of Equations (4.11) and "forget" the sub-domains Γ_1, Γ_2, Γ_3, Γ_4. If for instance we find a point that satisfies $\langle +u_2 + u_3, \gamma'(\theta) \rangle = 0$ there are two possibilities: either it belongs to Γ_1 and it is an actual critical point, or it does not belong to Γ_1. In the latter case, including this point in our list makes no harm: when we

evaluate the $\|V(P)\|_1$ norm at all points of our list, it will just be discarded because the norm will obvisouly not be minimal there. For the first case in the above equations, we get:

$$\begin{aligned}
&\langle u_2 + u_3, \gamma'(\theta)\rangle = 0 \\
&\Rightarrow \langle u_2, \gamma'(\theta)\rangle = -\langle u_3, \gamma'(\theta)\rangle \\
&\Rightarrow \|u_2\|\|\gamma'(\theta)\|\cos(\phi) = -\|u_3\|\|\gamma'(\theta)\|\cos(\phi') \\
&\Rightarrow \cos(\phi) = -\cos(\phi'),
\end{aligned}$$

Where θ is the angle which defines our tangent point $\gamma(\theta) \in C_1$ and ϕ, ϕ' are the angles between the tangent vector v_τ and the unit vectors direction u_2 and u_3 respectively, as illustrated in Figure 4.9(a). The above expression tells us that the angles of the unit vectors have opposite cosines. If we fixed u_2 then there are only two directions where u_3 satisfies the condition of the opposite cosine. The solid red vector of Figure 4.9(b) (which correspond to the information from Figure 4.9(a)) and the dashed red vector of Figure 4.9(b). Note in Figure 4.9(b) that the complementary angle ρ formed by ϕ is equal to the angle $\phi' - \frac{\pi}{2}$.
At this point one can ask: is there a unique point which satisfies the condition $\langle u_2 + u_3, \gamma'(\theta)\rangle = 0$? The answer is no, since from Figure 4.9(b) we already have two possible directions that satisfy the equation $\cos(\phi) = -\cos(\phi')$. So what can we do in order to compute all of these points? Luckily for us, the angle ρ which is the complementary angle of ϕ and the fact that it has an equal angle with respect to the u_3 vector and the normal direction axis is linked with an ancient problem known as Alhazen problem in optics [41]. This problem covers the case of the solid red vector in Figure 4.9(b) so we can study the angle ρ instead of ϕ.

Alhazen points (study of solid red vector in Figure 4.9(b))

Problem 1 ***Alhazen problem in optics (2D version)*** *[41]*
Given a light source and a circular mirror, find the points on the mirror, if any, where the light will be reflected to the eye of an observer.

For us the locations of the light source and the observer correspond to the circles centers (x_2, y_2) and (x_3, y_3) respectively. The circular mirror is the circumference C_1. The idea now of solving the Alhazen problem is based on the law of reflection, which states that the angles of incident and reflection are equal. For us the angle of incident is denoted as ρ and the angle of reflection is the angle of $\phi' - \frac{\pi}{2}$, see Figure 4.9(b).
Let $u = \gamma(\theta) \in \mathbb{T}$ and $c_2 = x_2 + \mathrm{i}y_2$, $c_3 = x_3 + \mathrm{i}y_3$ be the circles centers expressed in complex form. In [41] they use the notation $\measuredangle(c_2, u, 0) = \measuredangle(0, u, c_3)$ where $\measuredangle(c, u, w)$ denotes the radians measure in $(-\pi, \pi)$ of the oriented angle with initial side $[u, c]$ and final side $[u, w]$. This equality condition is equivalent to the statement that the angles of incident and reflection are equal.

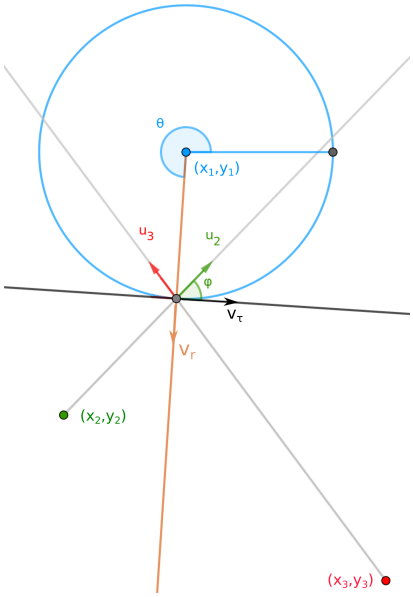

(a) This picture illustrates the unit vector projections of our example on the tangent point $\gamma(\theta) \in C_1$. At this point it holds that $\langle u_2 + u_3, \gamma'(\theta) \rangle = 0$. Based on the inner product properties we can associate the tangent axis with the cosine axis of the trigonometric circle as illustrated in the picture on the right.

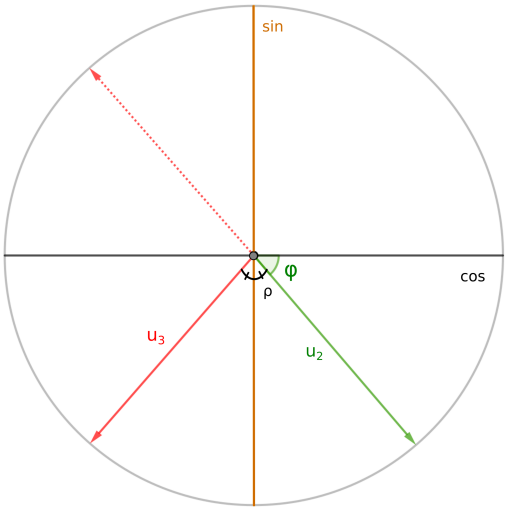

(b) This picture illustrates the information from the picture on the left. The point $\gamma(\theta) \in C_1$ is represented at the center of our unit circle $\mathbb{T}$. The horizontal black line is the tangent line of the left picture and is associated with the cosine axis of our unit circle $\mathbb{T}$. The vertical orange line is the line on the normal direction and is associated with the sine axis. There are two possible situations where $\langle u_2 + u_3, \gamma'(\theta) \rangle = 0$, our example in the left picture shows one of those and is illustrated with a solid red line.

Figure 4.9

In paper [41] they investigate the cases for all the possible locations of c_2, c_3 *e.g.* when both of them are inside the circle C_1. Finally they establish that:

$$\operatorname{Arg}\left(\frac{u - c_2}{u}\right) = \operatorname{Arg}\left(\frac{u}{u - c_3}\right).$$

From which we get:

$$\operatorname{Arg}\left(\frac{u - c_2}{u}\right) - \operatorname{Arg}\left(\frac{u}{u - c_3}\right) = 0 \Rightarrow \operatorname{Arg}\left(\frac{u - c_2}{u}\frac{u - c_3}{u}\right) = 0.$$

The trick now is to observe that since the argument of the quantity inside the parenthesis is equal to zero, it means that this quantity is a positive real

number, consequently it is equal with its conjugate

$$\frac{\overline{u}-\overline{c_2}}{\overline{u}}\frac{\overline{u}-\overline{c_3}}{\overline{u}}=\frac{u-c_2}{u}\frac{u-c_3}{u}. \tag{4.12}$$

By expanding the above equation and with the use of $u\overline{u}=1$ we get:

$$u^2\left(\frac{1}{u}-\overline{c_2}\right)\left(\frac{1}{u}-\overline{c_3}\right)=\frac{1}{u^2}(u-c_2)(u-c_3)$$
$$\Rightarrow u^2\left(\frac{1}{u^2}-\frac{1}{u}\overline{c_3}-\frac{1}{u}\overline{c_2}+\overline{c_2c_3}\right)=\frac{1}{u^2}(u^2-uc_3-uc_2+c_2c_3)$$

$$\Rightarrow \overline{c_2c_3}u^4-(\overline{c_2}+\overline{c_3})u^3+(c_2+c_3)u-c_2c_3=0. \tag{4.13}$$

This is a quartic equation, which has up to four complex roots. As they mention in [41] the solution of Equation (4.13) may have roots that are not on the unit circle. As remarked already earlier, having a finite number of extra points in our list does not affect our study: we will simply evaluate $\|V(P)\|_1$ for each one of them and eventually keep the minimum. The extra points will be discarded because they will obviously not provide a global minimum.

"Alhazen-like" points (study of dashed red vector in Figure 4.9(b))

Inspired by the solution of the Alhazen points, we study the dashed red vector of Figure 4.9(b) in a similar way. By using the same notation as before we can write:

$$\mathrm{Arg}\left(\frac{u-c_2}{u}\right)=\pi-\mathrm{Arg}\left(\frac{u}{u-c_3}\right).$$

From that we get

$$\mathrm{Arg}\left(\frac{u-c_2}{u}\right)+\mathrm{Arg}\left(\frac{u}{u-c_3}\right)=\pi\Rightarrow\mathrm{Arg}\left(\frac{u-c_2}{u}\frac{u}{u-c_3}\right)=\pi.$$

Observing that the argument of the quantity inside the parenthesis is equal to π, it means that this quantity is a negative real number, consequently it is equal with its conjugate

$$\frac{u-c_2}{u-c_3}=\frac{\overline{u}-\overline{c_2}}{\overline{u}-\overline{c_3}}$$

and by expanding the above equation in addition with the use of $u\overline{u}=1$ we get:

$$(\overline{c_2}-\overline{c_3})u^2+2\mathrm{iIm}(c_2\overline{c_3})u-c_2+c_3=0. \tag{4.14}$$

That means in order to solve our problem as illustrated in Figure 4.9(b) we have to solve Equations (4.13) and (4.14). The above analysis ensures that Alhazen and "Alhazen-like" points coincide with the points we are looking for, for the sub-domains Γ_1, Γ_4
In paper [42] they discuss and prove that Equation (4.12) is satisfied either if the incident and reflection angles are equal or if they differ by π. They call both kinds of points "reflection points" and distinguish them as "proper reflections" in the first case (which corresponds to the solid red vector of Figure 4.9(b)) and "backward reflections" in the second case. This is a convenient result for us, because in order to complete our analysis of the function f on non differentiable domains, we need to find also solutions for the cases where $\langle u_2 - u_3, \gamma'(\theta)\rangle = 0$. In these cases we get

$$\begin{aligned}
&\langle u_2, \gamma'(\theta)\rangle = \langle u_3, \gamma'(\theta)\rangle \\
&\Rightarrow \|u_2\|\|\gamma'(\theta)\| \cos(\phi) = \|u_3\|\|\gamma'(\theta)\| \cos(\phi') \\
&\Rightarrow \cos(\phi) = \cos(\phi').
\end{aligned}$$

In Figure 4.10 we illustrate the directions of the u_2 and u_3 vectors.

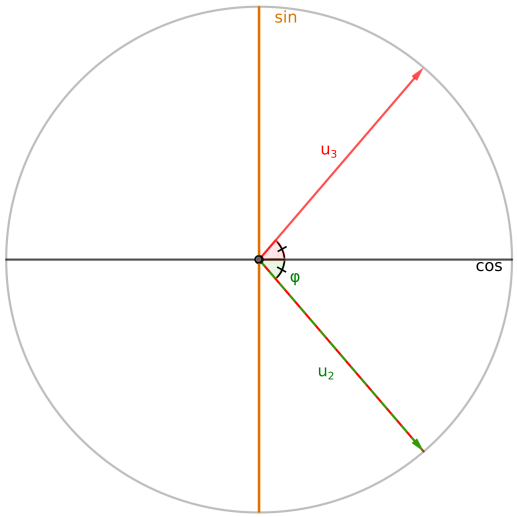

Figure 4.10: This picture illustrates the angle relation for the situations where $\cos(\phi) = \cos(\phi')$. Note that we preserve the color code of Figure 4.9b. There are two possible ways to have $\cos(\phi) = \cos(\phi')$ and we illustrate them with a solid and a dashed red line.

Now the information we get from Figure 4.10 can be decomposed into two problems. The first problem regarding the solid red vector of Figure 4.10. This problem is in fact the "backward reflections" of the Alhazen points which are described in [42], hence we can recover their solutions also from Equation (4.13).

The second problem regarding Figure 4.10 is the red dashed vector. This is equivalent to both the u_2 and u_3 vectors having exactly the same direction. By using the notations as before we can write:

$$\text{Arg}\left(\frac{u-c_2}{u}\right) = \text{Arg}\left(\frac{u-c_3}{u}\right) \Rightarrow \text{Arg}\left(\frac{u-c_2}{u-c_3}\right) = 0.$$

Now by observing that the argument of the quantity inside the parenthesis is equal to zero, means that the quantity is a positive real number, we can write

$$\frac{u-c_2}{u-c_3} = \frac{\overline{u}-\overline{c_2}}{\overline{u}-\overline{c_3}}.$$

This expression leads us to Equation (4.14). That means that the cases of Figure 4.10 have been already computed through Equations (4.13) and (4.14).
Now we have completed the list of points for the $\|V(P)\|_1$ minimization method. The list consists of the circles centers, the circles intersections, the two isogonic centers, the Alhazen and the "Alhazen-like" points. The next step in our analysis is to evaluate the quantity $\|V(P)\|_1$ for each one of these points and keep as pseudo-intersection point $\hat{\mathbf{x}}_d$ the point with the minimum $\|V(P)\|_1$ value.

4.2.3 Test of minimizing $\|V(P)\|_1$ simulations with synthetic data

Study of data without noise for the current lunometer configuration: for these experiments we use the same setup (Setup 1.3) with the 6000 dipoles as we did in the radical center analysis. These experiments concern ideal data from a single measurement position.
Here we compute the pseudo-intersection percentage error (e_{pi_ms}), based on the method that minimizes the sum of the distances to three given circles. This is computed with the same method as Equation (4.2), however we name it differently so we can distinguish the method results.

$$e_{pi\_ms} = \frac{|\hat{\mathbf{x}}_d - \mathbf{x}_d|}{R} \cdot 100.$$

The general results of our analysis are the following:

Experiment	Average e_{pi_ms} error	# of excluded cases	# of dipoles with error more than 1000%	# of dipoles with error more than 50%
Setup 1.3	27	0	2	914

For the 6000 dipoles the average e_{pi_ms} percentage error is 27%, with a median value of 13.5%. The distribution of e_{pi_ms} can be seen in Figure 4.11.

In fact 5086 cases have e_{pi_ms} percentage error less than 50% and we face only two cases with error more than 1000%. An illustration of the computed circles and the $\hat{\mathbf{x}}_d$ estimation from one of the examples with $e_{pi\_ms} > 1000\%$ can be seen in Figure 4.12. In fact a careful analysis of our experimental results shows that for e_{pi_ms} errors more than 200% we get circles configurations as seen in Figure 4.12. Note that the percentage of the error is linked with the size of the circles for this reason in Figure 4.12 small sized circles produce less error than bigger circles. We observe that the instability issues come from cases where the circle centers are almost aligned. This issue affects every method of our study.

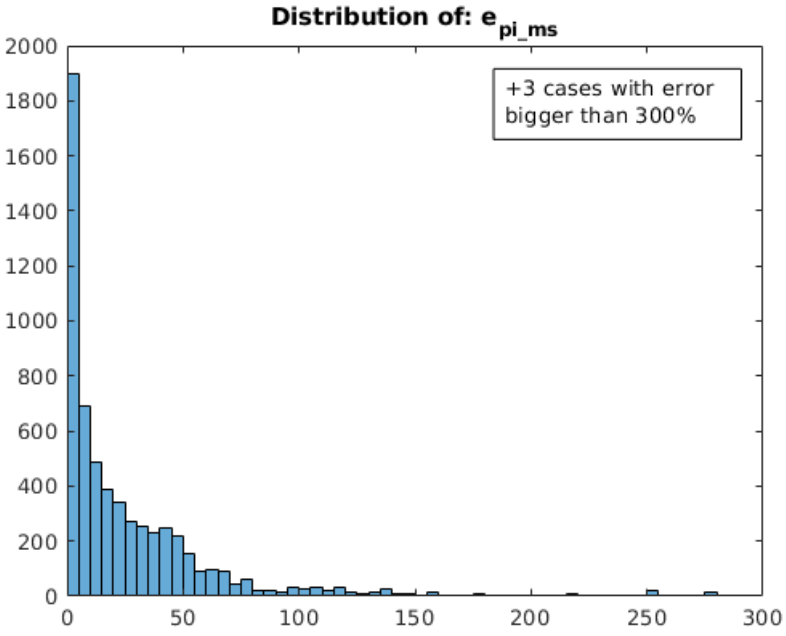

Figure 4.11: This picture illustrates the distribution of the e_{pi_ms} percentage error of the minimization of $\|V(P)\|_1$ method. Its vertical axis corresponds to the number of dipoles and its horizontal axis to the e_{pi_ms}. These experiments concern ideal data from a single measurement position.

The next question, since we use a list of points to search for the minimum value of $\|V(P)\|_1$, is how many times each category of points is selected as the minimum. At first sight the results may surprise the reader. Among the 6000 dipoles, there are 4169 occasions where an actual intersection point between two of the given circles is selected: that is almost 70% of the times. In addition, for the remaining 30% cases, the minimum is reached at an Alhazen or "Alhazen-like" point. That means that, in our list, the collections of circles centers and the two isogonic centers never correspond to a point that minimizes $\|V(P)\|_1$. This can be explained because our goal is

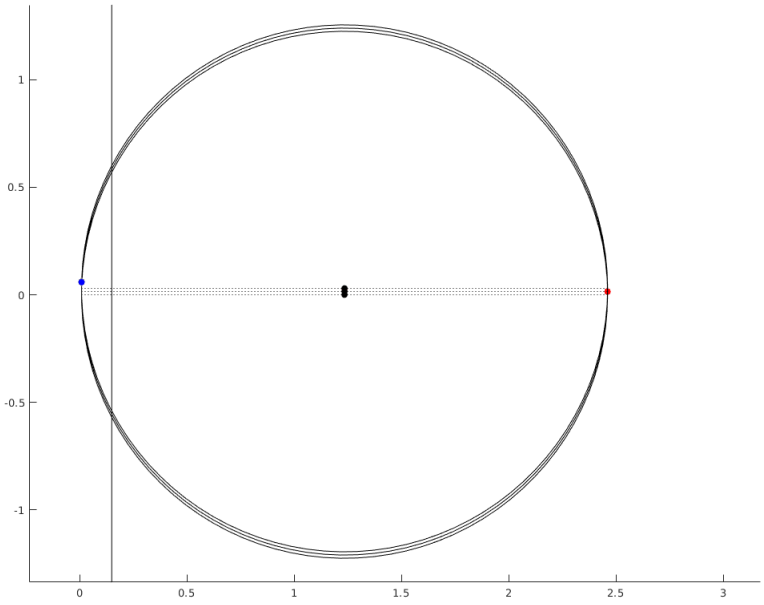

Figure 4.12: This picture illustrates one of the cases with $e_{pi\_ms} > 1000\%$. The recovered $\hat{\mathbf{x}}_d(p)$ is denoted as a red dot and the actual dipole location as a blue dot. The vertical black line corresponds to the sensors distance from the samples mass center $R = 0.015$. The horizontal dashed black lines indicate the circles diameters and at the same time the sensors heights h_i.

to minimize a problem with respect to the circumferences of the given circles and not with respect to the circles centers. In contrast circles centers and isogonic centers by construction "ignore" the information for the circles circumferences. By this analysis we can conclude that a feature of $\|V(P)\|_1$ minimization method is that its solutions tend to be located on the circles circumferences.
The approach used to minimize $\|V(P)\|_1$ heavily relies on the hypothesis that there are $S = 3$ circles and is hard to extend to more circles. As a result we cannot conduct simulations with more than three sensors. Our next method does not suffer from this problem.

4.3 Minimizing the sum of the squares of powers of a point with respect to given circles

Until now, we saw two different ways in order to estimate a pseudo-intersection point $\hat{\mathbf{x}}_d$ with the circles method. Both of those approaches work for three

given circles, a condition which is satisfied with the current lunometer's configuration. More precisely the radical center works by definition for $S = 3$ circles and the method of minimizing the sum of the distances to given circles, could be adapted for $S \geq 3$ circles, but the model is more complicated and the nice geometrical features with the unit vectors combinations may not hold anymore. For this reason in this section we use another method which minimizes the sum of the squares of the powers of a point with respect to $S \geq 3$ given circles. At the end of the section numerical simulations evaluate its performance.
To link this method with the previous ones, consider a point $P = (x, y) \in \mathbb{R}^2$ and given circles C_i, with $i = 1, .., S$. Recall from Definition 4 that the power of a point is given by:

$$h_i(x, y) = (x - x_i)^2 + (y - y_i)^2 - R_i^2.$$

Remark 19 *From Definition 4 we know that, if there exists an intersection point $P = (x, y) \in \mathbb{R}^2$ for $S \geq 3$ given circles then $h_1(x, y) = ... = h_S(x, y) = 0$ holds. If there is no intersection point then for $S = 3$ circles we can still search for $h_1(x, y) = h_2(x, y) = h_3(x, y) \neq 0$ which is the radical center. The idea now is instead of enforcing an equality among the powers $h_1(x, y) = ... = h_S(x, y)$ explore if we can find a point P with powers $h_i(x, y)$ as small as possible.*

Let us define the vector $\Lambda(P)$, for $S \geq 3$ given circles, by

$$\Lambda(P) = \begin{bmatrix} h_1(x, y) \\ h_2(x, y) \\ ... \\ h_S(x, y) \end{bmatrix} \in \mathbb{R}^N.$$

Our goal now is to find a point P which minimizes the $\|\Lambda(P)\|_2^2$ norm.

$$\|\Lambda(P)\|_2^2 = h_1^2(x, y) + ... + h_S^2(x, y) =: \sum_{i=1}^{S} k_i(x, y) =: k(x, y). \tag{4.15}$$

We actually want to minimize $\|\Lambda(P)\|_2$ rather than its square, but since it is a positive real number, minimizing it or its square is essentially the same problem: both $\|\Lambda(P)\|_2$ and $\|\Lambda(P)\|_2^2$ reach their minimum value at the same point $P = (x, y) \in \mathbb{R}^2$. The reason why we use $\|\Lambda(P)\|_2^2$ is because we want to simplify the square root which would otherwise be introduced in our computations from the Euclidean norm $\|\cdot\|_2$. In addition Expression (4.15) provides us with a continuous, differentiable function $k(x, y)$ in the entire plane $\mathbb{R}^2$. As before, because $k(x, y)$ increases when the point $P = (x, y)$ is

moving away from the given circles, we can restrict ourselves to a compact set which includes the global minimum, which must moreover be reached at a critical point of the function $k(x, y)$.
The critical points of function $k(x, y)$ are the points where its partial derivatives with respect to x and y vanish at the same time:

$$\begin{cases} A(x,y) := \frac{\partial k}{\partial x}(x,y) = 0 \\ \\ B(x,y) := \frac{\partial k}{\partial y}(x,y) = 0, \end{cases}$$

By computing the partial derivatives we get the following system:

$$\begin{cases} \frac{1}{4}\,A(x,y) = Sx^3 - 3\left(\sum_{i=1}^{S} x_i\right)x^2 + \left(3\sum_{i=1}^{S} x_i^2 + \sum_{i=1}^{S}\left((y-y_i)^2 - R_i^2\right)\right)x \\ \qquad\qquad - \sum_{i=1}^{S} x_i\left(x_i^2 + (y-y_i)^2 - R_i^2\right) = 0, \\ \frac{1}{4}\,B(x,y) = (Sy - \sum_{i=1}^{S} y_i)x^2 + \left(-2y\sum_{i=1}^{S} x_i + 2\sum_{i=1}^{S} x_i y_i\right)x \\ \qquad\qquad + y\sum_{i=1}^{S}\left(x_i^2 + (y-y_i)^2 - R_i^2\right) - \sum_{i=1}^{S} y_i\left(x_i^2 + (y-y_i)^2 - R_i^2\right) = 0. \end{cases} \tag{4.16}$$

At this point we have two options: either we continue our study with System (4.16) which leads us to quite complicated computations, or we compute a simpler system equivalent to System (4.16), by changing the coordinate system before the expansion of expressions $A(x, y)$ and $B(x, y)$. To do this simplification we take advantage from the fact that, in System (4.16), the quantities

$$\sum_{i=1}^{S} x_i,\ \sum_{i=1}^{S} y_i,\ \sum_{i=1}^{S} x_i y_i,$$

appear many times. We can eliminate those quantities by using a new coordinate system. The new coordinate system of our study is actually a translation and a rotation of the original one.
The translation we use is to place the origin of the coordinate system on the barycenter (gravity center) formed by the $S \geq 3$ circle centers. This corresponds to the following change of coordinates:

$$(x, y) \rightsquigarrow (x', y') = \left(x - \frac{1}{S}\sum_{i=1}^{S} x_i,\quad y - \frac{1}{S}\sum_{i=1}^{S} y_i\right).$$

By doing this we eliminate the terms $\sum_{i=1}^{S} x_i'$, $\sum_{i=1}^{S} y_i'$ in the Expression (4.16). Then we use rotation of angle $-\theta$ of the coordinate system such that:

$$(x', y') \rightsquigarrow (x'', y'') = (x'\cos(\theta) + y'\sin(\theta), -x'\sin(\theta) + y'\cos(\theta)).$$

In this case

$$\sum_{i=1}^{S} x_i'' y_i'' = \sum_{i=1}^{S} \left(x_i' \cos(\theta) + y_i' \sin(\theta)\right) \left(-x_i' \sin(\theta) + y_i' \cos(\theta)\right).$$

By expanding the above expression and with the use of trigonometric formulas we can express it as

$$\sum_{i=1}^{S} x_i'' y_i'' = \alpha \cdot \cos(\phi) + \beta \cdot \sin(\phi),$$

with $\alpha = \sum_{i=1}^{S} x_i' y_i'$, $\beta = \frac{1}{2} \sum_{i=1}^{S} \left(y_i'^2 - x_i'^2\right)$ and $\phi = 2\theta$.
What we want with the rotation of the coordinate system is

$$\alpha \cdot \cos(\phi) + \beta \cdot \sin(\phi) = 0.$$

We can compute now an angle for ϕ as follows

$$\alpha \cdot \cos(\phi) + \beta \cdot \sin(\phi) = 0 \Leftrightarrow \Re\left((\cos\phi + \mathrm{i}\sin\phi)(\alpha - \mathrm{i}\beta)\right) = 0 \Leftrightarrow$$
$$\Leftrightarrow \Re\left(e^{\mathrm{i}\phi}(\alpha - \mathrm{i}\beta)\right) = 0.$$

If $\alpha^2 + \beta^2 \neq 0$ then we can continue our computations as:

$$\Re\left(e^{\mathrm{i}\phi}|\alpha - \mathrm{i}\beta|e^{\mathrm{i}\mathrm{Arg}(\alpha - \mathrm{i}\beta)}\right) = 0 \Leftrightarrow$$
$$\Leftrightarrow \Re\left(e^{\mathrm{i}\phi}e^{\mathrm{i}\mathrm{Arg}(\alpha - \mathrm{i}\beta)}\right) = 0,$$

which gives us

$$\phi + \mathrm{Arg}(\alpha - \mathrm{i}\beta) = \tfrac{\pi}{2}[\pi] \Leftrightarrow$$
$$\Leftrightarrow \phi = \tfrac{\pi}{2} - \mathrm{Arg}(\alpha - \mathrm{i}\beta)[\pi].$$

Where $[\pi]$ denotes the modulo π. If $\alpha^2 + \beta^2 = 0$ then we can keep the coordinate system as it is (without rotation) because in that case any angle will satisfy our equations.
Without loss of generality, we will hence assume that we work from the beginning in such a coordinate system, so we further assume that $\sum_{i=1}^{S} x_i = 0$, $\sum_{i=1}^{S} y_i = 0$, $\sum_{i=1}^{S} x_i y_i = 0$.
To simplify the computation of our system even further we introduce the following notations:
$\mathcal{X} = \sum_{i=1}^{S} x_i^2$, $\mathcal{Y} = \sum_{i=1}^{S} y_i^2$, $\mathcal{R} = \sum_{i=1}^{S} R_i^2$, $\mathcal{C} = -\sum_{i=1}^{S} x_i(x_i^2 + y_i^2 - R_i^2)$, $\mathcal{D} = -\sum_{i=1}^{S} y_i(x_i^2 + y_i^2 - R_i^2)$, $\mathcal{M} = 3\mathcal{X} + \mathcal{Y} - \mathcal{R}$ and $\mathcal{W} = \mathcal{X} + 3\mathcal{Y} - \mathcal{R}$.

Once simplified using the properties of our system of coordinates and our notations, System (4.16) becomes:

$$\begin{cases} \mathcal{A}(x,y) = \mathcal{A}_y(x) = Sx^3 + (Sy^2 + \mathcal{M})x + \mathcal{C} = 0 \\ \mathcal{B}(x,y) = \mathcal{B}_y(x) = Syx^2 + Sy^3 + y\mathcal{W} + \mathcal{D} = 0. \end{cases} \tag{4.17}$$

Remark 20 *Observe that System* (4.17) *consists of two polynomials with variables* (x, y)*. Observe also that we adopt the notations* $\mathcal{A}_y(x)$ *and* $\mathcal{B}_y(x)$ *to underline the idea that we can consider these polynomials as univariate polynomials with variable* x *and an unknown parameter* y*. This is an important step in order to continue our analysis. That happens because we want to search for the common roots of our polynomials* $\mathcal{A}(x, y)$ *and* $\mathcal{B}(x, y)$ *by using the resultant method [43, ch.4 §8], however a fundamental condition of this method is that we have to deal with a system of two univariate polynomials, hence the* $\mathcal{A}_y(x)$ *and* $\mathcal{B}_y(x)$ *notations. A description of the resultant method and why we are able to use it follows in the next subsection.*

4.3.1 Resultant

Definition 7 ***Resultant***
Consider two polynomials with coefficients in $\mathbb{R}$*:*

$$L(x) = l_n x^n + ... + l_1 x + l_0,$$
$$Q(x) = q_m x^m + ... + q_1 x + q_0.$$

The resultant of L, Q *is defined as the determinant of the* $(m+n) \times (m+n)$ *Sylvester matrix given by*

$$\mathfrak{S}_{L,Q} = \begin{bmatrix} l_n & l_{n-1} & l_{n-2} & \dots & 0 & 0 & 0 \\ 0 & l_n & l_{n-1} & \dots & 0 & 0 & 0 \\ \vdots & \ddots & \ddots & & \ddots & \ddots & \vdots \\ 0 & 0 & 0 & \dots & l_1 & l_0 & 0 \\ 0 & 0 & 0 & \dots & l_2 & l_1 & l_0 \\ q_m & q_{m-1} & q_{m-2} & \dots & 0 & 0 & 0 \\ 0 & q_m & q_{m-1} & \dots & 0 & 0 & 0 \\ \vdots & \ddots & \ddots & & \ddots & \ddots & \vdots \\ 0 & 0 & 0 & \dots & q_1 & q_0 & 0 \\ 0 & 0 & 0 & \dots & q_2 & q_1 & q_0 \end{bmatrix} \tag{4.18}$$

Where the m *first rows contain the coefficients* l_n*,* l_{n-1}*, ... ,* l_0 *of* L *shifted 0, 1, ... ,* $m-1$ *steps and padded with zeros, and the* n *last rows contain the coefficients* q_m*,* q_{m-1}*, ... ,* q_0 *of* Q *shifted 0, 1, ... ,* $n-1$ *steps and padded with zeros.*

Proposition 3 *[43, ch.4 §8, Prop.8.1 p.202]*

If the polynomials $L(x)$, $Q(x)$ have a common root in $\mathbb{C}$, then their resultant is equal to zero.

Our strategy is as follows, first we compute the determinant of the Sylvester matrix for our univariate polynomials $\mathrm{Det}(\mathfrak{S}_{\mathcal{A}_y,\mathcal{B}_y})$. The computations of the determinant, will provide us with a polynomial of variable y. Then by computing the roots of that polynomial we have a collection of possible values of parameter y. We can then replace the parameter y in System (4.17) with each one of the computed values. Finally we solve $\mathcal{A}(x) = 0$ and $\mathcal{B}(x) = 0$ with respect to variable x and we have as solutions the pairs (x, y) with all the possible critical points of function $k(x, y)$. The last step is to bring those points back to the original geometry and keep the one that minimizes the $\|\Lambda(P)\|_2^2$.
More precisely our Sylvester's matrix has the form:

$$\mathfrak{S}_{\mathcal{A}_y,\mathcal{B}_y}=\begin{bmatrix} S & 0 & Sy^2+\mathcal{M} & \mathcal{C} & 0 \\ 0 & S & 0 & Sy^2+\mathcal{M} & \mathcal{C} \\ Sy & 0 & Sy^3+y\mathcal{W}+\mathcal{D} & 0 & 0 \\ 0 & Sy & 0 & Sy^3+y\mathcal{W}+\mathcal{D} & 0 \\ 0 & 0 & Sy & 0 & Sy^3+y\mathcal{W}+\mathcal{D} \end{bmatrix}. \tag{4.19}$$

By computing the determinant of the Matrix (4.19), we end up with a polynomial of degree 5 namely

$$\Omega(y) = \omega_5 y^5 + \omega_4 y^4 + \omega_3 y^3 + \omega_2 y^2 + \omega_1 y + \omega_0,$$

where $\Omega(y)$ is the resultant of $\mathcal{A}_y(x)$, $\mathcal{B}_y(x)$ and it has coefficients $\omega_j \in \mathbb{R}$, $j = 0, 1, ..., 5$

$$\begin{aligned} \omega_5 &= S^3(\mathcal{W}-\mathcal{M})^2, \\ \omega_4 &= 2\mathcal{D}S^3(\mathcal{W}-\mathcal{M}), \\ \omega_3 &= S^3(\mathcal{C}^2+\mathcal{D}^2) + S^2\mathcal{W}(\mathcal{M}-\mathcal{W})^2, \\ \omega_2 &= \mathcal{D}S^2(\mathcal{W}-\mathcal{M})(3\mathcal{W}-\mathcal{M}), \\ \omega_1 &= \mathcal{D}^2S^2(3\mathcal{W}-2\mathcal{M}), \\ \omega_0 &= S^2\mathcal{D}^3. \end{aligned}$$

Note that in general for polynomials of fifth degree or higher we can calculate their roots with numerical approximations from root-finding algorithms *e.g.* Newton-Raphson method [44].
If $(x^\star, y^\star)$ is a common root of System (4.17), Proposition 3 ensures that $\Omega(y^\star) = 0$. Therefore, we compute the real roots of $\Omega(y) = 0$ (among which we are sure to find $y^\star$), and we plug each one of them back in the equations $\mathcal{A}_y(x) = 0$, $\mathcal{B}_y(x) = 0$ (now the equations can be written as $\mathcal{A}(x) = 0$, $\mathcal{B}(x) = 0$ because y is given). System (4.17) becomes a system of polynomials in the x variable only. In the case when we put the proper value $y^\star$, this system must have at least one real root (namely $x^\star$). In total we can have up to 25 (x, y) pairs (with one of the pairs having the same $(x^\star, y^\star)$ values).

That happens because the polynomial $\Omega(y)$ might have up to 5 real roots, and then for polynomials $\mathcal{A}(x) = 0$ and $\mathcal{B}(x) = 0$ we have up to 3 and up to 2 roots respectively. The last step is to bring the recovered $(x^\star, y^\star)$ pair back to the original coordinate system and evaluate the function $k(x, y)$. We keep as pseudo-intersection $\hat{\mathbf{x}}_{d(p)}$ point the (x, y) pair that minimizes $\|\Lambda(P)\|_2^2$. The idea of how we compute the pseudo-intersection candidates can be seen in Algorithm 3.

In Algorithm 3, notice that we make use of a function called real_roots which is assumed to be a library function that returns all the real roots of a polynomial whose variable name is given as the second input.

Algorithm 3 Minimize the sum of the squares of the powers of a point w.r.t. S circles

Function: MinPowers
Input: (x_1, y_1), ..., (x_S, y_S) a list of S circle centers; $R_1, \ldots, R_S$, their radii.
Output: $(x^\star, y^\star)$ the point of $\mathbb{R}^2$ that minimizes the criterion k, see Eq. (4.15).

$x_{\text{avg}} \longleftarrow \frac{1}{S}\sum_{j=1}^{S} x_j\,;\qquad y_{\text{avg}} \longleftarrow \frac{1}{S}\sum_{j=1}^{S} y_j$
$\alpha \longleftarrow \sum_{j=1}^{S} x_j y_j\,;\quad \beta \longleftarrow \frac{1}{2}\sum_{j=1}^{S}\left(y_j^2 - x_j^2\right)$
/* Translate the system of coordinates if necessary */
if $x_{\text{avg}}^2 + y_{\text{avg}}^2 \neq 0$ **then**
  for $j = 1$ to S **do**
    $x'_j \longleftarrow x_j - x_{\text{avg}}\,;\quad y'_j \longleftarrow y_j - y_{\text{avg}}$
  end for
  $(x^\star, y^\star) \longleftarrow \text{MinPowers}((x'_1, y'_1), \ldots, (x'_S, y'_S), R_1, \ldots, R_S)$
  return $(x^\star + x_{\text{avg}},\, y^\star + y_{\text{avg}})$
end if
/* Rotate the system of coordinates if necessary */
if $\alpha^2 + \beta^2 \neq 0$ **then**
  $\phi \longleftarrow \frac{\pi}{2} - \text{Arg}(\alpha - \mathrm{i}\beta)\,;\quad \theta \longleftarrow \frac{\phi}{2}$
  for $j = 1$ to S **do**
    $x''_j \longleftarrow x_j\cos(\theta) + y_j\sin(\theta)\,;\quad y''_j \longleftarrow -x_j\sin(\theta) + y_j\cos(\theta)$
  end for
  $(x^\star, y^\star) \longleftarrow \text{MinPowers}((x''_1, y''_1), \ldots, (x''_S, y''_S), R_1, \ldots, R_S)$
  return $(x^\star\cos(\theta) - y^\star\sin(\theta),\, x^\star\sin(\theta) + y^\star\cos(\theta))$
end if
/* Otherwise, we are in a normalized system of coordinates */
$\mathcal{X} \longleftarrow \sum_{j=1}^{S} x_j^2\,;\quad \mathcal{Y} \longleftarrow \sum_{j=1}^{S} y_j^2\,;\quad \mathcal{R} \longleftarrow \sum_{j=1}^{S} R_j^2$
$\mathcal{C} \longleftarrow -\sum_{j=1}^{S} x_j(x_j^2 + y_j^2 - R_j^2)\,;\quad \mathcal{D} \longleftarrow -\sum_{j=1}^{S} y_j(x_j^2 + y_j^2 - R_j^2)$
$\mathcal{M} \longleftarrow 3\mathcal{X} + \mathcal{Y} - \mathcal{R}\,;\quad \mathcal{W} \longleftarrow \mathcal{X} + 3\mathcal{Y} - \mathcal{R}$
/* Coefficients of $\Omega(y)$, the determinant of $\mathfrak{S}_{\mathcal{A}_y,\mathcal{B}_y}$, see Eq. (4.19) */
$\omega_5 \longleftarrow S^3(\mathcal{W} - \mathcal{M})^2\,;\quad \omega_4 \longleftarrow 2\mathcal{D}S^3(\mathcal{W} - \mathcal{M})$
$\omega_3 \longleftarrow S^3(\mathcal{C}^2 + \mathcal{D}^2) + S^2\mathcal{W}(\mathcal{M} - \mathcal{W})^2\,;\quad \omega_2 \longleftarrow \mathcal{D}S^2(\mathcal{W} - \mathcal{M})(3\mathcal{W} - \mathcal{M})$

$\omega_1 \longleftarrow \mathcal{D}^2S^2(3\mathcal{W} - 2\mathcal{M})\,;\quad \omega_0 \longleftarrow S^2\mathcal{D}^3$
$L \longleftarrow \text{realRoots}(\omega_5 y^5 + \omega_4 y^4 + \omega_3 y^3 + \omega_2 y^2 + \omega_1 y + \omega_0, y)$
minValue $= +\infty$
for $y^\star$ **in** L **do**
  for $x^\star$ **in** realRoots$(Sx^3 + (Sy^{\star 2} + \mathcal{M})x + \mathcal{C}, x)$ **do**
    $k \longleftarrow \sum_{j=1}^{S}\left((x^\star - x_j)^2 + (x^\star - x_j)^2 - R_j^2\right)^2$
    if $k \leq$ minValue **then**
      minValue $\longleftarrow k\,;\quad$ res $\longleftarrow (x^\star,\, y^\star)$
    end if
  end for
end for
return res

4.3.2 Test of minimizing $\|\Lambda(P)\|_2^2$ method, simulations with synthetic data

Study of data without noise for the current lunometer configuration: we use the same setup of experiments with the 6000 dipoles that are located on concentric cylinders, as we did in the radical center and the minimization of $\|V(P)\|_1$ methods analysis (Setup 1.3). Once again we compute the pseudo-intersection percentage error which for this method we call it e_{pi_pw}. This is computed in the same way as Equation (4.2).

$$e_{pi\_pw} = \frac{|\hat{\mathbf{x}}_d - \mathbf{x}_d|}{R} \cdot 100.$$

The general results of our analysis are as follows:

Experiment	Average e_{pi_pw} error	# of excluded cases	# of dipoles with error more than 1000%	# of dipoles with error more than 50%
Setup 1.3	34	0	26	951

For the 6000 dipoles the averaged e_{pi_pw} error is 34% with a median value at 14.4%, which are slightly bigger than the average e_{pi_ms} which we compute for the minimization of $\|V(P)\|_1$. We can see the error distribution of e_{pi_pw} in Figure 4.13. Here we face 26 cases with $e_{pi\_pw} > 1000\%$. These cases correspond to circles whose centers are almost aligned. It is worth mentioning that e_{pi_pw} and e_{pi_ms} error distributions are almost identical. The only difference is for the number of dipoles with an error larger than 300%. This difference could be the effect of the $\|V(P)\|_1$ feature which tends to select an intersection point or a point on the circumference as a pseudo-intersection point, in contrast to the $\|\Lambda(P)\|_2^2$ method.

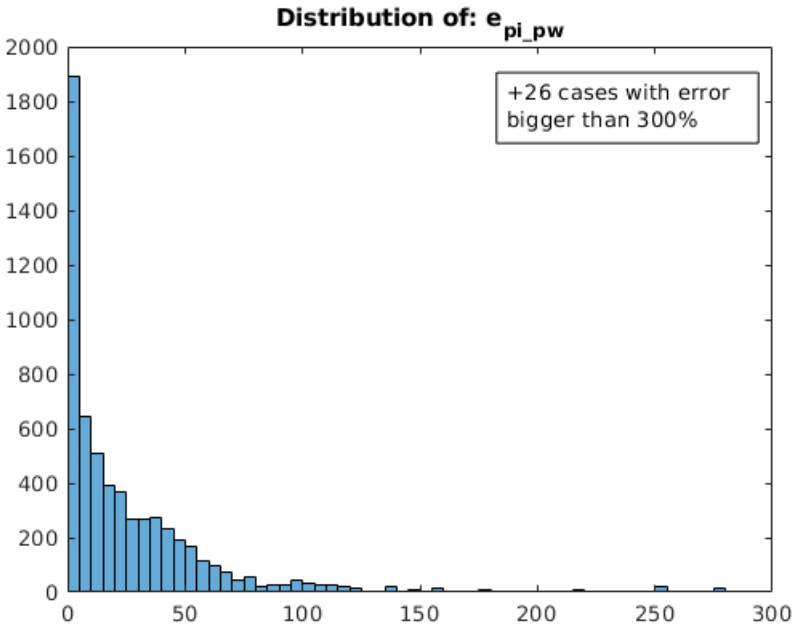

Figure 4.13: This picture illustrates the e_{pi_pw} distribution for ideal data from a single measurement position. Its vertical axis corresponds to the number of dipoles and its horizontal axis to the e_{pi_pw} percentage error. For these experiments we use the $\|\Lambda(P)\|_2^2$ method with data acquired from 3 sensors.

Study of data without noise for multiple sensors: as we have already discussed, the extra feature of this method is that it can be used with more than three sensors, offering the possibility of also using the circles method. So it is natural to conduct some experiments with multiple sensors even if we can not compare them directly with the minimization of $\|V(P)\|_1$ process. For the multiple sensor experiments we use the Setup 1.4 as described in Chapter 1 which concern measurements form a single measurement position for ideal data. Here we have 6000 dipoles on concentric cylinders as before, but we use 11 sensors instead of 3.

The general results of our analysis are as follows:

Experiment	Average e_{pi_pw} error	# of excluded cases	# of dipoles with error more than 1000%	# of dipoles with error more than 50%
Setup 1.4	8.4	0	0	148

Note that (once again) we do not compute 3 cases because of the averaged planes results and the fact that we have $\text{Arg}\hat{\xi}'_{(i)-}$ angles with ranges of more than 90°. The first observation (regarding the remaining dipoles) for the

experiments without noise for multiple sensors is that the e_{pi_pw} average error drops to 8.4%. In fact the maximum e_{pi_pw} error does not exceed 96% and only 3% of the dipoles locations produce an error bigger than 50%. The results are significantly better compared to the experiments with the actual lunometer configuration. The evidence that more sensors provide us with better results has already been seen in Chapter 3. This result is one more confirmation of this observation. The error distribution of e_{pi_pw} error for the multiple sensors experiment can be seen in Figure 4.14.

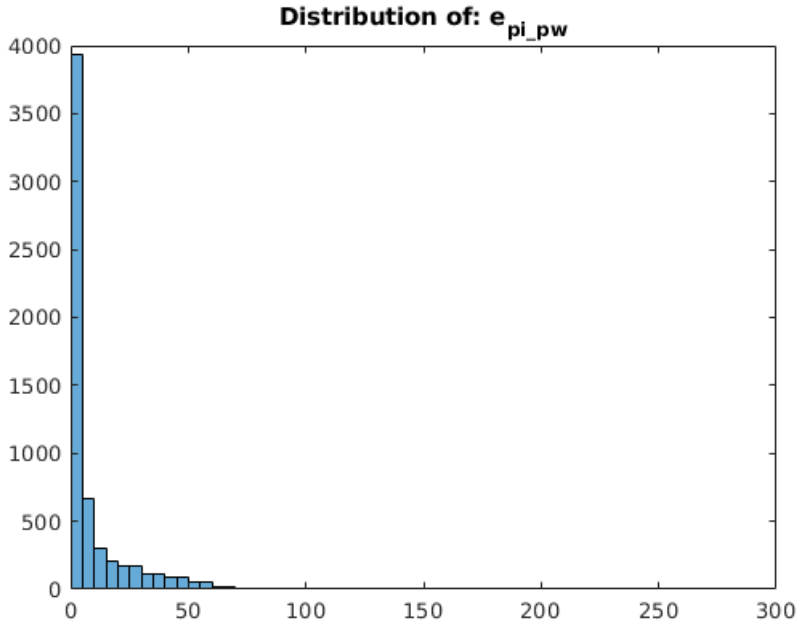

Figure 4.14: This picture illustrates the e_{pi_pw} error distribution for multiple sensors for ideal data. Its vertical axis corresponds to the number of dipoles and its horizontal axis to the e_{pi_pw} percentage error. Note that the maximum error is 95.2%, the illustration exceeds up to 300% in order to be compareable with Figure 4.13. For these experiments we use also the $\|\Lambda(P)\|_2^2$ method.

4.3.3 Summary of our technique

In Chapter 2 we saw the PHC and the grid method for finding a first estimate of the $\xi'_{(i)-}$ pole. We optimized their results with RARL2 and we finally get the $\hat{\xi}'_{(i)-}$ estimation.
In Chapter 3 we studied different methods to gain knowledge of the dipole location $\mathbf{X}_d$. Each method has its own characteristics. We also introduced the circles method but we faced the issue of defining a pseudo-intersection

point $\hat{\mathbf{x}}_d$.
Finally in Chapter 4 we described three techniques for which the circles method can define a pseudo-intersection point $\hat{\mathbf{x}}_d$.
By conducting experiments and comparing their results we decided that the methodology we will use to approach the problem of finding the dipole localization $\mathbf{X}_d$ is the following:

- Use of the grid method and RARL2 to find the $\hat{\xi}'_{(i)-}$ estimations.
- Use of the planes method in order to define the averaged plane, (for cases with range bigger than 90° we disregard the information of the whole position).
- Use of the circles method with the minimization of $\|\Lambda(P)\|_2^2$ in order to define a pseudo-intersection point $\hat{\mathbf{x}}_d$.
- Combine the information of planes and circles method in order to define the $\hat{\mathbf{X}}_d(p)$ per measurement position $p = 1, 2, 3$.

Because the circles method provides us with one estimation $\hat{\mathbf{X}}_d(p)$ per measurement position, we have to decide how we will compute a single $\hat{\mathbf{X}}_d$ estimation by combining all the available information. For this reason we use the centroid approach as follows.

4.4 Centroid

Depending on the data availability we face one of the following cases.

Data available from a single measurement position $p = 1$: in that case

$$\hat{\mathbf{X}}_d(1) =: \hat{\mathbf{X}}_d.$$

Data available from two measurement positions $p = 1, 2$: let us assume that two positions $p = 1, 2$ provide us with two independent estimates $\hat{\mathbf{X}}_d(1)$ and $\hat{\mathbf{X}}_d(2)$. In that case we compute the midpoint

$$\frac{\hat{\mathbf{X}}_d(1) + \hat{\mathbf{X}}_d(2)}{2} =: \hat{\mathbf{X}}_d,$$

as the final dipole location estimation $\hat{\mathbf{X}}_d$.

Data available from three measurement positions $p = 1, 2, 3$**:** similarly with the previous case, if we have independent estimates from all three measurement positions, our final dipole location estimation $\hat{\mathbf{X}}_d$ is given by computing the centroid of the three points $\hat{\mathbf{X}}_d(1)$, $\hat{\mathbf{X}}_d(2)$ and $\hat{\mathbf{X}}_d(3)$ as follows:

$$\frac{\hat{\mathbf{X}}_d(1) + \hat{\mathbf{X}}_d(2) + \hat{\mathbf{X}}_d(3)}{3} =: \hat{\mathbf{X}}_d.$$

4.5 Rough approximation

At this point it is useful to recall the method we use (at the first stages of our study [20]) before we compute the pseudo-intersection points and their centroid. This method consist of a rough approximation and it is an independent method for estimating the dipole location $\mathbf{X}_d$.
Rough approximation is a basic technique which needs information from all three measurement positions in order to compute the $\hat{\mathbf{X}}_d$ estimation. Its idea is based on the properties of the pole ξ'_- which we studied in Chapter 2 and the fact that $|\xi'_-| \leq |\xi'_d|$. From the first measurement position, we have several $\hat{\xi'}_{(i)-}$ estimations (as many as sensors), from those we keep the one with maximum modulus, thereby we obtain a rough approximation of $(\hat{x}_d, \hat{y}_d)$ coordinates.
Repeating the same procedure with the $\hat{\xi'}_{(i)-}$ corresponding to the second and third measurement positions, we get a rough approximation of $(\hat{y}_d, \hat{z}_d)$ and $(\hat{x}_d, \hat{z}_d)$ respectively. Overall, we have two estimates for each of the three coordinates of $\mathbf{X}_d$ dipole. Now for each coordinate, we retain the estimate of maximum absolute value.

Once we have an estimation $\hat{\mathbf{X}}_d$ for our dipole location, the only unknown quantity remaining in our main Equation (1.8) is $\mathbf{M}_d$. The next chapter is dedicated to its recovery.

CHAPTER 5

Moment recovery and numerical experiments

In this chapter, we are interested in recovering the magnetization $\mathbf{M}_d$ of the dipole. The key observation is that, when the dipole location $\mathbf{X}_d$ is estimated, the unknown quantity $\mathbf{M}_d$ can be recovered by studying the numerator of our main Equation (1.8).

$$\mathbf{B}_{[\mathbf{X}_d,\mathbf{M}_d]}(\mathbf{X}) = -\frac{\mu_0}{4\pi}\,\frac{|\mathbf{X}-\mathbf{X}_d|^2\,\mathbf{M}_d - 3\,[\mathbf{M}_d\cdot(\mathbf{X}-\mathbf{X}_d)]\,(\mathbf{X}-\mathbf{X}_d)}{|\mathbf{X}-\mathbf{X}_d|^5}\,.$$

The idea now is to create and solve a linear system of equations with unknown quantity the moment

$$\mathbf{M}_d = \begin{pmatrix} M_1 \\ M_2 \\ M_3 \end{pmatrix}$$

of the dipole.
What we measure are the magnetic field components (radial, tangential or vertical) $\mathbf{B}_{[\mathbf{X}_d,\mathbf{M}_d]}(\mathbf{X})$ at points $\mathbf{X} = \mathbf{X}_{ji} = (x_j, y_j, z_i)$. In our simulations we use $j = 1, \cdots, N$ with $N = 360$ the number of measurement points and $i = 1, \cdots, S$ with $S = 3$ or 11 the number of sensors (which for the current lunometer configuration corresponds to measurements of the three components of the magnetic field measured at different heights). Based on these conventions, (x_j, y_j) belongs to a circle of pointwise measurements of any component of the field, while z_i has the value of one of the heights of the measurements circles.
When the dipole location $\mathbf{X}_d$ is estimated, the denominator in Equation (1.8) can be considered as a known quantity. Consequently, we can rewrite Equation (1.8) as

$$-\frac{4\pi}{\mu_0}|\mathbf{X}-\mathbf{X}_d|^5\mathbf{B}_{[\mathbf{X}_d,\mathbf{M}_d]}(\mathbf{X}) = |\mathbf{X}-\mathbf{X}_d|^2\,\mathbf{M}_d - 3\,[\mathbf{M}_d\cdot(\mathbf{X}-\mathbf{X}_d)]\,(\mathbf{X}-\mathbf{X}_d)\,,$$

and set

$$\mathbf{F}_i(\mathbf{X}_{ji}) = -\frac{4\pi}{\mu_0}|\mathbf{X}_{ji} - \mathbf{X}_d|^5 \mathbf{B}_{[\mathbf{X}_d, \mathbf{M}_d]}(\mathbf{X}_{ji})\,.$$

Were $i = 1, ..., S$ indicates measurements from the i^{th} sensor (measurements of a single magnetic field component) at the corresponding height z_i. Note that $\mathbf{F}_i(\mathbf{X}_{ji})$ is a vector of size $N \times 1$. Now for a single measurement component we can write:

$$\mathbf{F}_i = |\mathbf{X}_{ji} - \mathbf{X}_d|^2 \begin{bmatrix} M_1 \\ M_2 \\ M_3 \end{bmatrix} - 3 \left(\begin{bmatrix} M_1 \\ M_2 \\ M_3 \end{bmatrix} \cdot \begin{bmatrix} x_j - x_d \\ y_j - y_d \\ z_i - z_d \end{bmatrix} \right) \begin{bmatrix} x_j - x_d \\ y_j - y_d \\ z_i - z_d \end{bmatrix}. \tag{5.1}$$

Let us assume that $S = 3$, and we have measurements for the radial, tangential and vertical component of the magnetic field respectively. In that case we can expand Equation (5.1) as follows:

$$\begin{cases} \mathbf{F}_1 = \left(|\mathbf{X}_{j1} - \mathbf{X}_d|^2 - 3(x_j - x_d)^2\right) M_1 - 3(x_j - x_d)(y_j - y_d) M_2 - 3(x_j - x_d)(z_1 - z_d) M_3 \\ \mathbf{F}_2 = -3(x_j - x_d)(y_j - y_d) M_1 + \left(|\mathbf{X}_{j2} - \mathbf{X}_d|^2 - 3(y_j - y_d)^2\right) M_2 - 3(y_j - y_d)(z_2 - z_d) M_3 \\ \mathbf{F}_3 = -3(x_j - x_d)(z_3 - z_d) M_1 - 3(y_j - y_d)(z_3 - z_d) M_2 + \left(|\mathbf{X}_{j3} - \mathbf{X}_d|^2 - 3(z_3 - z_d)^2\right) M_3. \end{cases} \tag{5.2}$$

Note that each $\mathbf{F}_i$ (in our example $i = 1, 2, 3$ for different components) is a system of linear equations with the unknowns (M_1, M_2, M_3). Since $j = 1, ..., 360$ means that each $\mathbf{F}_i$ is in fact an overdetermined system of linear equations. When we face overdetermined systems we can approximate their solution by using the least square approach, with the use of Moore-Penrose pseudo-inverse matrix as we did in Chapter 3 for the linear combination method in Section 3.3 and the parabola method in Section 3.4.

5.1 Moment recovery

In our example, in order to solve the linear system of Expression (5.2) we write it in a matrix form as follows:

$$\mathbf{F} = \mathbf{A}\mathbf{M}_d,$$

with:

$$\mathbf{F} = \begin{bmatrix} \mathbf{F}_1 \\ \mathbf{F}_2 \\ \mathbf{F}_3 \end{bmatrix},$$

$$\mathbf{A} = \begin{bmatrix} |\mathbf{X}_{j1} - \mathbf{X}_d|^2 - 3(x_j - x_d)^2 & -3(x_j - x_d)(y_j - y_d) & -3(x_j - x_d)(z_1 - z_d) \\ -3(x_j - x_d)(y_j - y_d) & |\mathbf{X}_{j2} - \mathbf{X}_d|^2 - 3(y_j - y_d)^2 & -3(y_j - y_d)(z_2 - z_d) \\ -3(x_j - x_d)(z_3 - z_d) & -3(y_j - y_d)(z_3 - z_d) & |\mathbf{X}_{j3} - \mathbf{X}_d|^2 - 3(z_3 - z_d)^2 \end{bmatrix}$$

and

$$\mathbf{M}_d = \begin{bmatrix} M_1 \\ M_2 \\ M_3 \end{bmatrix}.$$

The size of vector $\mathbf{F}$ is 1080×1, because we take measurements for $S = 3$ sensors at $N = 360$ different points for each one, hence $(3 \cdot 360 = 1080)$. The size of the matrix $\mathbf{A}$ is 1080×3 and the size of vector $\mathbf{M_d}$ is 3×1. Now we can use the Moore-Penrose pseudo-inverse [37] matrix $A^+ = (A^T A)^{-1} A^T$ (where A^T is the transposed matrix of A). The solution to the least squares problem is then given by

$$\hat{\mathbf{M}}_d = \mathbf{A}^+ \mathbf{F}.$$

Note that in [37] they explain that Moore-Penrose pseudo-inverse works even with rank deficient matrices.
This is how we compute the estimation $\hat{\mathbf{M}}_d$ for the moment of the dipole. From this estimation we can study two characteristics regarding the dipole's moment, namely its amplitude and its direction. For the numerical simulations that follows we compute the percentage amplitude error of the moment e_{ampl} as:

$$e_{ampl} = \left| \frac{|\hat{\mathbf{M}}_d| - |\mathbf{M}_d|}{|\mathbf{M}_d|} \right| \cdot 100.$$

The angular error e_{ang} of the moment (expressed in degrees) as:

$$e_{ang} = \left(\frac{\hat{\mathbf{M}}_d \cdot \mathbf{M}_d}{|\hat{\mathbf{M}}_d||\mathbf{M}_d|} \right) \cdot \frac{180}{\pi}.$$

We also compute the percentage error between the estimated and the actual dipole location $e_{est-act}$, normalized by the radius R of our sensors distance from the revolution axis. The $e_{est-act}$ is given by:

$$e_{est-act} = \frac{|\hat{\mathbf{X}}_d - \mathbf{X}_d|}{R} \cdot 100.$$

5.2 Numerical experiments with synthetic data

In this section we conduct numerical experiments for ideal and noisy data. For our synthetic data experiments we use $N = 360$ measurement points. In our analysis we compare 3 methods that compute an estimation for the dipole moment $\mathbf{M_d}$. These methods are the following.

- **Cerege method:** This method is the one that is currently used by geoscientists in Cerege. Its idea is to assume that the dipole is located at the origin of our coordinate system $\hat{\mathbf{X}}_d = (0, 0, 0)$.

- **Rough method:** This is the approximation method described in Chapter 4, Section 4.5 and the one we use in paper [20]. Here the idea is to keep the maximum modulus of the estimated pole $\hat{\xi}_{(i)-}$ per position and combine their information in order to recover a $\hat{\mathbf{X}}_d$. Note that for the current lunometer configuration we have $i = 1, 2, 3$ at different heights z_i.

- **Circles method:** This is the method we start studding in Chapter 3 Section 3.5 and we complete its study by finding a pseudo-intersection point in Chapter 4. For this method depending on the available information, we use the recovered point, midpoint or centroid as the estimation $\hat{\mathbf{X}}_d$ as described in Chapter 4 in the Section 4.4.

After estimating the dipole location $\hat{\mathbf{X}}_d$, we solve the appropriate linear system in order to recover the moment and get $\hat{\mathbf{M}}_d$, as explained in Section 5.1.

Remark 21 *An important piece of information for the reader is that, for the numerical experiments of this chapter, we do not discuss the linear combination method neither the parabola method. That happens because we test them and their results behave poorly when compared with the Cerege, rough and circles methods. We also present only synthetic data experiments because we still need some adaptations to our code in order to interpret and work with the real data measurements.*

In this section, with each experiment we investigate the influence of different factors. In Section 5.2.1 we conduct some experiments that we use as reference examples. These experiments concern ideal data from 3 different positions with the current lunometer configuration (3 sensors that measure the radial, tangential and vertical component of the field at different heights). In Section 5.2.2 we study the influence of using more sensors for ideal data. In Sections 5.2.3 and 5.2.4 we study the previous experiments under the contamination of noise. In these experiments we use 5% uniform noise on the signal and we study it without applying any denoising treatment. In Section 5.2.5 we use ideal data to test the influence of the moment orientation, we also test how the number of measurement positions affect our results and if less measurement points with $N = 72$, 63 or 24 can affect our estimations. The experiments of Section 5.2.5 can be compared with our reference results of Section 5.2.1. We continue with Section 5.2.5 by conducting experiments with noise data and multiple sensors for one measurement position. Finally we investigate in Section 5.2.6 if we can filter out specific estimations of $\hat{\xi}_{(i)-}$ pole estimations, instead of disregarding the measurements from the whole measurement position.

Remark 22 *As a general rule in our experiments, when we contaminate our data with noise (5% uniform noise on the signal) we continue our study*

without applying any denoising treatment. For this reason in the numerical experiments below when we mention that we use noisy data it implies that we do not use any treatment on them.

5.2.1 Study of data without noise for the current lunometer configuration

For this Setup 1.6 of experiments we use the lunometer configuration. Here we generate 6000 dipoles inside a ball and we take measurements from 3 positions. In Figure 5.1 one can see the distributions of the $e_{est-act}$, e_{ampl} and e_{ang} errors. We collect the results of our analysis in the following table:

# cases	$e_{est-act} > 20\%$	$e_{ampl} > 50\%$	$e_{ang} > 50^\circ$	$e_{ampl} < 25\%$	$e_{ang} < 10^\circ$
Cerege	5950	1925	1708	2894	1627
Rough	31	0	0	5940	5999
Circles	1120	698	2	4728	5964

Note that in these experiments we compute an $\hat{\mathbf{X}}_d$ at any case, because we use the methodology which is described in Chapter 4 Section 4.4. Hence we can compute a final $\hat{\mathbf{X}}_d$ point even if we disregard information from up to 2 (of the 3) measurement positions. This holds for all the experiments that follow and have measurements from 3 positions.

The first observation from these experiments is that the rough method performs perfectly for ideal data. This can be observed also from the distributions of $e_{est-act}$, e_{ampl} and e_{ang} errors in Figure 5.1 and it is in accordance with our results in paper [20]. Another (counterintuitive) observation is that the location of the dipole affects the estimation of the moment but not significantly. See for instance the case, $e_{est-act} > 20\%$ for the Cerege method. There are 5950 dipoles with localization error bigger than 20%, which corresponds to the 99% of the total cases. However only 32% of our dipoles provide $e_{ampl} > 50\%$ and 28% of them provide $e_{ang} > 50^\circ$. Finally, from the distributions of Figure 5.1 there is an evidence that for ideal data rough and circles method can estimate better the direction of the magnetic moment than its amplitude.

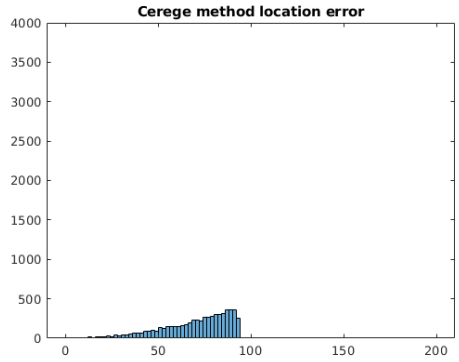

(a)

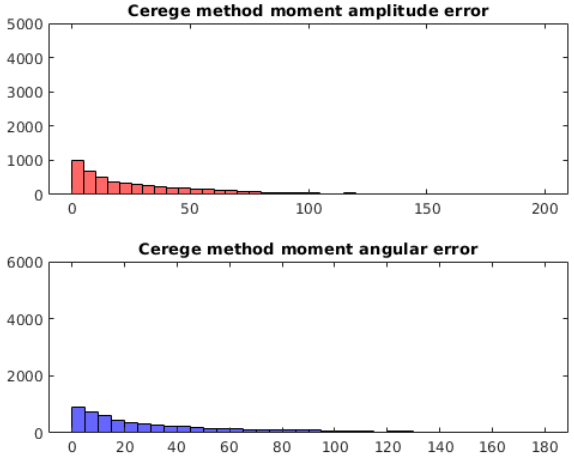

(b)

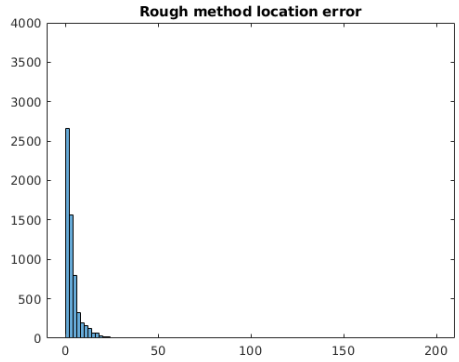

(c)

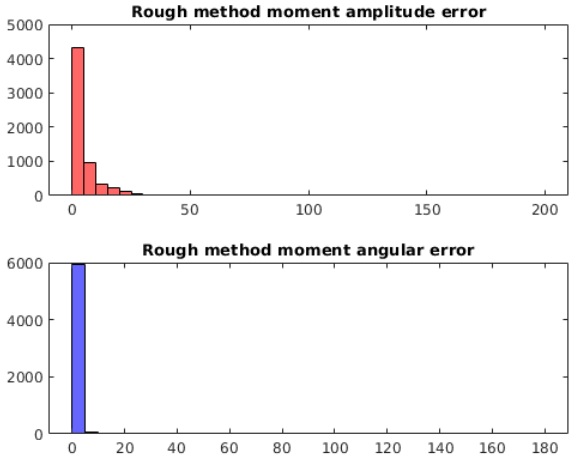

(d)

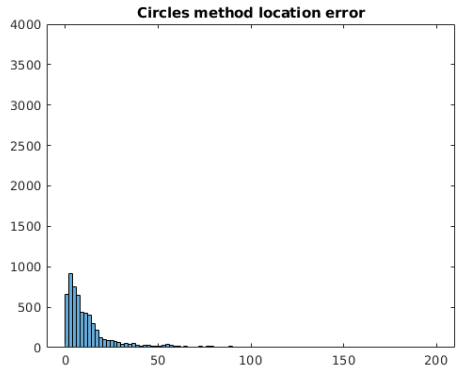

(e)

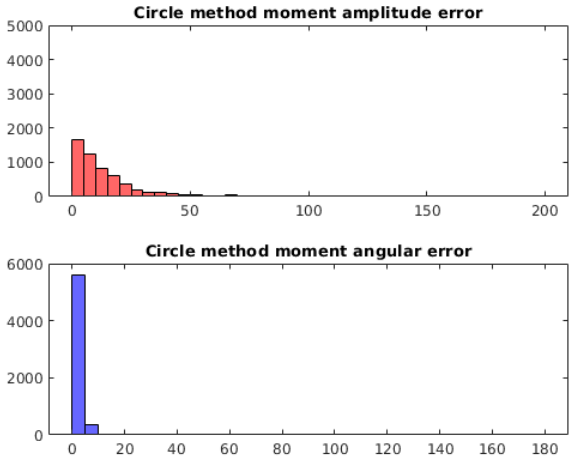

(f)

Figure 5.1: These experiments concern ideal data of 3 sensors, from 3 different positions. The illustrations compare the Cerege, rough and circles methods. Pictures on the left illustrate the $e_{est-act}$ distributions and pictures on the right the e_{ampl}, e_{ang} distributions.

5.2.2 Study of data without noise for multiple sensors

The setup of these experiments with ideal data is described in Chapter 1 Setup 1.7. As before we generate 6000 in a ball, but this time we use 11 sensors at each of the 3 positions. In Figure 5.2, one can see the distributions of the $e_{est-act}$, e_{ampl} and e_{ang} errors. We collect the results of our analysis in the following table:

# cases	$e_{est-act} > 20\%$	$e_{ampl} > 50\%$	$e_{ang} > 50^\circ$	$e_{ampl} < 25\%$	$e_{ang} < 10^\circ$
Cerege	5950	678	435	4433	3266
Rough	0	0	0	6000	6000
Circles	3	1	0	5988	5999

As we expected, for the Cerege method the number of dipoles with $e_{est-act} > 20\%$ is the same as before. That happens because the generated dipoles in both experiments have the exact same locations $\mathbf{X}_d$, since Cerege method assumes that $\hat{\mathbf{X}}_d = (0, 0, 0)$ at any case it means that the $e_{est-act}$ must be identical in both experiments. We can confirm this observation by comparing the $e_{est-act}$ distributions of Cerege method in Figures 5.1 and 5.2. However there is a significant improvement in the results of e_{ampl} and e_{ang} with the use of 11 sensors instead of 3. This improvement can be observed by comparing the distributions for e_{ampl} and e_{ang} in Figures 5.1 and 5.2 for each method, but it is more obvious for the Cerege and the circles methods. This is a strong evidence that for ideal data more sensors (that are located at different heights) provide us with better estimations for the $\mathbf{M}_d$.

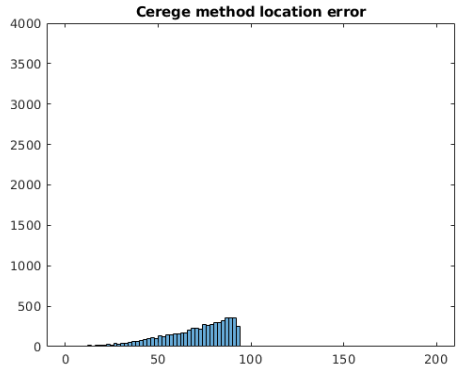

(a)

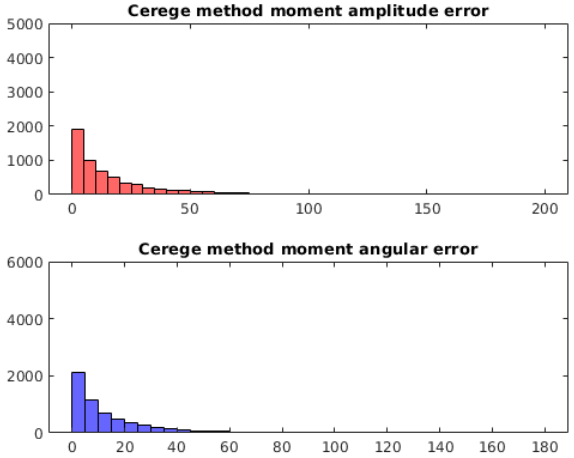

(b)

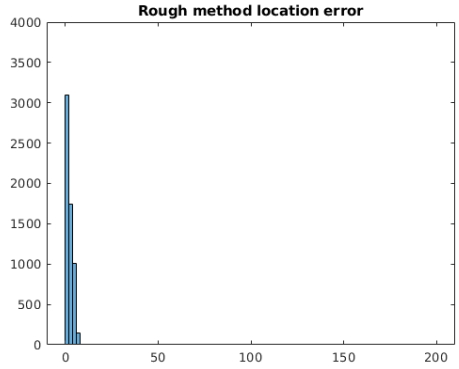

(c)

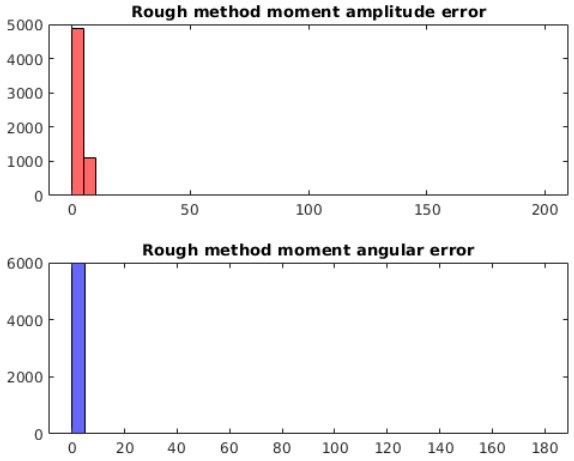

(d)

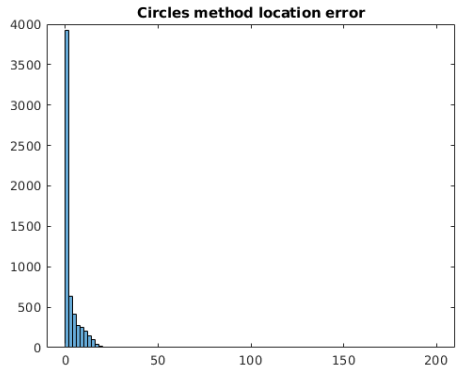

(e)

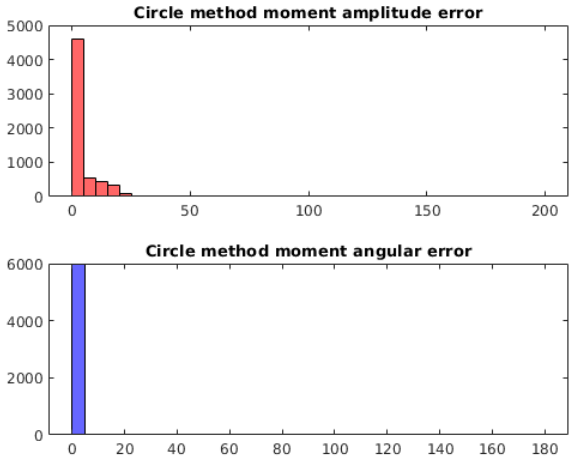

(f)

Figure 5.2: These experiments concern ideal data of 11 sensors, from 3 different positions. The illustrations compare the Cerege, rough and circles methods. Pictures on the left illustrate the $e_{est-act}$ distributions and pictures on the right the e_{ampl}, e_{ang} distributions.

5.2.3 Study of noisy data for the current lunometer configuration

For this setup of experiments we contaminate our signal with 5% uniform noise. Our experiments consist of 6000 dipoles in a ball and we take measurements from 3 positions as described in Setup 1.8. In Figure 5.3, we present the distributions of the $e_{est-act}$, e_{ampl} and e_{ang} errors. We collect the results of our analysis in the following table:

# cases	$e_{est-act} > 20\%$	$e_{ampl} > 50\%$	$e_{ang} > 50^\circ$	$e_{ampl} < 25\%$	$e_{ang} < 10^\circ$
Cerege	5950	1951	1704	2861	1631
Rough	4645	3797	593	776	3496
Circles	2722	706	575	3535	3410

The first observation is that for noisy data the rough method performs poorly. That is up to a point expected because the rough method uses only the information of the maximum modulus of $\xi'_{(i)-}$. Consequently for noisy data a bad estimation of $\xi'_{(i)-}$ will affect drastically the estimation $\hat{\mathbf{X}}_d$. This is also reflected on the number of cases with $e_{ampl} > 50\%$ and $e_{ang} > 50^\circ$ error which for the rough method concern 63.2% and 9.8% of our dipoles experiments respectively.

Another observation is that the circles method behaves better than the Cerege method. By comparing the distributions in Figure 5.3, one can see that Cerege method has more dipoles with $e_{ampl} < 5\%$ but its distribution decreases faster compared to the circles method. As a result, the circles method has more dipoles with $e_{ampl} < 25\%$. Also by comparing the e_{ang} distributions of the two methods we can see that with the circles method we have better estimation of the direction of the moment.

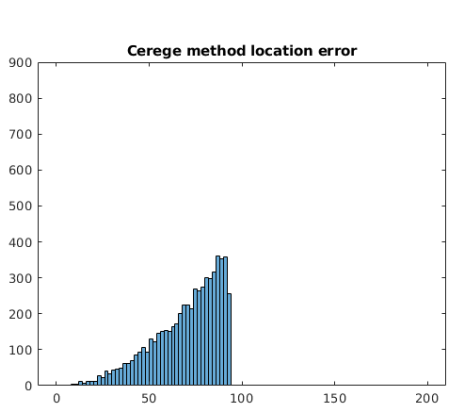

(a)

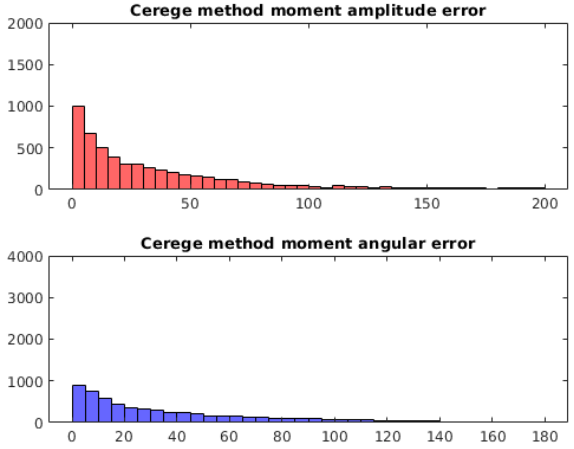

(b)

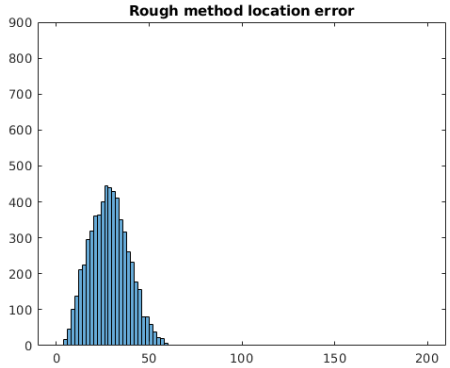

(c)

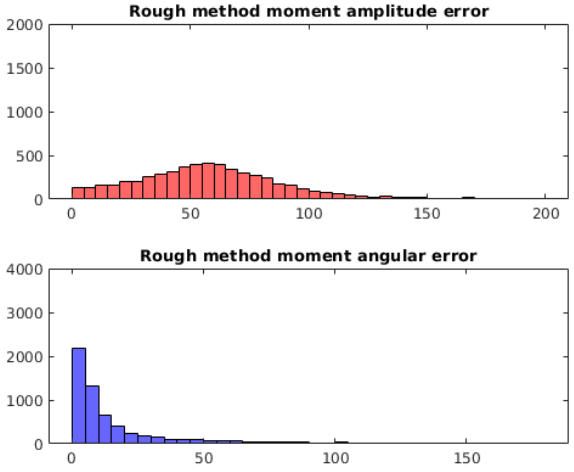

(d)

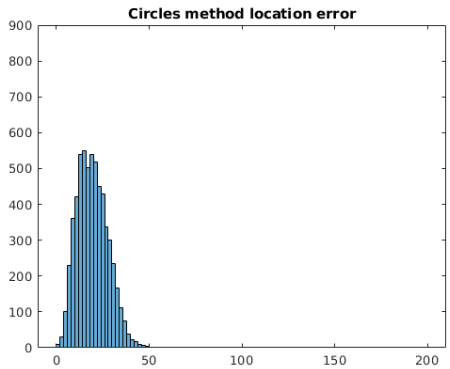

(e)

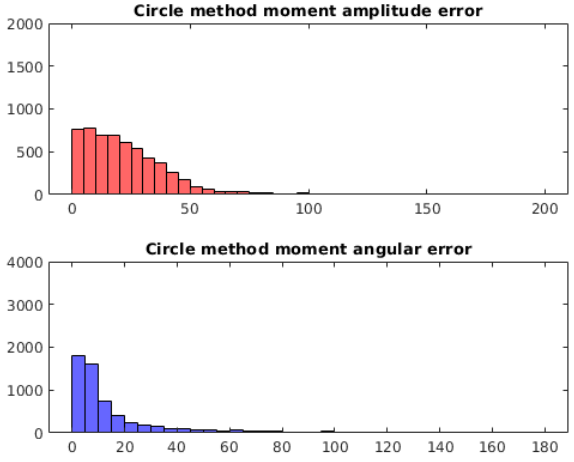

(f)

Figure 5.3: These experiments concern noisy data of 3 sensors, from 3 different positions. The illustrations compare the Cerege, rough and circles methods. Pictures on the left illustrate the $e_{est-act}$ distributions and pictures on the right the e_{ampl}, e_{ang} distributions.

5.2.4 Study of noisy data for multiple sensors and heights

Here we repeat the experiments with 5% uniform noise as before, only this time we use 11 sensors (per position) to measure the magnetic field, instead of 3. This setup of experiments is described in Chapter 1 Setup 1.9. In Figure 5.4, we present the distributions of the $e_{est-act}$, e_{ampl} and e_{ang} errors. We collect the results of our analysis in the following table:

# cases	$e_{est-act} > 20\%$	$e_{ampl} > 50\%$	$e_{ang} > 50^\circ$	$e_{ampl} < 25\%$	$e_{ang} < 10^\circ$
Cerege	5950	684	438	4426	3276
Rough	5758	4668	277	370	4094
Circles	547	342	281	4825	4400

This experiment confirms the observation that more sensors provide us with better estimations of the moment $\mathbf{M_d}$. For instance by comparing the distribution in Figures 5.3 and 5.4 we can see that the number of sensors plays an important role in improving the results of our estimations for both the dipole location $\mathbf{X}_d$ and its moment estimation $\mathbf{M_d}$.

By studying the cases with $e_{est-act} > 20\%$, $e_{ampl} > 50\%$ and $e_{ang} > 50^\circ$ for the circles method we observe that they are concentrated close to the borders of the sphere where the dipoles of our experiments are contained, see Figure 5.5. From our study there is no obvious correlation between the cases with $e_{ampl} > 50\%$ and $e_{ang} > 50^\circ$ except the fact that they are located close to the borders of our sphere. Though we investigate selected cases that are located close to the borders, we do not have a clear view for the reason behind this behavior. Note that because we have 3 measurement positions it means that there is at least one position where the illustrated dipoles are not close to the sensors.

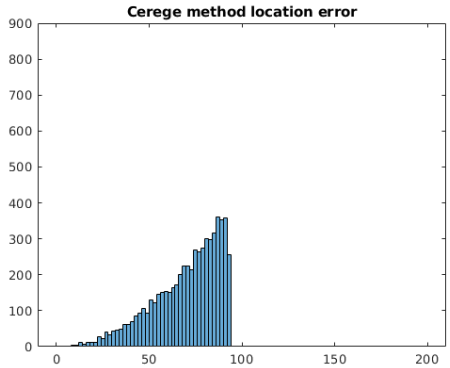

(a)

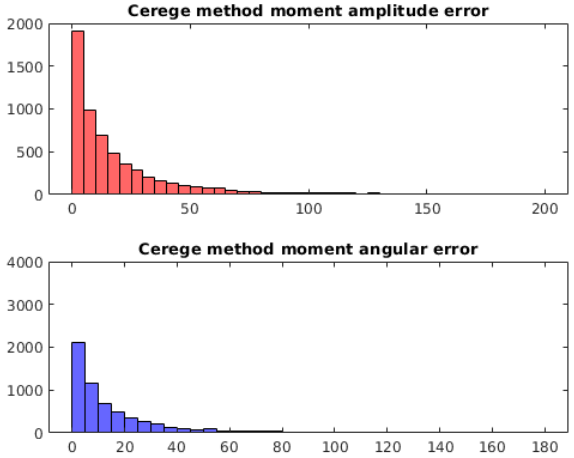

(b)

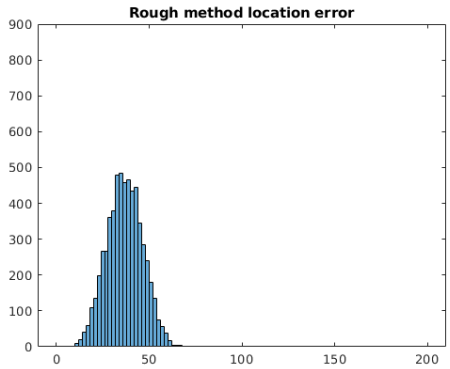

(c)

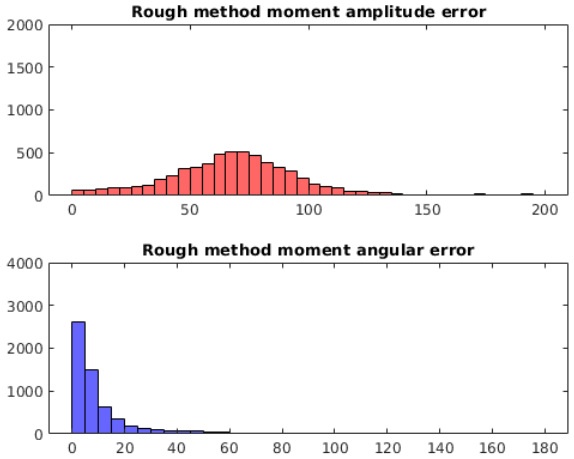

(d)

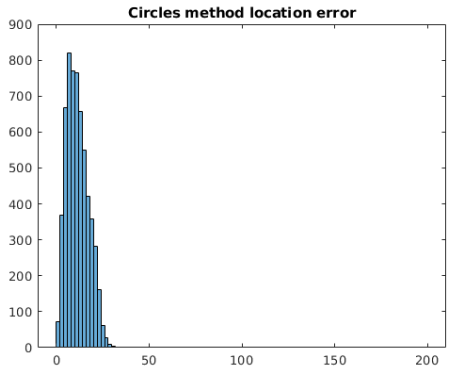

(e)

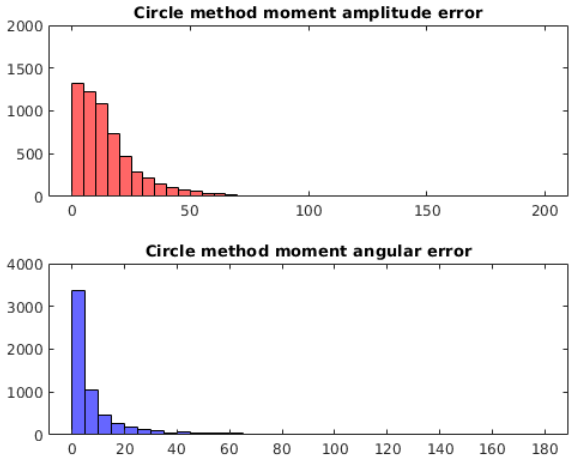

(f)

Figure 5.4: These experiments concern noisy data of 11 sensors, from 3 different positions. The illustrations compare the Cerege, rough and circles methods. Pictures on the left illustrate the $e_{est-act}$ distributions and pictures on the right the e_{ampl}, e_{ang} distributions.

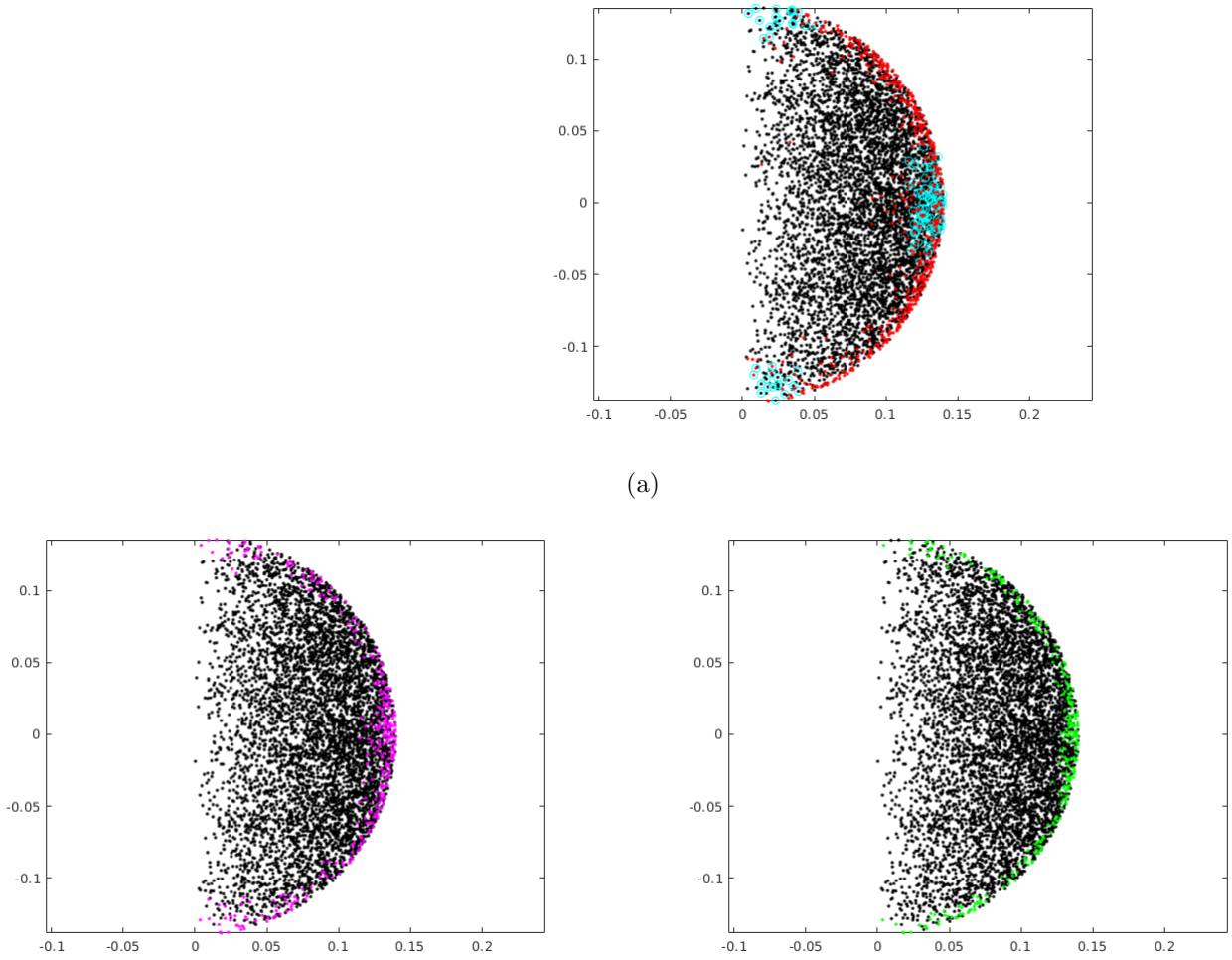

(a)

(b) (c)

Figure 5.5: Illustrations of circles method for noisy data form 11 sensors and from 3 measurement positions. All pictures contain 2D information of the dipole locations (black dots). The vertical axis correspond to z_d and the horizontal axis to $|x_d + \mathrm{i}y_d|$. The red dots on the top picture correspond to cases with $e_{est-act} > 20\%$ and the cyan circles to cases for which $\left|\hat{\mathbf{X}}_d\right|$ exceeds the radius R (those are cases that we are aware that we should not trust the moment estimation). The magenta dots at the bottom left picture, illustrate cases with $e_{ampl} > 50\%$ and the green dots at the bottom right picture illustrate cases with $e_{ang} > 50^{\circ}$.

5.2.5 Study of other parameters

Moment direction: one of the observations in our paper [20] was that the moment of a dipole can affect the estimation of both the dipole location $\mathbf{X}_d$ and its moment estimation $\mathbf{M_d}$. To test this assumption we select three individual cases from the experiments of Setup 1.6 (more precisely we select the 4, 5 and 6 generated dipoles with locations $\mathbf{X}_d(4) = [0.0228, -0.1080, 0.0690]$, $\mathbf{X}_d(5) = [-0.0526, -0.0529, -0.0838]$ and $\mathbf{X}_d(6) = [0.0519, 0.1101, -0.0668]$ which are illustrated in Figure 5.6 with red, blue and black diamonds respectively. Then we generate 1000 different moments for each one of the selected dipole locations with different orientations but with the same amplitude of 0.001. The setup of this experiment is described in Chapter 1 Setup 1.10.

Remark 23 *For this experiment we compare the results only for the circles method, however a similar behavior is observed also for the rough and Cerege methods.*

In the following tables we collect firstly the information of the circles method for the $e_{est-act}$, e_{ampl} and e_{ang} errors which concern our 3 dipoles from our reference experiments in Section 5.2.1. Secondly we compute the average values of $e_{est-act}$, e_{ampl} and e_{ang} for the 1000 generated moments per location based on the circles method too. The distribution of $e_{est-act}$, e_{ampl} and e_{ang} for each dipole can be seen in Figure 5.7.

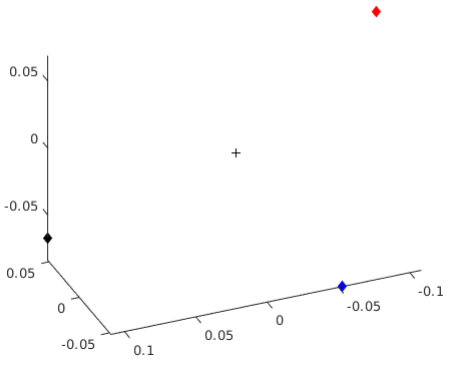

Figure 5.6: This picture illustrates the $\mathbf{X}_d(4) = [0.0228, -0.1080, 0.0690]$, $\mathbf{X}_d(5) = [-0.0526, -0.0529, -0.0838]$ and $\mathbf{X}_d(6) = [0.0519, 0.1101, -0.0668]$ dipole locations as red, blue and black diamonds respectively. The black cross denote the origin of our coordinate system.

Reference Section 5.2.1	Location error $e_{est-act}$	Moment amplitude error e_{ampl}	Moment angular error e_{ang}
$\mathbf{X}_d(4)$	19.7%	32.6%	2.39°
$\mathbf{X}_d(5)$	3.2%	4.4%	0.52°
$\mathbf{X}_d(6)$	6.9%	9.9%	1.33°

Current examples	Average location error $e_{est-act}$	Average moment amplitude error e_{ampl}	Average moment angular error e_{ang}
$\mathbf{X}_d(4)$	6.2%	8.5%	1.3°
$\mathbf{X}_d(5)$	4.3%	6.4%	1°
$\mathbf{X}_d(6)$	7.2%	10.4%	0.7°

The above tables show us the percentage error $e_{est-act}$, e_{ampl} and e_{ang} for our 3 individual locations for the circles method. The first table contains the information of the reference experiments and the second table contains the average information of the current experiments with the 1000 different moments. Based on the second table, one can see that we expect to have on average a certain percent of $e_{est-act}$, e_{ampl} errors and indeed the $\mathbf{X}_d(5)$ and $\mathbf{X}_d(6)$ locations of our reference experiment are close to the average values of the second table. However, $\mathbf{X}_d(4)$ has a larger value than the average value of the second table. For this reason we study the error distributions for each dipole location as illustrated in Figure 5.7. An interesting observation is that each location has a different behavior. For instance it is more likely to have a good approximation for the generated dipole in location $\mathbf{X}_d(5)$, than the generated dipole location $\mathbf{X}_d(4)$. In Figure 5.8 we collect the 3D information for the three selected locations, as well as the 3D information of the moment orientations. The magenta circles illustrate cases with $e_{ampl} > 10\%$, it is obvious that there is no specific moment directions which provide bad estimations. From our analysis it seems that the most important role for a good approximation of the moment plays the location of the dipole and not its moment direction.

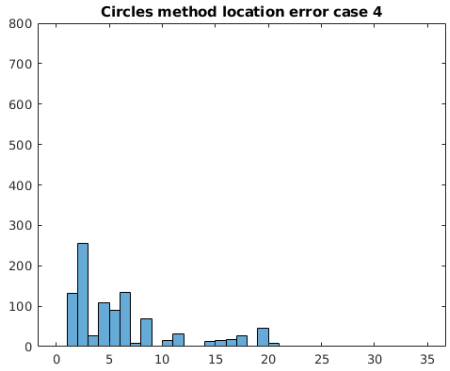

(a)

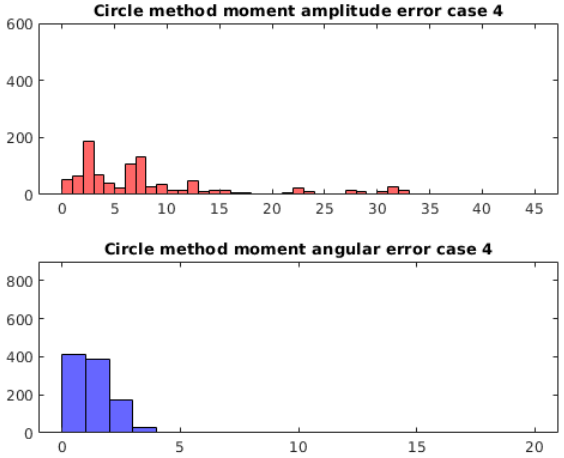

(b)

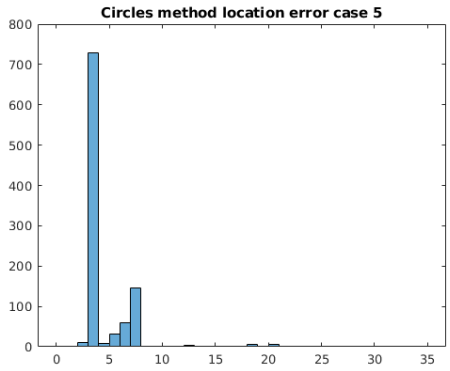

(c)

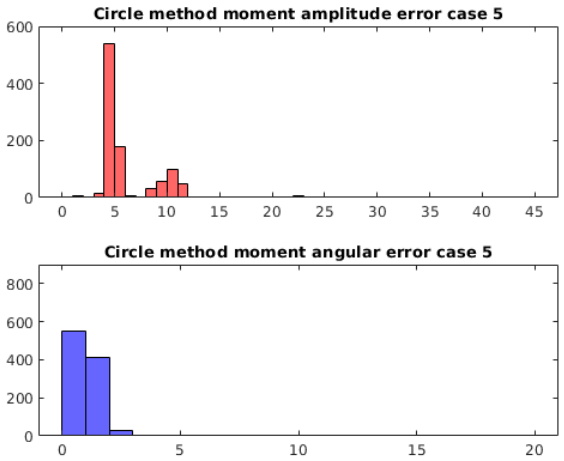

(d)

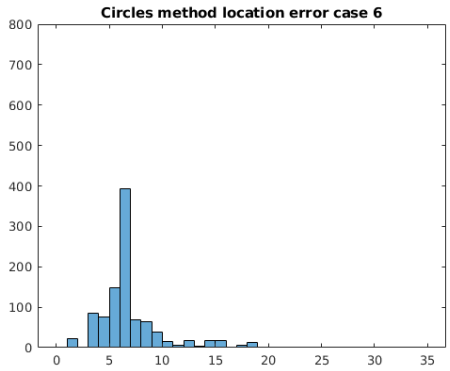

(e)

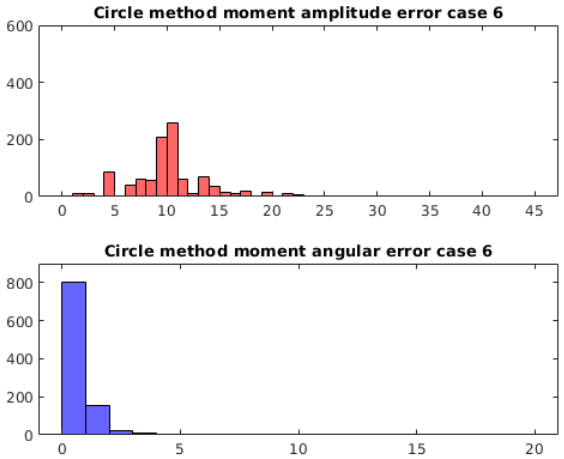

(f)

Figure 5.7: These experiments concern ideal data of 3 sensors, from 3 different positions. The illustrations focus on 3 specific locations with the use of circles methods. We provide the error distributions as follows: pictures on the left illustrate the $e_{est-act}$ and pictures on the right the e_{ampl}, e_{ang}.

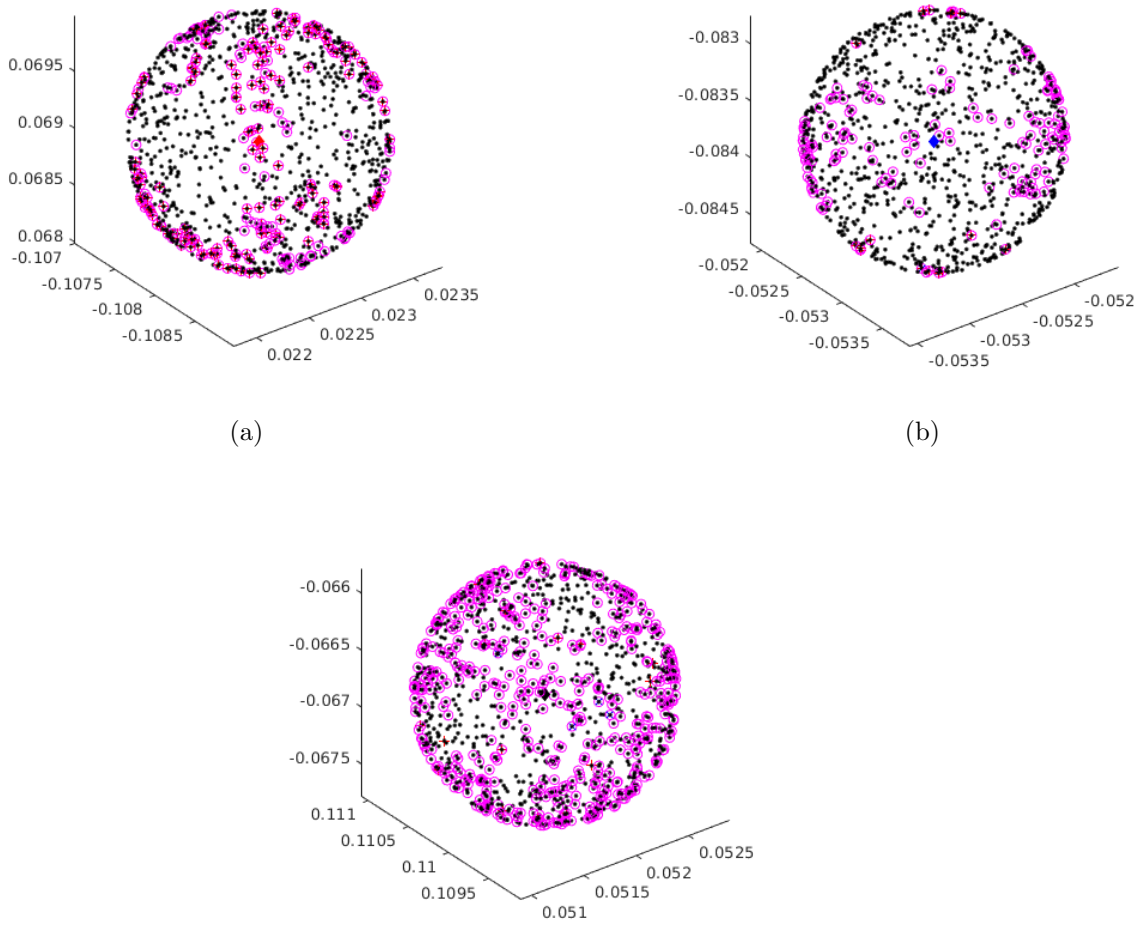

Figure 5.8: These experiments concern ideal data of 3 sensors, from 3 different positions. The illustrations focus on three specific dipole locations $\mathbf{X}_d(4)$, $\mathbf{X}_d(5)$ and $\mathbf{X}_d(6)$ and their results regarding the circles methods. We present the 3D information for the three selected dipole locations by using the colorcode of Figure 5.6 where each dipole location denoted with red, blue and black diamonds. Black dots illustrate the direction of the moments and the magenta circles denote cases with $e_{ampl} > 10\%$,

Number of measurement positions: another parameter that we are interested in testing with the circles method is the necessary number of measurement positions in order to compute good approximations of the dipole location $\mathbf{X}_d$ and its moment $\mathbf{M_d}$. In our reference experiments of

Section 5.2.1, we saw how the circles method performs for ideal data, with measurements taken by 3 sensors for 3 measurement positions as described in Setup 1.6. Here we repeat this experiment but we analyze the data firstly for all three measurements positions (as we did in Section 5.2.1), secondly for the first two measurement positions and lastly for only the first measurement position. In Figure 5.9 we present the distributions of the $e_{est-act}$, e_{ampl} and e_{ang} errors for the circles method with data acquired from 3, 2 and 1 measurements positions respectively. From those distributions one can observe that 3 measurement positions provide in general better results for the $e_{est-act}$, e_{ampl} and e_{ang} errors. However the two measurement positions also performs well. Only the results of a single measurement position provide poor estimations for $\mathbf{X}_d$ and $\mathbf{M_d}$. This is interesting information, which indicates that circles method needs data from at least two measurement positions in order to increase its performance. Through our analysis we confirm that the number of measurement positions plays indeed a more important role than the number of sensors at each position. In Section 5.2.6 for instance (which we discuss later) we conduct experiments for a single measurement position with 11 sensors, its $e_{est-act}$, e_{ampl} and e_{ang} distributions in Figure 5.10 have the same behavior with our single measurement distributions in Figures 5.9(e) and (f).

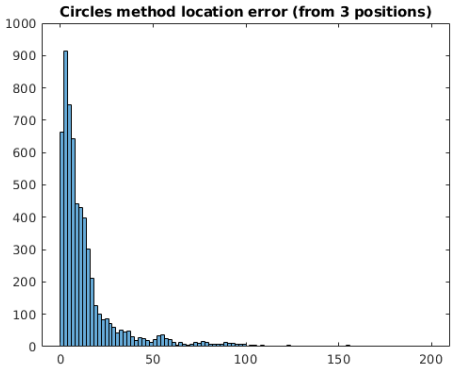

(a)

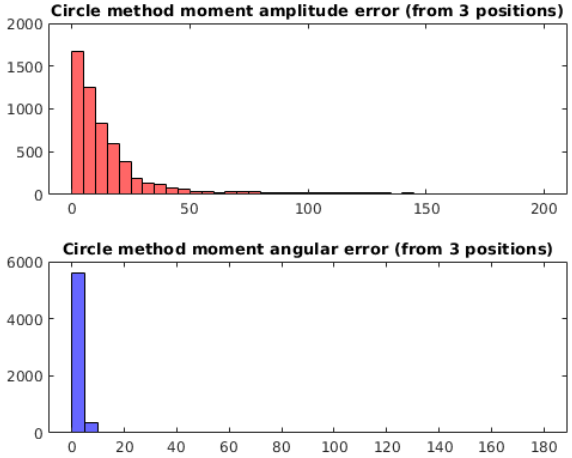

(b)

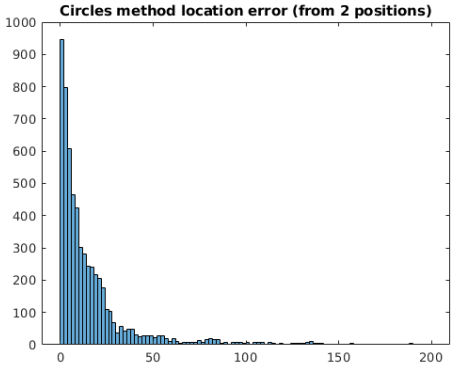

(c)

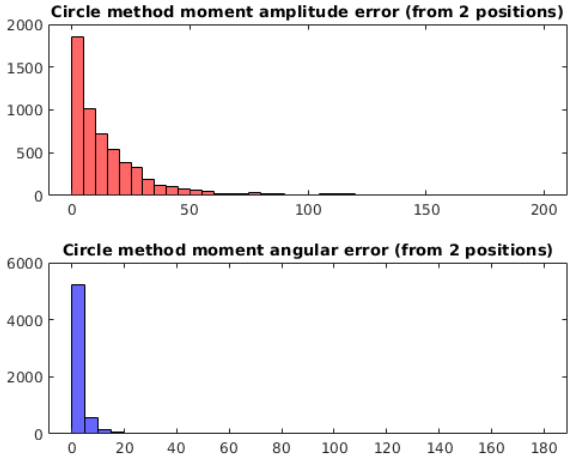

(d)

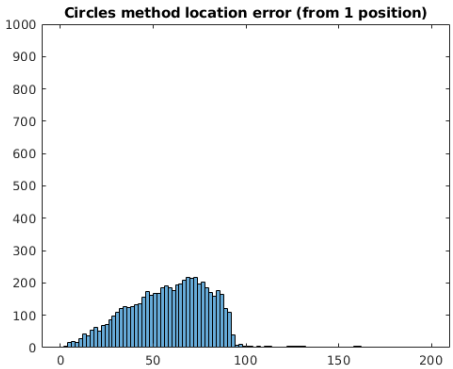

(e)

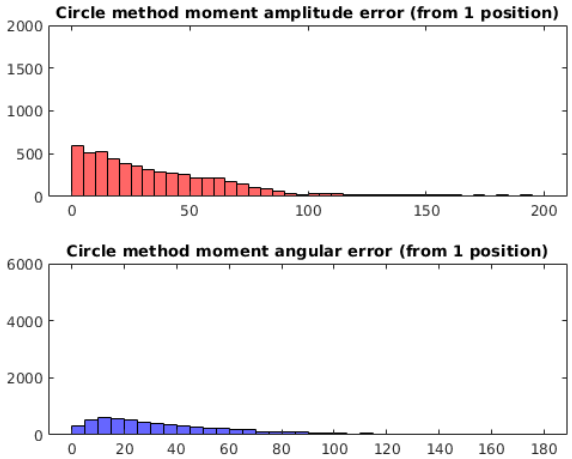

(f)

Figure 5.9: These experiments concern ideal data of 3 sensors, from 3, 2 and 1 measurement positions respectively. The illustrations focus on the circles method. The pictures on the left illustrates the error distribution of $e_{est-act}$ and the pictures on the right, the error distribution of e_{ampl}, e_{ang}.

Measurement step: we also test for the circles method, how the step size between pointwise measurements along a circular path affect our results. By step size we mean how often the sensors take measurements of the magnetic field $\mathbf{B}_{[\mathbf{X}_d,\mathbf{M}_d]}(\mathbf{X})$. In our simulations we take measurements every 1° (which gives us $N = 360$) in comparison the current lunometer takes measurements every 0.7° [10] $N = 512$. In this analysis we want to see how sparse the measurements can be (how large can the step between them be) in order to start affecting our results. For this test we use the first 100 cases from our reference experiments we describe in Section 5.2.1. That means that we have 100 generated dipoles that are uniformly spread inside a ball of radius $r = 0.14$. We use steps of 1°, 5°, 10° and 15° which provide us with $N = 360$, 72, 36 and 24 measurement points per circular path respectively. The results for the $e_{est-act}$, e_{ampl} and e_{ang} errors, are collected in the following table:

Table 5.1: measurement step for circles method

# cases	$e_{est-act} >$ 20%	$e_{ampl} >$ 50%	$e_{ang} >$ 50°	$e_{ampl} <$ 25%	$e_{ang} <$ 10°
step 1°	20	15	0	74	99
step 5°	23	15	0	72	99
step 10°	17	9	0	81	98
step 15°	41	4	0	63	89

The first observation is that, for ideal data with the use of circles method, until 10° it seems there is no significant difference in our results. The cases with $e_{ampl} > 50\%$ are observed at common dipole locations for the first three step sizes. There is an indication that steps up to 10° provide us with better results, we base this claim on the observation that we have fewer cases with $e_{ampl} < 25\%$ and $e_{ang} < 10°$ errors for the 15° step size compared to the other, smaller step sizes. In this analysis, the 10° step performs better; however it is not clear why this happens. In any case, these experiments provide us only with an intuition of the step size influence, due to the fact that they are conducted for a small number of dipoles. This is something that it is worth studying further, however due to time constraints we were not able to continue the study for more dipoles.

Single sensor / component: in Chapter 2 Section 2.5, we saw evidence that the measurements of $B_\perp$ sensor could provide us with better results compared to the B_r and B_τ sensors. This evidence however, comes from the study of a single sensor measurement at a specific height. In order to test if multiple $B_\perp$ sensors, which are located at different heights, can provide us with better $\mathbf{X}_d$, $\mathbf{M}_d$ estimations, we conduct experiments with noisy data for 1000 dipoles uniformly spread inside a ball, for a single measurement

position. For this experiment we use 11 $B_\perp$ sensors as described in Setup 1.11 and we compare their results by using 1000 dipoles uniformly spread inside a ball with the same size from the first measurement position of Setup 1.9 which we saw in Section 5.2.4. In Figure 5.10, we present the distributions of the $e_{est-act}$, e_{ampl} and e_{ang} errors for the circles method regarding the measurements of multiple $B_\perp$ sensors compared to multiple $B_r, B_\perp, B_\tau$ sensors. We observe that all of the distributions have similar behavior (shape). The small differences between the distributions can be explained by the fact that the 1000 dipoles of one of the experiments are different to the 1000 dipoles of the other experiment (not the same moments $\mathbf{M}_d$). We also collect some results in the following table:

# cases	$e_{est-act} >$ 50%	$e_{ampl} >$ 50%	$e_{ang} >$ 50°	$e_{ampl} <$ 25%	$e_{ang} <$ 10°
$B_\perp$ only	624	287	284	467	154
multiple $B_r, B_\perp, B_\tau$	624	237	188	434	161

This table confirms that there is no significant difference in our results, when we have multiple sensors that measure only the $B_\perp$ component or when we have multiple sensors that measure all three $B_r, B_\perp, B_\tau$ components of the field. However one extra piece of information that does not appear in the table is that, with multiple $B_\perp$ sensors, we exclude 14 cases based on the way we have computed the averaged plane (recall the process of the $\text{Arg}(\hat{\xi}_{(i)-})$ list which we saw in Chapter 3 Section 3.2.1). In contrast with multiple sensors $B_r, B_\perp, B_\tau$ we exclude 55 cases. This could be a coincidence due to the fact that our two experiments study different dipole moments. Once again through time limitations we are not able to continue our study in depth, however this is one more observation that needs further investigation.

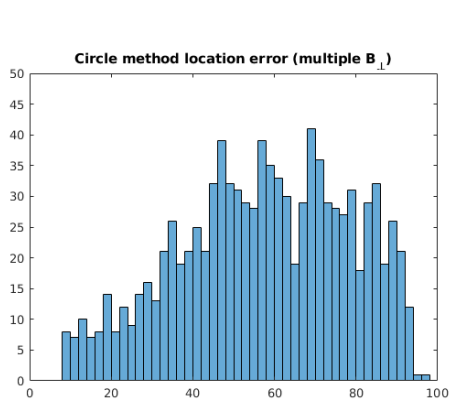

(a)

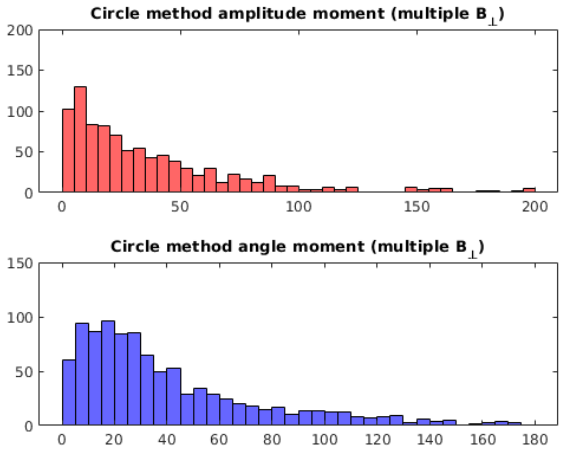

(b)

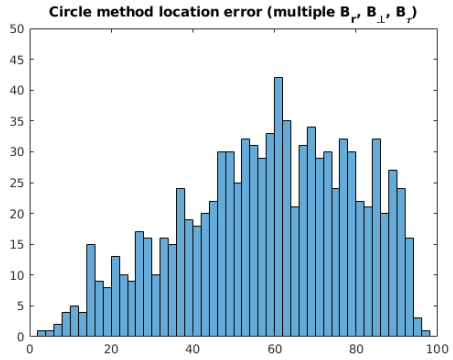

(c)

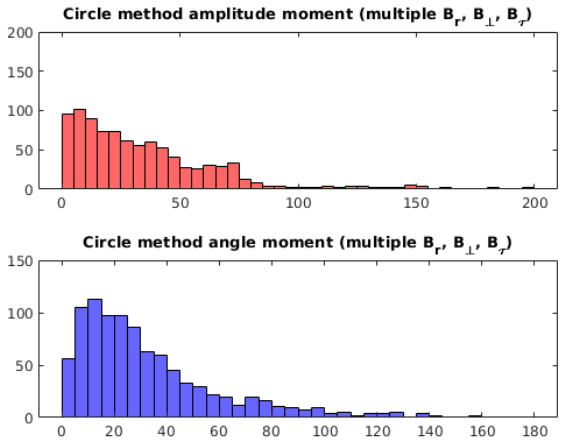

(d)

Figure 5.10: These experiments concern noisy data of 11 sensors, from a single measurement position. The illustrations focus on the circles method. The pictures on the left illustrate $e_{est-act}$ distributions and the pictures on the right e_{ampl}, e_{ang} distributions. The top three pictures regard measurements only of $B_\perp$ component and the bottom three pictures from $B_r, B_\perp, B_\tau$ components.

5.2.6 Study of possible clusters

Study of possible clusters for multiple sensors: when we study the planes method in Chapter 3 Section 3.2.1, we set the question if for multiple sensors we have the ability to disregard measurements from specific sensors instead of disregarding the whole measurement position. Here we analyze

the information from the Setup 1.11 which concerns the experiments of 1000 dipoles inside a ball and measurements taken from multiple $B_\perp$ sensors for a single measurement position. From the pole estimations $\hat{\xi}_{(i)-}$ (with $i = 1, ..., 11$) we compute a list with their arguments $\text{Arg}(\hat{\xi}_{(i)-})$. Now in Chapter 3 we exclude the measurements of a whole position when we faced cases with angle ranges that exceed 90°. In this experiment we have in total 14 excluded cases for which we collect the angle information $\text{Arg}(\hat{\xi}_{(i)-})$ (converted to degrees) at the following table. Note that the last column of the table contain the actual (theoretical) angle $\text{Arg}(\xi'_-)$ of the dipole computed from the true location $\mathbf{X}_d$ of each dipole.

Table 5.2: list of angles $\text{Arg}(\hat{\xi}_{(i)-})$ and $\text{Arg}(\xi'_-)$

Ex. case	$\text{Arg}(\hat{\xi}'_{(1)-})$	$\text{Arg}(\hat{\xi}'_{(2)-})$	$\text{Arg}(\hat{\xi}'_{(3)-})$	$\text{Arg}(\hat{\xi}'_{(4)-})$	$\text{Arg}(\hat{\xi}'_{(5)-})$	$\text{Arg}(\hat{\xi}'_{(6)-})$
1	40	-93	-111	99	-10	5
2	-86	-108	-93	-128	-127	-130
3	172	179	-176	-180	-167	179
4	-40	-59	-22	128	-180	-77
5	-119	-59	-93	-82	-102	-58
6	-149	-175	-139	165	-169	-94
7	15	31	26	8	17	-13
8	85	44	48	10	77	134
9	-103	-117	-124	-121	-120	-119
10	-131	-156	-155	-166	-117	-91
11	-25	-20	-13	-32	-26	-17
12	24	23	25	-86	22	18
13	159	32	-1	112	116	113
14	152	106	-163	-176	148	145
Ex. case	$\text{Arg}(\hat{\xi}'_{(7)-})$	$\text{Arg}(\hat{\xi}'_{(8)-})$	$\text{Arg}(\hat{\xi}'_{(9)-})$	$\text{Arg}(\hat{\xi}'_{(10)-})$	$\text{Arg}(\hat{\xi}'_{(11)-})$	$\text{Arg}(\xi'_-)$
1	2	5	-1	-7	7	-3
2	-130	-131	-124	176	148	-129
3	156	179	-170	154	96	-180
4	-75	-84	-76	-83	-81	-79
5	-49	136	84	10	-50	-80
6	-128	-161	-153	-150	-154	-155
7	-63	-29	-20	-31	-42	-14
8	26	25	28	28	24	27
9	-121	-149	165	-158	-116	-122
10	-157	156	119	-145	-104	-119
11	-147	144	10	163	166	-28
12	17	20	19	15	17	18
13	114	118	121	117	115	113
14	145	147	145	147	147	146

Because our angles vary from $[-180, 180)$ degrees it is difficult to determine from the table above how many of our $\text{Arg}(\hat{\xi}_{(i)-})$ are close to the theoretical

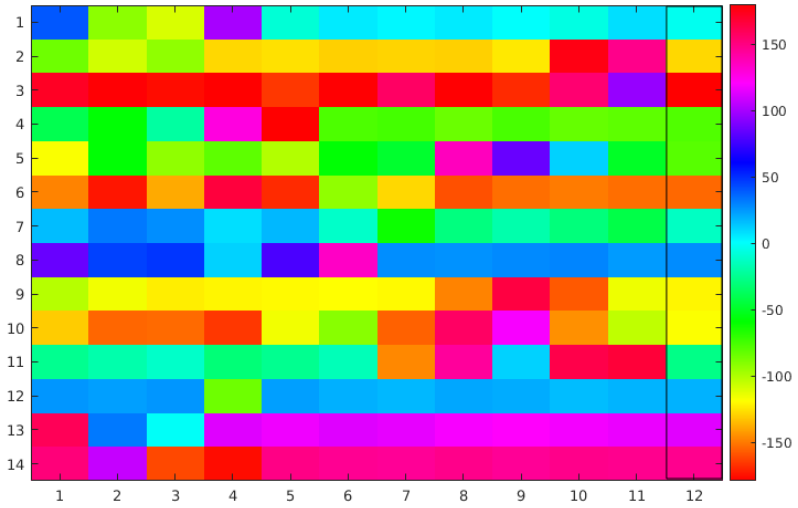

Figure 5.11: This picture illustrates the information of Table 5.2 which is interepreted with colors based on the provided colorbar.

angle $\text{Arg}(\xi'_-)$. For this reason in Figure 5.11 we use a different representation of the table's information. More precisely we make a color coded table where the last column of the table contains the (theoretical) angles $\text{Arg}(\xi'_-)$ as before. The values of the angles in this table are associated with a color as one can see from the color bar at the right hand-side of Figure 5.11 which varies between $[-180, 180)$ degrees. Now each row corresponds to one of the excluded cases and the first 11 columns of the color table gather the information $\text{Arg}(\hat{\xi}'_{(i)-})$ with $i = 1, ..., 11$. With this representation the angles of each row that differs a lot from the true angle are easily identified. For instance, the first line of the color table shows that the first 4 sensors provide angles further away from the actual angle (cyan color of the 12^{th} column).

From the above analysis, a first answer is that for multiple sensors a clustering process, which excludes information from specific sensors, is possible. That happens because one can observe that in most cases, there are only few sensors with bad angle estimation. However, for a definitive answer more investigation is required.

CHAPTER 6

General discussion and conclusion

Paleomagnetic studies try to understand the history and the evolution of the magnetic field of planets and planetary objects. Through those studies, hypotheses such as the continental drift [45], the tectonic plates and the geomagnetic reversal [16] have been proposed and confirmed. Because of these studies, the way we understand the world has changed. One important factor in these studies is that with the right conditions, ferromagnetic materials can preserve natural remanent magnetization (NRM) for long periods of time (even billions of years). The difficulty geoscientists face is how to recover accurately the magnetization from various objects. For this reason they develop invasive techniques where they demagnetize the samples under study such as rocks or clay fragments [12]. However invasive techniques limit geoscientists to studying small samples, which are essentially destroyed after the study. This motivates them to develop instrumentation for noninvasive techniques [10]. New technologies also help them to increase the sensitivity of sensors that record the magnetic field of a rock.
Despite the new technological advantages there are still some physical limitations that puzzle the geoscientists. With noninvasive techniques they can measure the magnetic field around a sample [11], but then they have to deal with an inverse problem in order to recover the magnetization that generates this field. In our study we saw that in order to have good estimations of the magnetization $\mathbf{M}_d$ the knowledge of the source location $\mathbf{X}_d$ is important. To estimate the location $\mathbf{X}_d$ for large samples (for instance a rock that has a mass of 1 kg) geoscientists have two options:

- The first option is to take measurements at a distance from the sample. In that case an approximation of the magnetic source location at the sample's mass center is valid. However magnetic field varying as an inverse cube (with respect to the distance), that can be observed in Equation (1.7) from the denominator expression $|\mathbf{X} - \mathbf{X}_d|^3$.

That means that the field strength decreases rapidly when we increase the distance from the magnetic source. Hence, if geoscientists take measurements at a distance from the sample, they are in fact just measuring noise.

- The second option they have is to take measurements close to the (large) sample. However, in a case like this, the framework geoscientists use (namely the assumption that the magnetic source is located at the center of the sample's mass) could be invalid.

Contribution and experimental observations

In our thesis we address exactly a situation like the above second option. More precisely, we study what happens when we take measurements of a large sample with a single magnetic source from a small distance. During our study, we saw how to estimate the source location $\mathbf{X}_d$ and the magnetization $\mathbf{M}_d$. An important contribution of our study is that we gain intuition for the behavior of a magnetic source due to the large number of synthetic data experiments we conducted (more than 680.000 experiments). In this thesis we include only a small part of our experiments in order to highlight our main observations, more precisely from our experiments with synthetic data in Chapter 5 (Section 5.2) we observe that there exists some parameters which can be controlled by geoscientists and can affect the $\mathbf{M}_d$ estimation. Some of these parameters are the following:

- **Number of sensors:** in our analysis, both with ideal and noisy data, we observe an improvement of the $\mathbf{M}_d$ estimation based on the number of sensors we use. Though we had some evidences in Chapter 2 Section 2.5 that $B_\perp$ sensor could perform better than other two sensors, the overall picture we have after our study in Chapter 5 Section 5.2 is that, it does not matter what sensor we use (measurement of a specific component) but how many sensors we have at each measurement position. In fact in Chapter 2 we test the pole estimation $\hat{\xi}'_-$ for each sensor B_r, B_τ and $B_\perp$ by conducting experiments for 4000 dipoles from one measurement position at a specific height $z = 0.015$. In contrast in Chapter 5 we conducted experiments for 1000 dipoles with measurements from one position at heights z that varies from [-0.075, 0.075]. For the multiple sensors experiments we compare the $\mathbf{X}_d$, $\mathbf{M}_d$ estimations by using only $B_\perp$ sensors at the one case and a combination of B_r, B_τ and $B_\perp$ at different heights at the other case. We observe that the multiple sensors results were comparable, which suggests that indeed it is more important to have many sensors at each measurement position, than fewer sensors, which measure a specific component.

- **Number of measurement positions:** though having measurements of 2 or 3 different positions is time consuming, in Chapter 5 Section 5.2 we observe that it is really important to combine information from many positions for a good $\mathbf{M}_d$ estimation. The information from the extra positions is a critical factor that works as a weight for our data and leads us to better estimations. In fact it is more important to have measurements from different positions than having one position with many sensors.

- **Level of noise:** the higher the level of noise the worst our estimations for $\mathbf{X}_d$ and $\mathbf{M}_d$. This is an expected observation. In our study with synthetic data we investigate cases with ideal signal and cases with noisy data. We study the noisy data experiments without applying any denoising treatment. We do this because we are planning to test the raw measurements of the magnetic field, provided to us by the geoscientists in Cerege. To be more precise, we know that geoscientists take measurements at magnetically isolated facilities. However they still face issues of jumps and drift in their signal. For this reason they use a denoising technique known as Savitzky-Golay filter. With this technique they recover a signal that resembles the signal from a single (centered) dipole that has no drift or jumps. With our approach we want to compare the results of the raw signal analysis with the results of the signal after treatment.

Now concerning the question "which method of our study is best to be use in order to estimate the magnetization $\mathbf{M}_d$?", the answer depends on the level of noise.

- **Ideal data:** for cases where the data can be considered ideal, the best method to use in order to estimate the magnetization $\mathbf{M}_d$ is the rough method which is described in Chapter 4 Section 4.5. This method performs well for data without noise and provides us with accurate estimations of the source location $\mathbf{X}_d$, which in turn provides us with good estimations for the magnetization $\mathbf{M}_d$.

- **Noisy data:** for cases with noisy data (without applying any denoising treatment) we propose the circles method as explained in Chapters 3 and 4. However this is an answer that needs some extra explanation. For noisy data the Cerege method provides similar results with the circles method as one can see by comparing the distributions of the two methods in Figures 5.3 and 5.4. The reason why we propose the use of circles method is because it has better results for the e_{ang} error and it consistently has more dipoles with amplitude error $e_{ampl} < 25\%$. However one can debate that the performance of Cerege method especially for experiments with noisy data with 11 sensors for 3 different

positions is comparable with the performance of the circle method. In this particular scenario one can indeed use the Cerege method in terms of convenience by sacrificing slightly its estimation accuracy. Despite this special occasion we believe that for noisy data, circles method is a good option, because it gives a higher level of confidence for both e_{ang} and e_{ampl} error.

Further work

One important process to continue with our work is to test our method with real data. We couldn't include results with real data analysis because we didn't finish the code adaptations in order to interpret them properly. However through our synthetic data analysis we observe some factors that would be interesting to study in depth, these factors are the following:

- **Number of dipoles:** one main assumption in our model is that the magnetic field we measure is generated form a single dipole. Though it could be valid for homogeneous magnetized objects, this assumption is not realistic for objects such as rocks. For this reason we want to expand the model in order to estimate more than one dipole location (possibly 2 or 3 dipole locations is a feasible goal).

- **Filtering process:** we have already shown evidence that when we use multiple sensors at different heights z_i we can disregard information from specific sensors, instead of disregarding the information from the whole measurement position. This is an observation worth further investigation, because it can increase the quality of our estimations.

- **Noisy data:** as we have already discussed the level of noise is an important parameter that should be studied in depth. A comparison of $\mathbf{M}_d$ estimations regarding raw and treated signal could reveal interesting results.

- **Comparison with other methods:** though our main concern in this thesis was to compare our methods with the method currently used by geoscientists, in literature one can find other available methods in order to estimate the source location $\mathbf{X}_d$ and the magnetization $\mathbf{M}_d$, *e.g.* spherical harmonics or multipole expansion [46]. A comparison between all these methods for the same set of data could reveal interesting results regarding the magnetization recovery.

Bibliography

[1] H. Tsunakawa, F. Takahashi, H. Shimizu, H. Shibuya, and M. Matsushima. Surface vector mapping of magnetic anomalies over the Moon using Kaguya and Lunar Prospector observations. *AGU Journal of Geophysical Research: Planets*, 120:1160–1185, 2015.

[2] M. Fuller. *Our Beautiful Moon and its Mysterious Magnetism: A Long Voyage of Discovery*. Springer, 2014.

[3] M. Fuller and S.M. Cisowski. Lunar paleomagnetism. *Geomagnetism*, 2:307–455, 1987.

[4] B.P. Weiss and S.M. Tikoo. The lunar dynamo. *Science*, 346, 2014.

[5] M.A. Wieczorek, B.L. Jolliff, A. Khan, M.E. Pritchard, B.P. Weiss, J.G. Williams, L.L. Hood, K. Righter, C.R. Neal, C.K. Shearer, I.S. McCallum, S. Tompkins, B.R. Hawke, C. Peterson, J.J. Gillis, and B. Bussey. The Constitution and Stracture of the Lunar Interior. *Reviews in Mineralogy & Geochemistry*, 60:221–364, 2006.

[6] M.A. Wieczorek, B.P. Weiss, and S.T. Stewart. The Impactor Origin for Lunar Magnetic Anomalies. *Science*, 335, 2012.

[7] R. Skomski. *Simple Models of Magnetism*. Oxford University Press, first edition, 2008.

[8] M.J. Dekkers. Magnetic Proxy Parameters. *Encyclopedia of Geomagnetism and Paleomagnetism*, 2007.

[9] J.S. Oliveira, M.A. Wieczorek, and G. Kletetschka. Iron abundances in lunar impact basin melt sheets from orbital magnetic field data. *Journal of Geophysical Researc: Planets*, 122:2429–2444, 2017.

[10] M. Uehara, J. Gattacceca, Y. Quesnel, C. Lepaulard, E.A. Lima, M. Manfredi, and P. Rochette. A spinner magnetometer for large Apollo lunar samples. *Review of Scientific Instruments*, 88, 2017.

[11] C. Lepaulard, J. Gattacceca, M. Uehara, P. Rochette, Y. Quesnel, R.J. Macke, and S.J.W. Kiefer. A survey of the natural remanent magnetization and magnetic susceptibility of Apollo whole rocks. *Physics of the Earth and Planetary Interiors*, 290:36–43, 2019.

[12] D.J. Dunlop. Physical basis of the Thellier-Thellier and related paleointensity methods. *Physics of the Earth and Planetary Interiors*, 187:118–138, 2011.

[13] D.J. Dunlop. Intrinsic paleointensity bias and the long-term history of the geodynamo. *Science Advances*, 2017.

[14] D.A. Brain, S. Barabash, S.W. Bougher, F. Duru, and R. Jakosky, B.M.and Modolo. *Solar wind interaction and atmospheric escape*. Cambridge University Press, 2017.

[15] R.B. Horne, M.W. Phillips, S.A. Glauert, A.D.P. Hands, K.A. Ryden, and W Li. Realistic worst case for a severe space weather event driven by a fast solar wind stream. *Space Weather*, 16:1202–1215, 2018.

[16] B. M. Clement. Dependence of the duration of geomagnetic polarity reversals on site latitude. *Letters to nature*, 428:637–640, 2004.

[17] C. Cournède, J. Gattacceca, and P. Rochette. Magnetic study of large Apollo samples: Possible evidence for an ancient centered dipolar field on the Moon. *Earth and Planetary Science Letters*, (331-332):31–42, 2012.

[18] J. D. Jackson. *Classical electrodynamics*. John Wiley & Sons, Inc., third edition, 1999.

[19] L. Baratchart, D. P. Hardin, E. A. Lima, E. B. Saff, and B. P. Weiss. Characterizing kernels of operators related to thin plate magnetizations via generalizations of hodge decompositions. *IOP Publishing Ltd, Inverse Problems*, 29, 2012.

[20] S. Chevillard, J. Leblond, and K. Mavreas. Dipole recovery from sparse measurements of its field on a cylindrical geometry. *International Journal of Applied Electromagnetics and Mechanics*, 59:209–215, 2019.

[21] M. Clerc, J. Leblond, J.P. Marmorat, and T. Papadopoulo. Source localization using rational approximation on plane sections. *Inverse problems*, 28, 2012.

[22] J.P.Jr. Wikswo and K.R. Swinney. A comparison of scalar multipole expansions. *Journal of Applied Physics*, 56:3039–3049, 1984.

[23] G. Nolte. The relevant degrees of freedom of a focal source in MEG measurements. *Biomedizinische Technik*, 46:41–43, 2001.

[24] J.R. Partington. *Interpolation Identification and Sampling.* Oxford Science Publications, 1997.

[25] N. Young. *An introduction to Hilbert space.* Cambridge University Press, 1997.

[26] G. H. Golub and C. F. Van Loan. *Matrix Computations.* John Hopkins University Press, 3rd edition, 1996.

[27] A. Cooman, F. Seyfert, and S. Amari. Estimating unstable poles in simulations of microwave circuits. *IEEE, International Microwave Symposium*, 2018.

[28] T. Kailath and A.H. Sayed. *Fast Reliable Algorithm for Matrices with Structure.* SIAM, 1999.

[29] S.Y. Kung and K.S. Arun. *Advances in statistical signal processing.* JAI Press, 1987.

[30] K. Glover. All optimal hankel-norm approximations of linear multivariable systems and their H_∞-error bounds. *International J. Control*, 39:1115–1193, 1984.

[31] L. Baratchart, J. Leblond, and J.P. Marmorat. Inverse source problem in a 3D ball from best meromorphic approximation on 2D slices. *Electronic Transactions on Numerical Analysis*, 25:41–53, 2006.

[32] K. Wirth and A.S. Dreiding. Relations between edge lengths, dihedral and solid angles in tetrahedra. *J Math Chem*, 52:1624–1638, 2014.

[33] A. Van Oosterom and J. Strackee. The solid angle of a plane triangle. *IEEE*, 30:125–126, 1983.

[34] O. Mazonka. Solid angle of conical surfaces, polyhedral cones, and intersecting spherical caps. *Lecture notes*, 2012.

[35] J. Casey. *A treatise on Spherical Trigonometry and Applications to Geodesy and Astronomy.* Hodges, Figgis, & co., 1889.

[36] W. Gellert, H. Kustner, Hellwich M., and Kastner H. *The concise encyclopedia of mathematics.* Van Nostrand Reinhold Company, 1977.

[37] P. Courrieu. Fast computation of Moore-Penrose inverse matrices. *Neural Information Processing - Letters and Reviews*, 8:25–29, 2005.

[38] R. A. Johnson. *Advanced Euclidean Geometry.* Dover Publications, Inc., 1960.

[39] H.M. Lufkin. The minimal properties of the isogonal centers of a triangle. *The American Mathematical Monthly*, 30(3):127–131, 1923.

[40] J.S. Mackay. Isogonic centers of a triangle. *The Mathematical Association*, 19:54–60, 1893.

[41] M. Fujimura, P. Hariri, M. Mocanu, and M. Vuorinen. The Ptolemy-Alhazen problem and spherical mirror reflection. *Computational Methods and Function Theory*, 2018.

[42] J.D. Smith. The remarkable Ibn Al-Haytham. *The Mathematical Gazette*, 76:189–198, 1992.

[43] S. Lang. *Algebra*. Springer, 3rd edition, 2002.

[44] T.J. Ypma. Historical development of the newton-raphson method. *SIAM*, 37:531–551, 1995.

[45] X. Le Pichon. Sea-floor spreading and continental drift. *Journal of Geophysical research*, 73(12):3661–3697, 1968.

[46] J.P. Wikswo and K.R. Swinney. Scalar multipole expansions and their dipole equivalents. *J. Appl. Phys.*, 57:4301–4308, 1985.